Wear control in sheet metal forming – detection and life span estimation

vom Fachbereich Maschinenbau

der Technischen Universität Darmstadt

zur Erlangung des Grades

Doktor-Ingenieur

(Dr.-Ing.)

Dissertation

von

Yutian Wu

aus Shanghai (China)

Erstgutachter:	Prof. Dr.-Ing. Dipl.-Wirtsch.-Ing. P. Groche
Zweigutachter:	Prof. Dr.-Ing. Matthias Weigold

Darmstadt 2023

Acknowledgement

This dissertation was written while I was working as a research assistant at the Institute of Production Engineering and Forming Machines (PtU) at Technical University of Darmstadt. I would like to express my special thanks to the institute director, Prof. Dr.-Ing. Dipl.-Wirtsch.-Ing. Peter Groche, for the trust he bestowed on me from the beginning of the employment, the associated freedom in research work as well as the development opportunities within the scope of the activities, the professional suggestions as well as for the evaluation. I would like to thank Prof. Dr.-Ing. Matthias Weigold for taking over the co-lecture and for the technical discussion.

I would like to thank all my colleagues for an enjoyable and exceptionally pleasant time at the institute. Furthermore, I would like to express my gratitude for the constant support from the staff of the affiliated mechanical workshop. Special thanks go to Ms. Yuchen Leng, Mr. Ulfar Arinbjarnar and Mr. Alessandro Franceschi for their critical review of my dissertation, as well as to Mr. Felix Flegler and Prof. Dr. Chengliang Hu for their professional expertise and collegial cooperation. I would also like to thank my students and research assistants. In particular, I would like to mention Mr. Diego Ignacio Miranda Silva, Ms. Yuchen Leng and Mr. Gohar Ali Suddiqui.

Part of the presented work was funded by the German Federal Ministry for Economic Affairs and Climate Protection within the framework of joint industrial research of the AiF. I would like to thank the consortium of the research project for the fruitful cooperation and would like to express my special thanks to Dr. Matthias Prier (Hans Berg GmbH & Co KG), Dr. Bernd Aha (Zeller+Gmelin) and Mr. Sebastian Röhner (ZF Friedrichshafen AG) for their active support.

Moreover, part of the experimental results in the dissertation was produced during a research stay at Department of Civil and Mechanical Engineering of Technical University of Denmark (DTU). I would like to thank Associate Professor Chris Valentin Nielsen and Mr. Ulfar Arinbjarnar for the support and cooperation during my research stay in Copenhagen.

I would like to express my special thanks to my parents Chenggui Wu and Lei Zhu for their continuous support and motivation throughout my educational and practical career. Finally, I would like to thank wholeheartedly my wife Chunyu Qian, who stood by me and supported me throughout my doctoral studies and the preparation of this dissertation. The published dissertation contributes also to my two lovely daughters, Zhongyu Anita and Yuqiao Sophie.

Mainz-Weisenau, in January, 2023

Yutian Wu

Contents

Formula characters, Latin letters

Characters	Unit	Definition
A	-	System elements
a	-	empirical factor depending on the tribological system
A_{Flange}	mm^2	Contact area in the flange region
D	mm	Diameter of sheet
D_0	mm	Initial diameter of sheet
d_P	mm	Diameter of punch
e	C	Amount of elementary charge
E_{el}	C/m^2	Electric field density
F_{BH}	N	Blank holder force in deep drawing
$F_{BH,min}$	N	Minimal blank holder force
F_{ff}	N	Friction force between blank holder and die (flange area) in deep drawing
F_{fr}	N	Friction force at the drawing radius
F_{id}	N	Ideal forming force
F_N	N	Normal force
F_p	N	Punch force
F_{rb}	N	Reverse bending force
$\widetilde{F_V}$		Specific wear force
H	MPa	Hardness of material
H_S	MPa	Hardness of sheet metal
H_T	MPa	Hardness of tool
i	A/m^2	Current density

I_{th}	A	Thermoelectric current
k	-	Wear coefficient
k'	-	Deviating wear coefficient
k_B	$J/kg \cdot °C$	Specific heat
L	m	Sliding length until severe wear occurs
Li	-	Likelihood function
l	mm	Sliding length
l_s	mm	Sample length
n	-	Exponent
N_f	-	Number of cycles
P	-	Character (of a system)
$\mathrm{P_{current}}$	A	Peak value of thermoelectric current
p_{BH}	MPa	Contact stress on the flange area
p_{uT}	MPa	Contact stress, from which severe wear of the tribological system occurs within a sliding length of 1 m
r	-	Residual
Ri	-	Interaction (within a system)
R	-	Stress ratio
R_a	μm	Arithmetic average of profile height
R_t	μm	Maximal height of the measured profile
R_z	μm	Peak to valley height of the profile, within a single sampling length l of five measurements
R_m	MPa	Maximal tensile stress
S	V/K	Seebeck coefficient

Sf	-	System function
S_a	µm	Arithmetic average of profile height (3d)
S_t	µm	Maximal height of the profile (3d)
S_z	µm	Maximal height of the profile (3d)
s_0	mm	(Initial) sheet thickness
s_1	mm	Sheet thickness after forming
T	K, °C	Temperature
T_{warm}	K, °C	Temperature of the warm side
U	V	Electric potential
U_{Th}	V	Thermal potential
w	-	Warm side
W	µm; µm^2; µm^3	Wear amount (1d, 2d, 3d)
z_a	µm	Asperity height
z	µm	Penetration of asperities

Formula characters, Greek letters

Characters	Unit	Definition
α	°	Wrap angle
$\hat{\alpha}$	-	Fitting parameter
$\hat{\beta}$	-	Fitting parameter
α_t	°	Taper angle
σ_R	$\Omega \cdot m$	Specific electric resistance
σ_N	MPa	Contact pressure
σ_{max}	MPa	Stress amplitude

σ_{∞}	MPa	Stress limit, under which an infinite number of fatigue load cycles can be achieved by the material
σ_{uT}	MPa	Ultimate tensile strength
ΔT	$K, ℃$	Temperature rise
ε	-	Random error
ε_F	J	Fermi energy
Φ	-	Standard normal distribution
μ_c	J	Average energy of electrons
μ_N	-	Friction coefficient between the blank holder and sheet metal
μ_R	-	Friction coefficient at the radius

Abbreviations

Abbreviation	**Definition**
2D	2-dimensional roughness measurement
3D	3-dimensional roughness measurement
2d	2-dimensional
3d	3-dimensional
Ac	Accuracy
AE	Acoustic emission
AHSS	Advanced high-strength-steels
Ap	Applicability in the industry
BH	Blank holder
BUT	Bending under tension
COF	Coefficient of friction

Ct	Cost
DB	Draw bead test
DTU	Technical University of Denmark
EDT	Electrical discharge texturing
FD	Flat Die Test
FE	Finite Element
GPS	Geometrical Product Specifications
MSE	Mean square error
MT	Maturity of technology
PQ	Possibility for Quantification
PDF	Probability density function
PtU	Institute for Production Engineering and Forming Machines
PVD	Physical Vapour Deposition
RT	Real-time property
S	Sheet
SBMF	Sheet-bulk metal forming
SDT	Strip drawing test
Se	Sensibility
SEM	Scanning electron microscope
SOFS	Slider-on-flat-surface
SMF	Sheet metal forming
S-N Curve	Stress-cycle curve for fatigue strength analysis
SRT	Strip reduction test
TD	Thermal diffusion
UHSS	Ultra-high-strength-steels

Un	Uniqueness
VA	Visual assessment
WRD	Wear resistance diagram

1 Introduction

A better understanding and control of tool wear in metal forming is a key to higher resource efficiency for the following reasons: Firstly, it allows for a broader usage of ultra-high strength steels or aluminum alloys. The proper use of advanced high-strength-steels (AHSS) and ultra-high-strength-steels (UHSS), such as dual-phase and micro alloy steels, allows for the use of thinner sheets that have identical mechanical performance, resulting in mass reduction and a smaller impact on the environment [TIS18]. These metals are therefore important for realizing an expansion and enhancement of lightweight design, but require higher forming and blank holder forces [TSC06]. At the same time, the reduced thickness leads to failure during deep drawing through instabilities such as wrinkling. In order to avoid these instabilities, higher forming loads are required, which create more severe tribological conditions. Besides high contact stresses, elevated process temperatures at the radii of deep drawing tools can also be observed [KIM08]. These factors provoke pre-mature adhesive and abrasive wear and shorten tool lives [GRO11]. Secondly, over-engineering of tool materials and surface treatments could be avoided. For example, in some cases, tool hardness is adjusted to values higher than necessary. Sometimes, surface treatments are needlessly laborious. Coatings, which are applied in many cases for enhancing the life span of forming tools, might not be necessary in some industrial processes. Although such kind of “over-engineering” can avoid premature wear of tools in sheet metal forming, it leads to a higher cost for tool manufacturing, especially for small batch productions [GRO13a]. Therefore, improved wear control helps in tool designing to be just as resistant to wear as is necessary. This could foster the economic production of small batches with cost-efficient tools.

The transformation of the concept of “over-engineering” to “lean construction” was first proposed about 30 years ago [WEB94]. In the context of wear control in sheet metal forming, a better understanding of the wear development is beneficial for increased accuracy in wear prediction and therefore a more

reliable plan for maintenance intervals of forming tools. This could pave the way to lean construction and robust forming processes for AHSS and UHSS. As a result, fewer scrap parts would be produced and a stable control of surface finishing could be achieved [TSU18].Thirdly, lubrication states could be adjusted to more environmentally friendly conditions without jeopardizing required tool lives, which aggravates the tool wear control significantly. Adequate adjustments minimize the amount of lubricant or remove environmentally hazardous components of the lubricant [BAY10]. Fourthly, improved control of tool wear paves the way for more stable process conditions, which lead to smaller fluctuations of process results. Therefore, tighter tolerances in product properties, especially surface quality, would be achievable [TSU18].

For these reasons, a better understanding and control of tool wear is a key factor for efficient sheet metal processing. A better understanding of tool wear can reduce variations in processes and thus allow for tighter tolerances in product properties.

2 State of the art

In this chapter, an overview of the topics investigated in this work is presented. The negative influence of the occurrence of premature wear on sheet metal forming processes is described. Based on the fundamentals of tribology, the methods of wear prediction and detection are reviewed and evaluated. Finally, tribometers characterizing the wear behavior are presented.

2.1 Sheet forming processes

Sheet metal forming is one of the most important processes in industry. In recent years, the demand for sheet metal parts with different shapes and properties has increased dramatically due to the development of modern industry. In recent decades, various methods have been developed to form high-strength, low-plasticity and difficult-to-form materials as well as complex-shaped parts [RAM10].

2.1.1 Deep drawing

Deep drawing is a widely applied process in sheet metal forming. According to DIN 8584-1, this process is classified as tensile-compressive forming. It is characterized as the deformation of a blanked sheet metal to form a hollow cup without the change of the sheet metal thickness [REC20]. The reduction of the diameter of the hollow cup can also be achieved through deep drawing. The process principal is shown in Figure 1.

In the first step, the blanked sheet is pressed between the blank holder and the forming die through a blank holder force. Next, the punch moves relative to the blank holder and forming die and deforms the sheet. The forming process requires a punch force (F_p), which consists of four parts: the ideal forming force (F_{id}), the reverse bending force (F_{rb}), the friction force at the drawing radius (F_{fr}), and the friction force between blank holder and die (flange area) (F_{ff}) [PAN61, SIE32]:

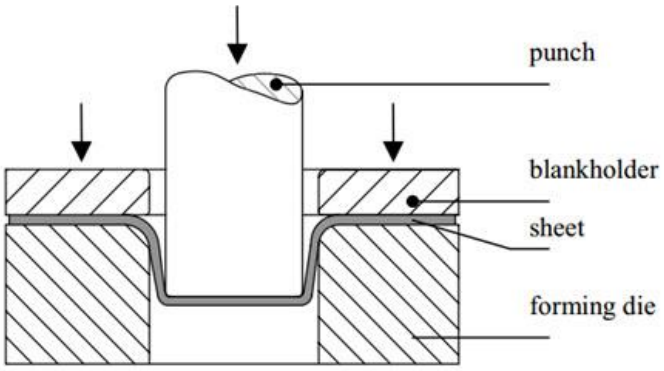

Figure 1 Principle schematic of deep drawing [GON11]

$$F_p = F_{id} + F_{rb} + F_{fr} + F_{ff} \quad (1)$$

In equation (1), the terms F_{fr} and F_{ff} are induced through friction between forming tools and sheet metal, which results in wear directly. The friction force between blank holder and die in the flange area can be described by the following equation:

$$F_{ff} = F_{BH} \cdot 2\mu_N \cdot \frac{d_P}{D} \quad (2)$$

F_{BH} corresponds to the blank holder force, μ_N is the friction coefficient between the blank holder and sheet, d_P the diameter of the punch and D the diameter of the sheet.

The friction force on the die radius can be calculated through the theory of belt friction according to Euler-Eytelwein [EYT32].

$$F_{fr} = (e^{\mu_R \cdot \alpha} - 1) \cdot \left(F_{id} + F_{ff}\right) \quad (3)$$

1st and 2nd order wrinkling [SIM89], and fracture [WAN74] are the most common failure modes in deep drawing. Especially, due to the utilization of high-strength and ultra-high-strength-steel, the problem of 1st order wrinkling is becoming critical where blank holder force is inadequate [YAO11].

Tschaetsch has proposed an equation for the minimal necessary blank holder force for avoiding wrinkling in deep drawing of a sheet with a tensile strength of R_m [TSC06]:

$$F_{BH,min} = A_{Flange} \cdot p_{BH} \quad (4)$$

$$= A_{Flange} \cdot 0{,}002 \left(\left(\frac{D_0}{d_P} - 1 \right)^2 + 0{,}5 \cdot \left(\frac{d_P}{100 \cdot s_0} \right) \right) \cdot R_m$$

In equation (4), D_0 stands for the initial diameter of the blanked sheet, s_0 the thickness of sheet, p_{BH} the contact stress underneath the blank holder and A_{Flange} the contact area in the flange region. It shows that the minimal necessary blank holder force is proportional to the tensile strength R_m of the used sheet.

Combining the equations (2) – (4), the friction forces F_{fr} and F_{ff} increase by the use of high-strength and ultra-high-strength steels. This increase of the friction force is a potential risk for wear occurrence.

2.1.2 Sheet-bulk metal forming (SBMF)

The concept of “sheet-bulk metal forming (SBMF)” is relatively new within metal forming. The raw material for SBMF is a sheet of a thickness between 1 and 5mm. This kind of sheet forming has a three-dimensional material flow with thickness changes of the sheet metal [MER12a], while the material flow of the conventional sheet metal forming is two-dimensional without an intended thickness change. Contact stresses in forging can reach up to 2500 MPa [BAY94], so tool wear is also an issue in SBMF tribology. The different types of SBMF are shown in Figure 2.

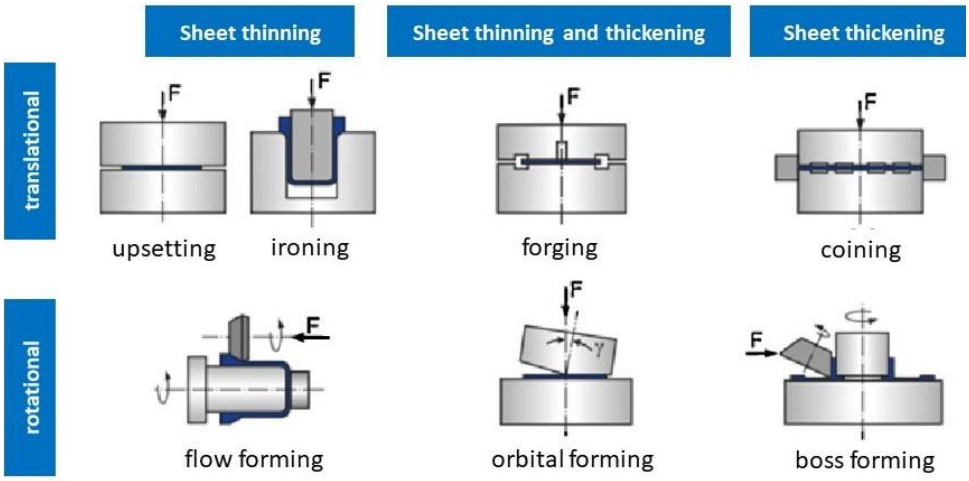

Figure 2 Classification of SBMF (modified figure from [MER11])

In this work, two SBMF processes serve as case studies for wear prediction (discussed in Chapter 7), the ironing process and gear processing.

Ironing

Ironing is a process of smoothing and thinning the wall of a shell or cup by forcing it through a die with a punch. It often follows a deep drawing process and leads to a reduced wall thickness. According to Figure 2, ironing is a translational sheet thinning process in SBMF. The principle of ironing is shown in Figure 3.

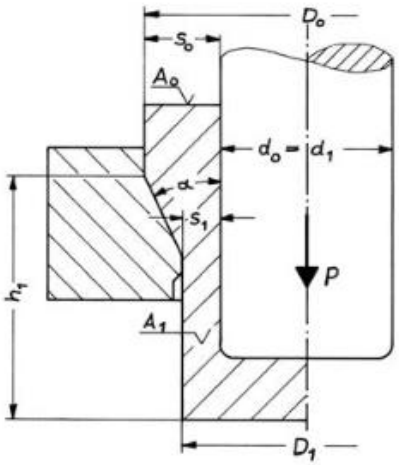

Figure 3 Principle of ironing [TSC06]

In Figure 3, the wall of the cup is reduced from s_0 to s_1. The reduction $\frac{s_0-s_1}{s_0}$ leads to a high friction force on the forming tools. With an increase of reduction, the friction force in the forming zone increases correspondingly. According to the experimental results of Saito, an increment of the reduction by a factor of 1.7 can lead to an increase of the friction force by more than a factor of 3.5 and it also leads to a more significant tendency of galling initiation on the forming tools [SAI89]. Moreover, in the combined deep drawing-ironing procedure, the ironing process is often situated as downstream process after the deep drawing. The initial amount of lubricant on the work piece is often scrapped off before the ironing process. Therefore, the amount of lubricant is drastically reduced and the friction situation is even more severe [HOL12]. Because of this sensitivity of wear occurrence, the wear behavior in ironing processes will be studied in this work.

SBMF of gear

The SBMF of a gear has been used to manufacture a clutch hub in automobile industry (see Figure 4). This process is similar to the “plate forging” presented in the work of Nakano [NAK01]. Compared to the conventional forging of billets, plate forging can both shorten the process chain (see Figure 5) and reduce the press force [MER12b]. Therefore, it has received more attention in the past ten years.

Figure 4 Clutch hub after gear forming (Source: ZF Friedrichshafen AG)

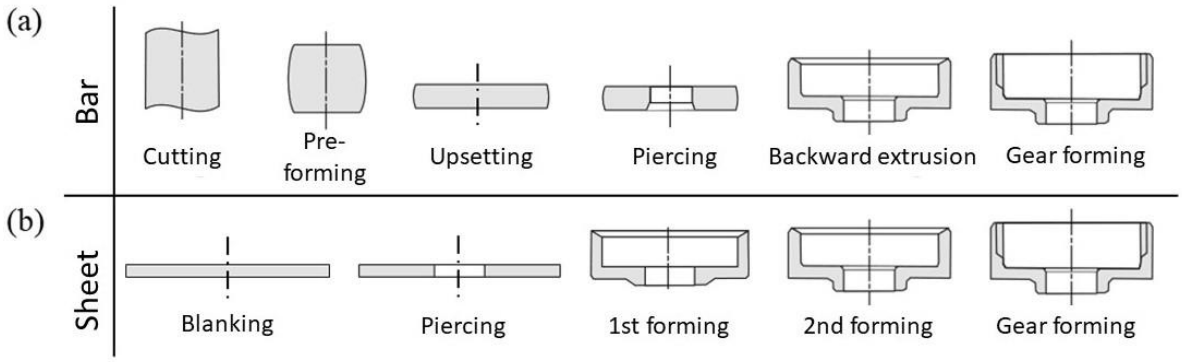

Figure 5 The difference between conventional billet forging and plate forging (Modified from [NAK09])

In the SBMF gear forming, cold forging is deployed on the sheet metal with a thickness of up to 5 mm. The sheet material flow is three-dimensional and both sheet thinning and thickening occur. Due to high contact stresses, tool life is reduced by premature tool wear [MER12b], which causes higher material cost

because of scrap production. Therefore, the wear issue in gear forming should be taken into account.

2.2 Basics of tribology

Friction force is an important component of the whole process force (for example the punch force in press) in the introduced forming processes. The study of friction, wear and lubrication is called “tribology”, which is derived from the Greek word “tribos” meaning rubbing and sliding [GOH18].

Wear is a major cause of material scrap and production failure. Any control over or reduction of wear implies considerable production savings in mechanical processing. It is estimated that one-third of the world's energy resources in present use is needed to overcome friction and wear [STA06]. As discussed in chapter 1, more and more high-strength and ultra-high-strength steels are required to be used in forming processes. As a result, the friction forces of forming processes rise accordingly in all mentioned processes such as deep drawing, ironing and sheet-bulk forming (see Section 2.1), which leads to a premature wear occurrence on the forming tools. In this section, the basics of tribology are discussed.

2.2.1 Tribological system

Devices and processes are often regarded as a technical system when analyzing their function [EHR13]. The system and its environment are separated by a virtual system boundary. A technical system is described through its “system function” and “system structure”. The “system function” is defined as the transformation of operational input variables into functional output variables and is determined by the system structure. The “system structure” consists of system elements (A), the character (P) and interaction (R) of the elements, which can be modelled as followed [CZI10]:

$$S = \{A, P, R\}$$

A tribological system in forming technology can be classified as a “mass transfer” system according to Czichos [CZI10]. The structure of a tribological system is illustrated Figure 6:

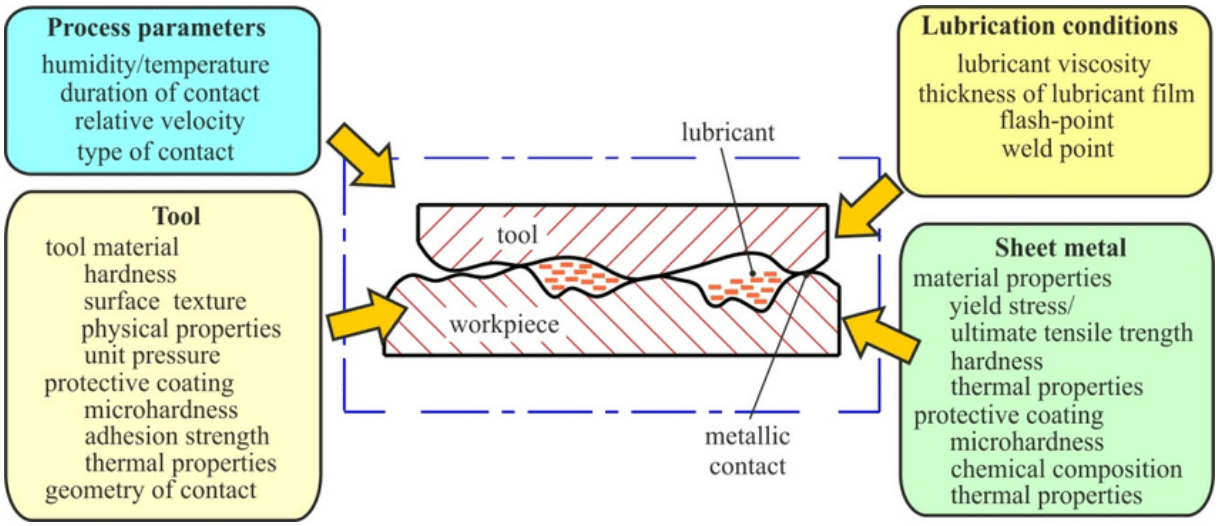

Figure 6 Illustration of a tribological system in metal forming [TRZ19]

In a general view of tribology, a tribological system consists of two contact bodies, the base and counter body, the intermediate substance and the load collective [KÖN06]. In view of metal forming, tool and workpiece are in contact and play a role as base and counter body. Between tool and workpiece, the lubricant can be regarded as the intermediate substance. Process parameters such as contact stress, relative velocity and tool temperature are regarded as the load collective of the tribological system [TRZ19].

2.2.2 Technical surface and its influence on friction

The contact pair in sheet metal forming, tool and sheet metal surfaces, are not perfectly flat. A periodic profile of surface roughness can be found on a milled and ground surface [HAS03, OST13]. For sheet metals, the electrical discharge texturing (EDT) method is widely used for surface texturing of sheets [SIM94]. The application of stochastic surface structure such as EDT can enhance the tribological conditions of sheet metal forming processes [STE96]. Because of this character, the actual contact between tools and sheet metal is in a local area, which is much smaller than the apparent contact area. Figure 7 illustrates this actual contact. The actual contact areas are formed through the contact between the peaks of the roughness asperities. A high concentration of contact stress takes place in these actual contact areas [CZI10].

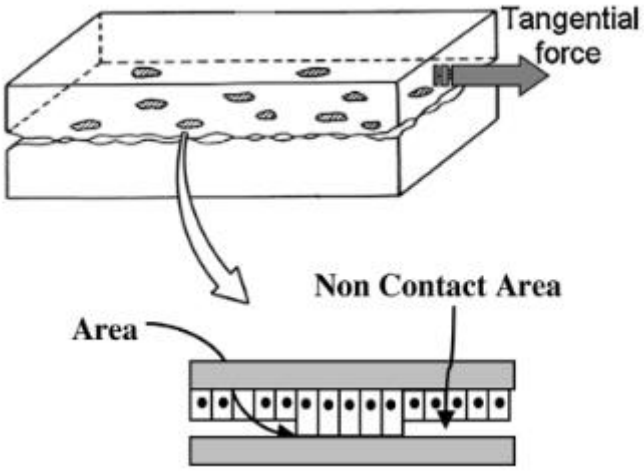

Figure 7 Actual contact area of contact pair [AVL15]

The concentration of the contact stress leads to plastic deformations of the asperities in contact. The contact model put forward by Westeneng explains the flattening effect, since the normal contact stress not only leads to the crushing of asperity peaks, but also leads to the rise of asperity valleys [WES03]. Moreover, the strains during deformation of arbitrarily shaped asperities also influence the flattening of the contact surface [HOL12].

The high contact stress on the asperities also causes the concentration of frictional heat in a tribological system, which is shown in Figure 8. Since the actual contact area is considerably smaller than the apparent contact area, the frictional energy and resulting heat at these contacts become highly concentrated with a correspondingly large temperature rise. This effect influences the material properties of the contact partners locally due to different thermal expansion, which influences the behavior of friction and wear of the material [STA06].

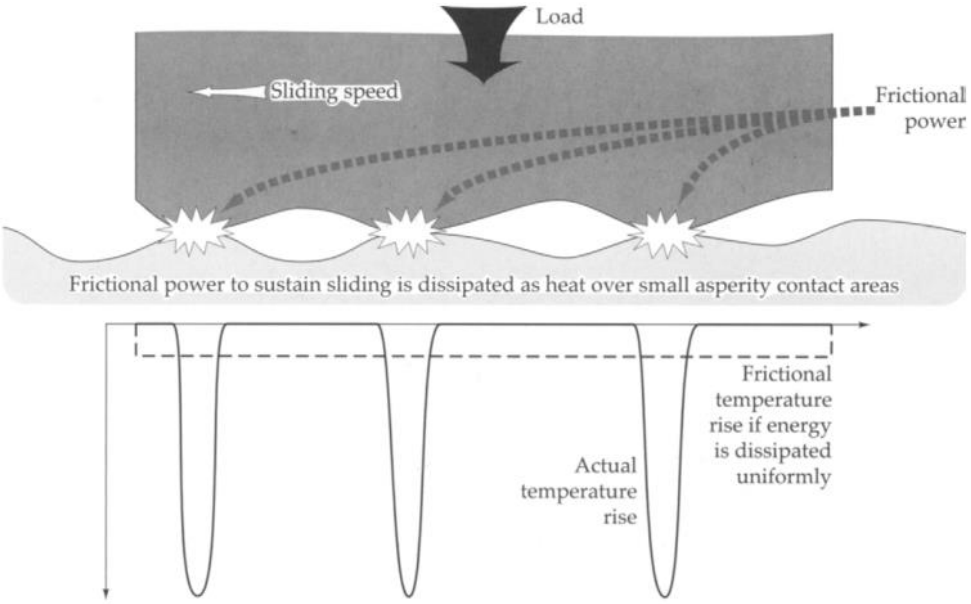

Figure 8 Concentration of frictional energy at the asperity contacts [STA06]

2.2.3 Characterizing the roughness of a technical surface

Surface roughness can be evaluated through tactile and optical measurement. For surface roughness quantification, several surface parameters are derived according to DIN EN ISO 4288:1998-04 (Geometrical Product Specifications (GPS) - Surface texture: Profile method - Rules and procedures for the assessment of surface texture) [DIN98]. In this section, the surface parameters used in this work are introduced.

Firstly, the parameters based on a 2-dimensional profile are described. R_a stands for the arithmetic average of profile height deviations from the mean line (see Figure 9) [AME19]. This parameter is widely used in industrial applications for tool wear evaluation [VOL05]. The minimal sample length l_s of the measured profile is also given by the DIN EN ISO 4288 [DIN98]. The mathematical equation can be described as the following:

$$R_a = \frac{1}{l}\int_0^{l_s} |z_a(x)|dx \tag{5}$$

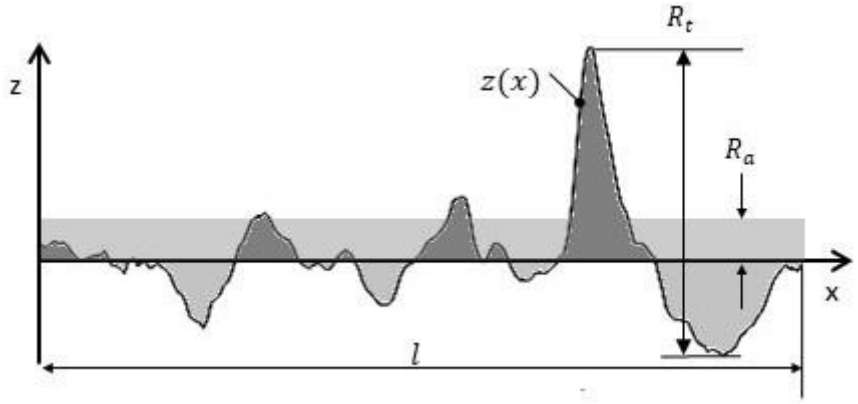

Figure 9 2-dimensional profile for surface roughness determination [REC20]

However, this characteristic value is not suitable for an objective description of different profile geometries, since it cannot distinguish the difference between peak and valley [REC20]. Moreover, local high peaks or deep valleys of a profile (local wear mark for example) cannot be detected sensibly enough for R_a. Another constraint with the utilization of the average roughness R_a is that totally different surface topographies can return similar values [BHU03].

For a description with better sensitivity for local peaks or valleys, the surface parameters R_z and R_t are used. R_z is defined as the peak to valley height of the profile z_i, within a single sampling length l_s of five measurements:

$$R_z = \frac{1}{5}\sum_{i=1}^{5} z_i \tag{6}$$

A much more sensitive surface parameter is R_t, the maximal height of the measured profile:

$$R_t = |\min z_a(x)| + |\max z_a(x)| \tag{7}$$

For a stochastic surface pattern, three-dimensional surface parameters are derived according to DIN EN ISO 25178-1 [DIN16]. The characterization of surface roughness is expanded from 2d profiles to a 3d curved surface. The 3d surface parameters S_a, S_z and S_t are equivalent to the 2d parameters R_a, R_z and R_t. According to DIN 25178, S_z and S_t are defined in the same way as: the maximal distance between the highest peak and the deepest valley. The equations for S_a, S_z and S_t can be written as follows:

$$S_a = \frac{1}{A}\iint_A |z_a(x,y)|dxdy \tag{8}$$

$$S_z = S_t = |\min z_a(x,y)| + |\max z_a(x,y)| \tag{9}$$

2.2.4 Wear mechanisms

According to “Gesellschaft für Tribologie e.V.” (German Society of Tribology), wear is defined as “Advanced material loss from the surface of a solid surface, which is caused by mechanical effects such as contact and relative motion” [DET02]. According to Williams, wear is a result of complex mechanical, physical and chemical interactions [WIL05b]. In metal forming, the failure of a workpiece can be defined as wear being so advanced that it leads to an inacceptable shape or dimensional change of the workpiece [HOF12].

The classification of the wear mechanism varies in the literature. A widely accepted classification is abrasion, adhesion, fatigue wear and tribochemical reaction [CZI10, TAK13], all of which are shown in Figure 10

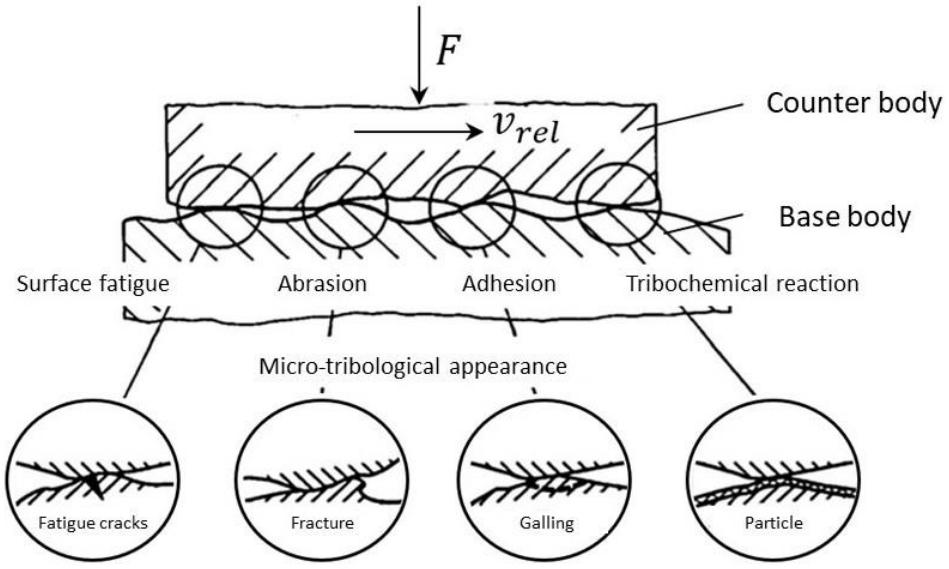

Figure 10 Basic wear mechanisms viewed microscopically (modified from [KOV09])

These four mechanisms are the highest level of classification. The other classifications are mainly a refinement of these four mechanisms. For example, Bayer classified the abrasive wear into abrasive wear resulting from single-cycle deformation and repeated cycle deformation [BAY04]. Kopeliovich has

separated the abrasive wear into two-body and three-body abrasive wear [KOP14]. The mechanism of tribochemical reaction is often separated into oxidation and corrosive wear in literature [STA06]. In the following part of the work, the discussion of wear mechanisms will be based on the four basic wear mechanisms shown in Figure 10. Some other wear mechanisms such as fretting [BAY04], erosive and cavitation wear [STA06] will not be discussed in this work, since they seldom take place in metal forming.

Abrasive wear

Abrasive wear is defined as a phenomenon that includes plastic deformation, removal of material or permanent displacement when a rough, hard surface rubs against a softer surface [BAY04]. The characteristics of the softer material determine the micro effects of the abrasive wear.

In terms of the micro effects, abrasive wear can be classified into microcutting, mircoploughing, microcracking and microfatigue (See Figure 11) [GAH88]. Microcutting is the classic form of abrasive wear, which occurs when a sharp and hard asperity cuts the softer surface, with only minimal or no displacement to both sides of the groove [STA06]. After the indention of a sharp asperity into a ductile, soft material, micro-ploughing occurs, where ridges are created along the wear groove [GAH87]. If the softer material is brittle, microcracking occurs when highly concentrated stress is imposed by abrasive particles [GAH88]. In this case, large wear debris is detached from the wearing surface. Repetitive microploughing can cause microfatigue.

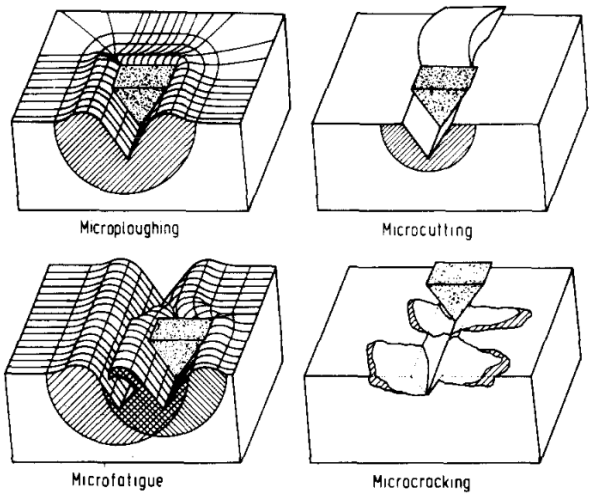

Figure 11 Physical interactions between abrasive particles and the surfaces of materials [GAH88]

The above-mentioned micro-effects are based on two body contact. Usually, the debris or abrasives detached from the two contact bodies participate in the sliding effect as well, which is known as the three-body effect [KOP14]. This also affects the wear behavior of the material [SAS84].

Fatigue Wear

Surface fatigue wear occurs on account of localized and progressive structural fracture under repeated cycling loading when the applied load is higher than the fatigue strength of the material. This can occur under sliding, rolling or impact conditions [KOP14].

Figure 12 illustrates the mechanism of surface crack fatigue wear schematically. A primary crack originates at some weak point of the surface and then propagates downward along weak planes such as slip planes or dislocation cell boundaries. A secondary crack can develop from the primary crack or alternatively the primary crack can connect with an existing subsurface crack. Finally, a wear particle is released when the developing crack reaches the surface again [BUC81].

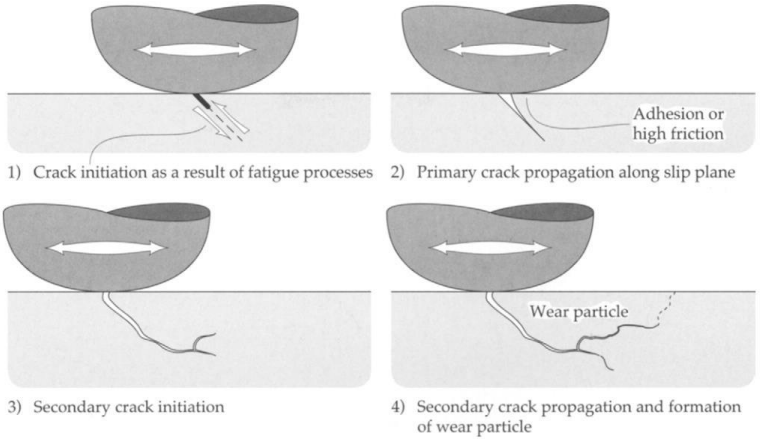

Figure 12 Procedure of fatigue wear [STA06]

According to Timoshenko, the maximum shear stress in the counter body of a line contact or a point contact is not located directly on the surface, but at a distance below the contact surface. This distance correspond to the width of apparent contact area [TIM70]. Hence, the fatigue wear is hazardous for materials with internal defects (such as pores and micro-cracks) which can be found e.g. in grey iron.

As discussed above, fatigue wear may not occur in short term sliding processes, but it is harmful in a long-term sliding process, since the crack initiation and propagation occurs inside the surface of the contact pair have an incubation phase, which is hard to predict. Moreover, the material loss due to the fatigue wear is high and harmful [BAY04]. Therefore, a detection of such fatigue wear in due time is necessary.

Adhesive wear

Adhesive wear is a very serious form of wear. It is defined as a phenomenon which occurs on account of the removal of material from the less wear-resistant surface by sufficient separation force [BAY04].

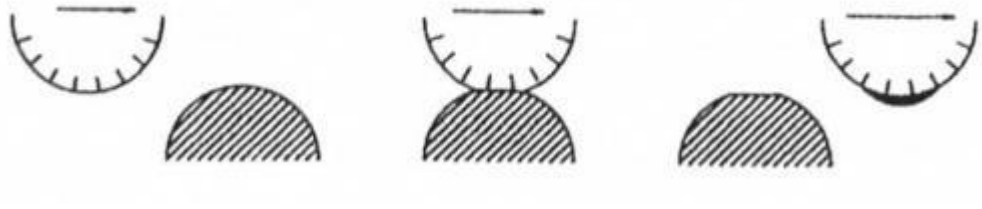

Figure 13 Conceptual illustration of adhesive wear mechanism [BAY04]

Galling is a severe type of adhesive wear on tools in sheet metal forming. Galling is often defined as a term for seizure of the sheet surface and is often observed as a consequence of transfer of sheet material to the tool surface. It is a phenomenon in which the frictional force abruptly increases under specific conditions at the contact surface due to microscopic welding [YOO13]. Because of the welding, wear marks cause a severe scratching on the sheet surface [SCH93]. After occurrence of galling, the normal operation of mechanical systems such as forming tools in sheet metal forming is impossible. In most sliding contacts, such as bearings, gears, chains and cams, it is the cause of rapid and sometimes catastrophic failures [STA06]. Therefore, the control of adhesive wear is essential.

Tribochemical reaction

Tribochemical reaction is a chemical reaction that occurs during the friction process, which takes place between contact bodies or between one of the contact bodies and the lubricant [CHR16]. For metallic friction pairs, a brittle corrosion layer is sometimes produced due to oxidation, which causes material loss.

In metal forming, 50% of wear can be traced back to abrasion [WIL05a]. Abrasion and adhesion are the two dominating wear mechanisms in manufacturing technology [CZI10]. In sheet metal forming, fatigue wear should also be taken into account because of cyclic loading [PER09].

2.2.5 Wear models

For characterizing the wear amount, different kinds of wear models have been developed for various wear mechanisms. The most widely used model is Archard's wear model [ARC53]:

$$W = k\frac{pl}{H} \tag{10}$$

In this equation, W stands for the wear parameter, p the contact stress, l the sliding length, H the hardness of the softer contact material and k the wear coefficient. According to Habig, this wear parameter can be separated into three main groups: the direct, related and indirect parameters [HAB80]. The direct parameters can be 1d, 2d or 3d, which describes the wear amount. For example, the wear volume belongs to the 3d parameters, while the wear area is a 2d and the wear depth is a 1d parameter [CZI10]. In sheet metal forming, the surface roughness parameters introduced in section 2.2.3 are usually used for the characterization of wear severity [GRO13a].

The indirect parameters, on the other hand, are other physical parameters that reflect the wear severity. For example, in sheet metal forming, punch or drawing forces are usually used for wear severity evaluation [FIL04]. Similarly, the coefficient of friction (COF) is also used as a parameter in wear tests such as twist-compression-test [KIM08] and strip drawing test (SDT) [FIL04]. Based on these indirect parameters, methods for wear detection are developed and will be discussed in Section 2.5.

The important related parameters are mainly time (life span), sliding length until wear occurrence and wear work [KUW07]. Besides the direct wear parameters, the indirect method for wear prediction is based on relative parameters, which will be discussed in section 2.3.3.

Another important parameter of the wear model is the wear coefficient k, which is a parameter used to define the wear rate [BAY04]. The definition of k varies for different wear mechanisms.

For chemical processes, such as adhesion and tribochemical reaction, the wear coefficient k is an empirical value. It characterizes a probability of a chemical reaction between contact bodies resulting in wear. For adhesive wear, it represents the probability of adhesion between two junctions of two contacting bodies, which leads to wear. In tribochemical reaction, it means the probability of a chemical reaction of contact partners that leads to wear [BAY04].

For physical processes such as abrasion and fatigue, the wear coefficient k is determined by the geometry of asperities according to Rabinowicz [RAB66], which is shown in Figure 14.

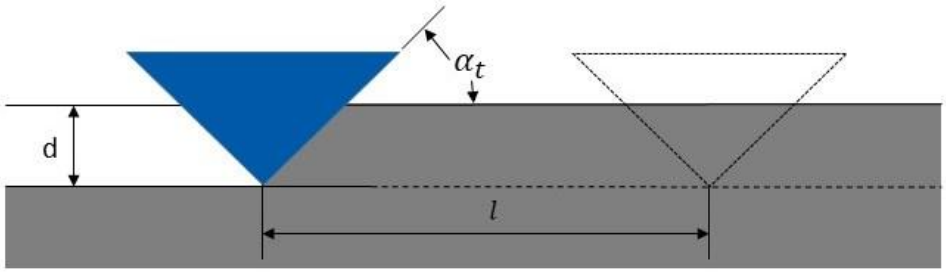

Figure 14 Model of abrasive wear by a single grit (modified from [STA06])

The wear coefficient k for a conical asperity can be written as followed:

$$k = \frac{2 \cdot tan\alpha_t}{\pi} \tag{11}$$

It shows that the taper angle α_t of the asperity determines the wear coefficient of abrasive wear.

Archard's wear model is applicable for characterizing wear in the classes abrasion, adhesion and tribochemical reaction. However, the wear model for fatigue wear is different from those of the other three wear mechanisms. Bayer has proposed the following equation [BAY04]:

$$W = k \cdot p^n \cdot l, n > 1 \tag{12}$$

In this equation, two differences compared to Archard's wear model can be identified. Firstly, the dependency on hardness is eliminated. Secondly, the load factor is non-linear instead of linear. The value of the power n varies for different materials. The n-values of most materials are more than 1 [CLA87]. It is obvious from equation (12) that fatigue wear is very sensitive to the variation of load.

2.3 Approaches for wear prediction

2.3.1 Wear development

According to Habig, the typical wear development of steel parts can be divided into three phases: running-in, steady-state and failure (see Figure 15) [HAB80].

In the running-in phase, wear development is regressive. As a result of surface roughening, the wear rate during running-in is relatively high [BAY04]. The duration and behavior of the running-in phase is determined by the distribution of the energy in the tribological system [BLA05]. According to Kragelsky, reaching the optimal load-carrying capacity of a surface means the end of running-in and the start of steady-state, which implies the influence of surface roughness on the behavior of running-in [KRA69].

After the initial phase with a high wear rate, the wear development starts to stabilize and turns into a steady-state condition. In this phase, the wear rate is constant and the duration is relatively long. After steady-state, failure occurs, which shows an exponential development. The sliding length or the process time at the transition between these two phases can be defined as the life span of the tribological system. The transition of the phase of the wear development can be regarded as the transition of the wear mechanism from mild wear such as abrasion to more severe wear such as fatigue wear according to Bayer [BAY04]. Czichos states that the wear mechanisms, which take place after failure, are not unique. Instead, the superposition of the basic wear mechanisms also leads to the rapid increase of the wear rate [CZI10].

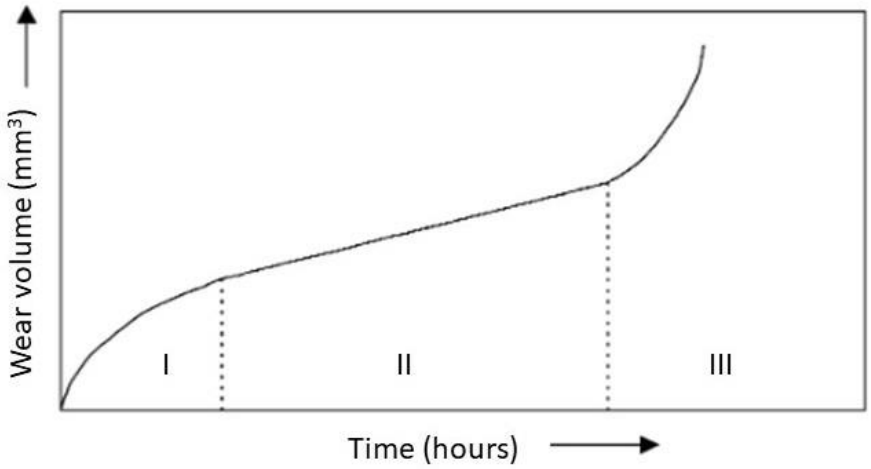

Figure 15 Typical wear development (I) running-in; (II) steady-state; (III) failure (modified figure from [KUM02])

In sheet metal forming, Christiany has deployed numerous conditions in the strip drawing test for characterizing tool wear behavior [CHR16]. Similar to typical wear development, tool wear also experiences three phases where the

dominating wear mechanism varies in different phases [GRO13a]. Due to this abrupt occurrence of “failure”, the prediction of wear and life span estimation is a challenge in designing and controlling manufacturing processes. The wear prediction is separated into direct and indirect methods, which are discussed in the following sections.

2.3.2 Direct wear prediction methods

For direct wear prediction, the wear models discussed in section 2.2.5 are used to calculate the wear amount (volume, area or depth) directly. The wear prediction in metal forming is often based on Archard’s wear model (Equation 10) through the calculation of the load p by numerical simulations, the hardness H and the wear coefficient k through experimental approaches.

Several other models are proposed through optimization of Archard’s wear. In bulk forming, Behrens proposed the following model [BEH08]:

$$W = k\frac{pl}{H(T)} \tag{11}$$

Compared to equation 10, the temperature dependent hardness $H(T)$ is proposed, since the contact temperature in bulk forming can reach more than 600℃ and its influence on the material hardness is not negligible.

By using the wear prediction methods, it is possible to calculate the wear amount through numerical simulation and material characterization. The determination of the wear coefficient k, which is done empirically, is one of the main constraints of this approach. Because of this, the transition of the wear mechanism is hard to predict. The typical wear models and their applications in metal forming are summarized in Table 1.

Table 1 Summary of the wear prediction model

Wear parameter	Forming process	Wear model	Relevant literature
Wear volume	Deep drawing	Archard	[SOB92], [WAN11], [HOR01], [HOF05], [WAN13], [XIA07]

Wear volume	Stamping		[PER10], [PER08]
Wear depth	Wire drawing		[KIM97]
Wear depth	Forging		[BEH08]
Contour	Hot extrusion		[PAI96]
Wear depth	Cold rotary forging		[HAN13]
Wear depth	Extrusion forging	Behrens	[CHO12]
Wear depth	Forging		[BEH17a]
Wear depth	Deep drawing	Archard modified with energy approach	[ERS08]

Ersoy proposed a wear model based on an energy approach for wear prediction in deep drawing processes. It is assumed that wear is directly related to the dissipated energy. The tribological condition will change, if a certain amount of work or dissipated energy accumulates at a certain location. Fatigue fracture occurs when the total energy reaches a certain constant value for a given material [ERS08]. With the help of this method, the transition of mechanisms is predictable. Nevertheless, the threshold value of dissipated energy is also an empirical value. For life span estimation, a database of threshold values would be necessary.

2.3.3 Indirect wear prediction methods

Besides the direct wear prediction, some other indirect method can also be used for wear prediction. These methods are based on the relative wear parameters described in section 2.3.1.

Ashby and Lim proposed a concept for the prediction of the dominating wear mechanism. The so called “wear mechanism map” is based on data gained in pin-on-disc tests [LIM87]. This map offers a database for the analysis of influencing parameters such as sliding velocity and normalized pressure on the wear coefficient and the dominating mechanism. If the parameters of the load collective are known, the wear coefficient and the resulting wear mechanism for

a specific tribological system can be estimated through the wear map (see Figure 16).

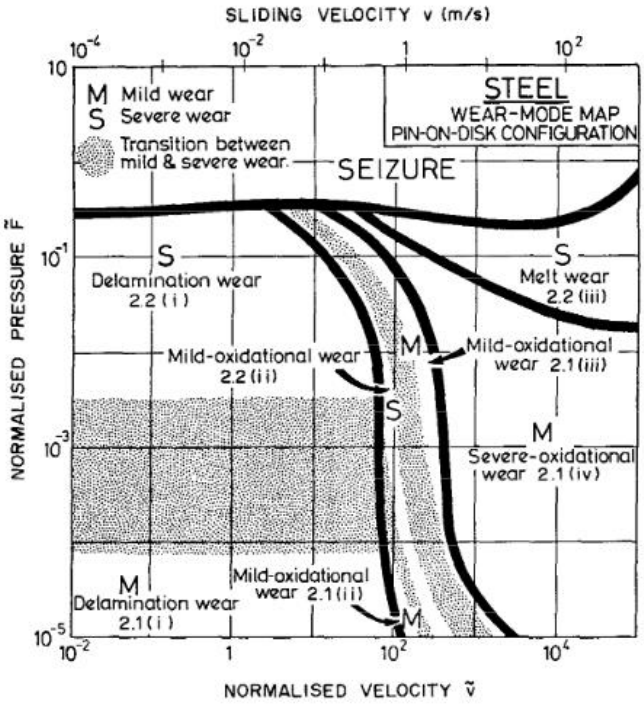

Figure 16 Wear mechanism map according to Lim and Ashby [LIM87]

In addition, in metal forming, a method for wear prediction using the life span estimation through a wear resistance diagram (WRD) was developed [GRO19a], which is inspired from the stress-cycle (S-N) curves for fatigue strength analysis (see Figure 17). These diagrams have been used to characterize the wear resistance of different tribological systems in laboratory tests [CHR16]. The WRD illustrates the life span of tools under different contact stresses, quantified by the attainable sliding length until wear occurrence in a strip drawing test. The results of previous studies show that the life spans deviate drastically at different load levels, not only in terms of the absolute value of life span, but also in the variation of the life span under the same nominal conditions. At lower load levels, the obtained life span and its deviation increase significantly, while at higher load levels the life span is significantly smaller and its deviation decreases distinctively [GRO19a].

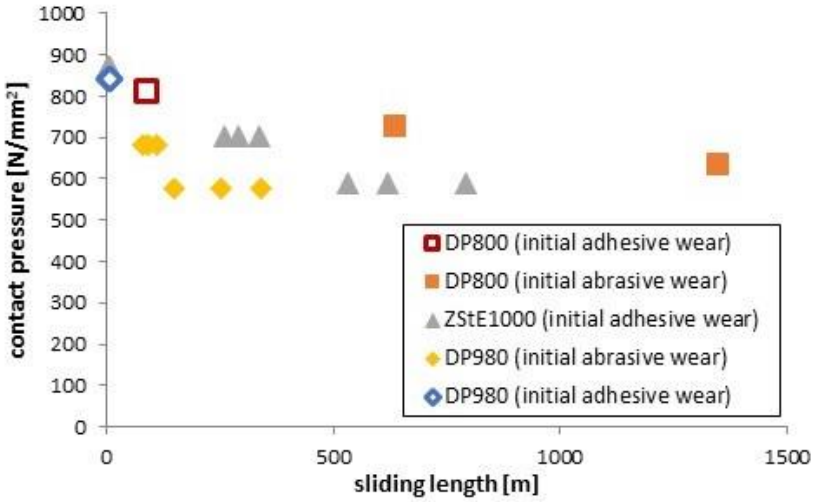

Figure 17 Wear resistance diagram (WRD): comparison between contact pressure and reachable sliding length [GRO19a]

With the help of this approach, the evaluation of the life spans of tribological systems under different contact pressures is possible. For a deeper understanding of the influence of the sheet metal strength, another characteristic value, the specific wear force $\widetilde{F_V}$, is derived. It takes into account the resulting friction force, which leads to wear after a characteristic sliding length. The equation of the specific wear force is as following:

$$\widetilde{F_V} = \frac{{\sigma_N}^2 z}{H_T}\left(\frac{H_S}{H_T}\right)^n \tag{13}$$

This mathematical model demonstrates that the hardness of tools H_T and sheets H_S as well as the penetration of asperities z have an influence on the specific wear force. With the help of wear resistance characteristic curves, it is possible to analyze the wear development and approximate the life span of a forming tool when forming different sheet metal materials with similar material structure but different tensile strengths [GRO19a] (see Figure 18).

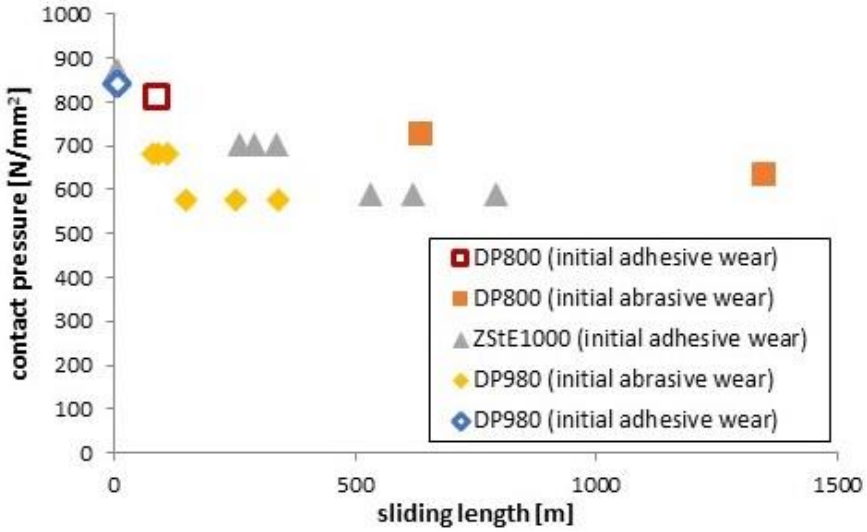

Figure 18 Wear resistance diagram (WRD) by applying specific wear force [GRO19a]

The penetration of asperities z is obtained after the approach of Tsukizoe, which is relevant to surface hardness and roughness [TSU65]. In addition, the effect of the exponent n on the relative hardness $\frac{H_S}{H_T}$ is not clear because of the lack in research on the influence of hardness. Therefore, more information about the influence of hardness and surface roughness is required.

Due to the development of the WRD, the wear resistance of a tribological system can be estimated through model tests such as strip drawing tests, which will be introduced in section 2.7.2.

Moreover, the load-dependent life spans can be estimated through WRD. Nevertheless, the influence of hardness and roughness should be defined according to the model of specific wear force (Equation 13). For an accurate wear prediction, a characterization of influence of hardness and roughness on the life span is necessary as well.

2.4 Recent study on the influence of hardness and roughness

Hardness is an essential property for the evaluation of wear resistance. Archard's and Rabinowicz's wear models indicate that the abrasive wear rate of a tribological system increases with a decreasing hardness of the softer

contacting body. However, results gained in pin abrasion tests show that the hardness is not the only relevant property which influences the abrasive wear of the material. Additionally, the ductility or the grade of case hardening are also important factors. For a softer and more ductile material, microploughing occurs, while harmful wear such as mircocracking with high material loss will occur for a harder matter (see Figure 11) [GAH88]. For adhesive wear, Bayer's wear model assume that the material properties of the contact pair (the wear coefficient k) play a more important role than the hardness itself [BAY04].

In terms of surface roughness, Bayer and Sirico found that wear resistance increases with decreasing roughness up to a specific value in their wear experiments. Beyond this value the wear resistance did not improve with an improved surface roughness [BAY75]. In dry forming, surfaces with lower roughness show a reduced risk of galling [HAN08]. Kumar has discussed that the initial roughness and coefficient of friction determine the wear rate in steady-state for E31 steel [KUM02]. On the contrary, for a tribological system that includes lubricant, the inclusion of lubricant pockets on tools made by machine hammer peening is found to be favorable. The positive influence of such lubricant pockets on the friction and wear behavior has been proven [STE15]. In a lubricated tribosystem, the application of proper surface texture leads to an extended life time [PET03].

In sheet metal forming, tools made from cold working steel are usually engineered to be as hard as possible and the surfaces treated or polished to be as smooth as possible. Although these measures can lead to a high wear resistance, it is not resource efficient in terms of small or middle-batch production. Therefore, a life span estimation through WRD, taking hardness into account, should be considered for those fields of application.

The above-mentioned methods for wear prediction pave the way towards an effective control of wear. Besides wear prediction, effective detection of wear is also an important prerequisite for wear control.

2.5 Methods for wear detection

Due to the characteristics of the tribological system (see section 2.2.1) and the character of wear development (see section 2.3.1), the wear occurrence (start of failure of wear development in Figure 15) is difficult to detect accurately. Table 33 offers an overview of methods for wear detection found in academic journals. Generally, nine different methods are applied, ranging from the classical, qualitative such as visual assessment (VA) to newly developed inline methods such as acoustic emission (AE). In this section, the methods used for wear detection in sheet metal forming are reviewed and benchmarked to offer an overview of recent approaches for wear control based on 29 pieces of literature that showcase some methods for wear detection (See Appendix 3).

2.5.1 Visual Assessment

So far, the detection of wear in forming technologies is still mostly based on offline visual assessment and optical scan of the tool surface. The qualitative visual assessment is often used to determine the severity of wear on tooling and parts, and remains the most effective method for characterizing and identifying the wear severity [VOS17]. According to Table 33, almost all journal papers related to wear research use this visual assessment for the characterization of wear. Before the development of other detection methods around 1998, it was the most widely used method. Although it is a useful and direct method to identify wear, the process relies heavily on the experience of the examiner, since no quantitative data can be referenced. Moreover, the time delay between the occurrence of unacceptable wear and the result of the offline surface analyses increases the probability of scrap production in industrial processes.

2.5.2 Offline measurement (classic methods)

Besides the visual assessment, several offline approaches are used. Measurement of roughness and mass are the two main typical methods. In mass measurement, the evaluated part is weighed before and after sliding. The measured difference in weight is the wear mass. A positive difference denotes material loss, which implies abrasive wear, while a negative difference denotes material gain, which implies adhesive wear. After wear occurrence, the mass

difference is only about 0.02% according to [SKÅ03], which can be a challenge for the measurement accuracy. Because of this constraint, relatively few approaches use mass measurement for wear characterization.

In sheet metal forming, measurement of roughness is implemented for wear detection on the surfaces of workpiece or forming tools after specified intervals [GRO13a]. The measurement is deployed through confocal microscope [GRO19a] or scanning electron microscope (SEM) [GÅÅ09a]. After the measurement, the 2d and 3d surface parameters described in Section 2.2.3 are used for wear characterization. The accuracy of roughness measurement is guaranteed since roughness is a typical indicator of wear. The time delay between the wear occurrence and the pre-determined interval is a constraint for this method, which is similar to the visual assessment. Therefore, an in-process evaluation or inline measurement is necessary for wear detection.

2.5.3 In-process evaluation (Inline measurement)

Christiany integrated a confocal sensor into a strip drawing test for in-process roughness evaluation. He found that it shows a good agreement with the classical visual assessment [GRO13a]. The relatively long measurement period is the biggest constraint of this method. For example, the maximal measurement period of the chromatic confocal sensor is 0.125 s per mm [GRO13a]. The ironing process described in section 7.2.1 has a period of only 0.67 s for one stroke of production, with a sliding length of 30 mm. This efficiency of surface measurement does not meet the demand of the throughput time of modern metal forming processes.

The evaluation of COF or force is equivalent, both of which measure the process force (such as punch force) as an indicator of the wear. This method is widely used in actual processes [VAN01] and in different tribometers [FIL04, PUJ13]. Generally, the force evaluation offers a good efficiency of in-process wear monitoring. However, the tool wear is not the only cause of punch force variation. According to Chen, lubricant system failure accounts for 15% of failures in a punching machine. Other failures on the main drive system of a machine with an occurrence frequency of 23.5 % will also cause a change in the

punch force [CHE16]. In a recent study, signal features of punch force are studied to classify the defect in a blanking process [KUB21].

The temperature measurement is relatively seldom used for wear detection, since the peak contact temperature in tribological systems during sliding, the flash temperature according to Czichos [CZI10], is not measurable through the existing measurement technologies. For a contact temperature determination, a combination of an experimental and numerical approach is necessary. The approach of Üstünyagiz et al. showed a significant temperature drop of merely 1mm from the contact surface. Therefore, the sensitivity of the wear detection through temperature measurement with the status-quo measurement technology is limited [ÜST19].

The measurement of AE (acoustic emission) has been used for failure diagnosis in manufacturing processes in both machining and forming for more than 50 years [DOR92]. It is a non-destructive evaluation technique to detect material degradation. The initiation or propagation of a crack leads to a sudden release of energy within a solid body. The energy is dissipated in the form of elastic waves. This local, sudden energy release can be detected by audio devices attached to the surface. This whole process is called acoustic emission [SCR87]. According to Section 2.2.4, the wear mechanisms are based on the degradation of materials in a microscopic scale such as microcracking, microploughing, which offers the potential for application in wear detection. AE measurement was first investigated for wear detection in sheet metal forming in around 2010. Through the analysis of an AE signal in the time and frequency domains, the magnitude has a good correlation with conventional wear parameters such as roughness and the force signal [MOG17b]. According to Hase, different wear mechanisms have a specific frequency band of the AE signal in the frequency domain, which makes it possible to identify the dominating wear mechanism through the analysis of AE signals [HAS14]. Therefore, the AE-measurement is a wear detection method with high potential due to its high sampling rate and high sensitivity [GEN19].

2.5.4 Assessment of the wear detection methods

The aim of this section is to evaluate the status-quo methods for wear detection in sheet metal forming through benchmarking. The following criteria are set for this benchmarking: “Accuracy (Ac)”, “Sensitivity (Se)”, “Uniqueness for wear occurrence (Un)”, “Maturity of technology (MT)”, “Real-time property (RT)”, “Possibility for Quantification (PQ)”, “Applicability in the industry (Ap)” and “Cost (Ct)”. The benchmarking of assessment is defined in Table 2 .

Table 2 Benchmarking of the assessment

	1	2	3	4	5
Ac	excellent	good	satisfactory	sufficient	insufficient
Se	excellent	good	satisfactory	sufficient	insufficient
Un	unique		Light ambiguous		ambiguous
RT	excellent	good	satisfactory	sufficient	insufficient
PQ	excellent	good	satisfactory	sufficient	insufficient
MT	mature	Rooms for improvement	medium	Great potential	Totally new
Ap	Very easy	easy	medium	hard	Very hard
Ct	Very low	Low	Medium	high	Very high

The assessment of the above-mentioned methods for wear detection are summarized in Table 3.

Table 3 Assessment of the measurement methods

	VA	2D/3D	Mass	COF/Force	Temp	AE
Ac	2	1	5	3	5	2
Se	3	1	5	3	4	1
Un	1	1	3	5	3	1
RT	5	5	5	2	2	1

PQ	5	1	3	2	2	1
MT	1	1	1	1	4	4
Ap	1	3	2	1	4	3
Ct	1	3	1	2	2	5

From the assessment above, it can be found that the most popular wear detection methods such as visual assessment and roughness measurement have a good accuracy and good uniqueness for wear detection. However, the fatal disadvantage of the two methods is their real-time property. The detection of severe wear is always delayed and leads to scrap production. For wear detection in modern sheet forming, the real-time property becomes essential.

For an effective wear detection in metal forming, the wear detection method should have both good functionality (accuracy, sensitivity and uniqueness) and real-time property. Moreover, the cost of the measurement should also be taken into account, which is a disadvantage for AE measurement. In this work, a real-time, inline wear detection method based on thermoelectric measurement is introduced (see chapter 4.2). This approach is inspired by a study on the influence of thermoelectricity on wear, as described in section 2.6.

2.6 Influence of thermoelectricity on tribology

In this section, the influence of thermoelectricity on tribology are introduced in sheet metal forming. Thermoelectricity is a physical phenomenon of conducting or semi-conducting materials, which is widely used in temperature measurement devices such as thermocouples. At first, the basics of thermoelectricity are introduced and the application of thermoelectricity to tribology will be reviewed.

2.6.1 Basics of thermoelectricity

If both ends of a solid body have a temperature difference, electric charges in the bodies tend to displace. This effect is called thermodiffusion. The velocity of charge carriers is temperature- and location-dependent. The generated electric field causes the thermodiffusion to stop, and the moving charge carriers cause

the generation of thermoelectricity [ASH76]. This effect is called the Seebeck effect.

The Boltzmann transport equation offers a general relation of the electric field density E_{el} [CAL79]:

$$E_{el} = \frac{i}{\sigma_R} + S \cdot \frac{dT}{dz} - \frac{1}{e} \cdot \frac{d\mu_c}{dz} \tag{14}$$

where i is the current density, σ_R the specific resistance, S the Seebeck coefficient, $\frac{dT}{dz}$ the temperature gradient, e the amount of elementary charge ($e = 1.6 \times 10^{-19} C$) and $\frac{d\mu_c}{dz}$ the gradient of chemical potential.

The first term of equation 14 is the electric term, which corresponds to Ohm's law [OHM27]. The second term describes the thermodiffusion in a homogeneous lead material. The value of the Seebeck coefficient S is determined by the metallurgical composition and the temperature [DEM13]. The third term is the generated chemical energy. The chemical potential indicates the average energy μ_c of the electrons which contribute to the charge transport, which is determined by the Fermi energy ε_F and the thermal energy $k_B \cdot T$ [PEL05]. It is described mathematically through the following equation:

$$\mu \approx \varepsilon_F \cdot \left(1 - \frac{\pi^2}{12} \cdot \frac{k_B^2 T^2}{\varepsilon_F^2}\right) \tag{15}$$

It can be found that the chemical potential is determined by the chemical character of the material (Fermi-energy) and the temperature T. The chemical potential difference occurs not only within a material body, but also at the interface of two materials in contact [PEL05].

The electric potential has a relationship with the electric field density E, as described in the following equation:

$$U = \int E \, dz \tag{16}$$

A widely used temperature measuring device, the thermocouple, is based on the physical principles described in this section. A schematic explanation of the physical basis is shown in Figure 19. In equation 17, the electric potential within

the material $U_{TD,A}^{w\to k}$ and $U_{TD,B}^{k\to w}$ are composed of the thermal diffusion and chemical term, while the electric potential at the contact areas $U_K^{A/B}$ and $U_K^{B/A}$ are only dependent on the chemical potential difference.

$$U_{TD,A}^{w\to k} = -S_A \cdot (T_2 - T_1) + \frac{1}{e} \cdot [\mu_{cA}(T_2) - \mu_{cA}(T_1)]$$

$$U_K^{A/B} = -\frac{1}{e} \cdot [\mu_{cB}(T_1) - \mu_{cA}(T_1)]$$

$$U_{TD,B}^{k\to w} = S_B \cdot (T_2 - T_1) + \frac{1}{e} \cdot [\mu_{cB}(T_2) - \mu_{cB}(T_1)]$$

$$U_K^{B/A} = -\frac{1}{e} \cdot [\mu_{cA}(T_2) - \mu_{cB}(T_2)] \tag{17}$$

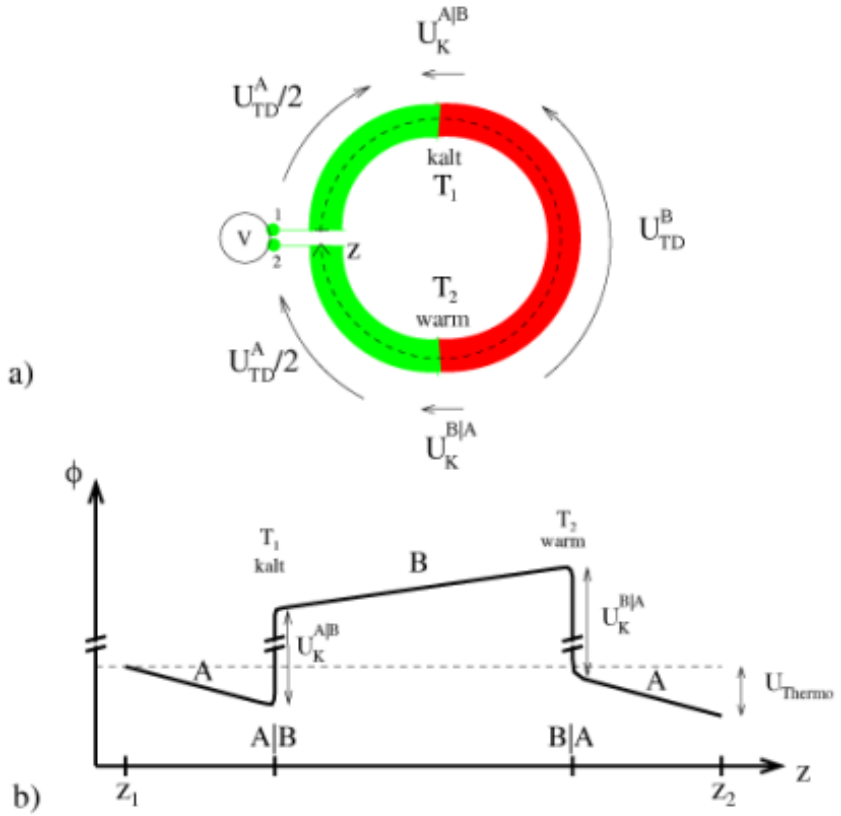

Figure 19 a) Schematic illustration of a thermocouple; b) Illustration of the electric potential in a thermocouple [PEL05]

The sum of the four equations is the thermal potential U_{Th}:

$$U_{Th} = (S_B - S_A) \cdot (T_2 - T_1) \quad (18)$$

From equation 18, it is found that the thermal potential is only related to the thermal term of equation 14. The terms related to the chemical potential are eliminated after summation of the “electric circuit”. The mathematical model U_{Th} is called the “Seebeck-effect”, which is dependent on the relative Seebeck coefficient $S_B - S_A$ and the temperature difference between the warm and cold side. It should be noted that the chemical potential actually exists according to Figure 19b and should not be ignored. Besides the application in thermocouples, other applications in metal forming are also based on thermoelectricity. This will be discussed in the following section.

2.6.2 Study of thermoelectricity in metal forming

In section 2.6.1, it is introduced that a chemical potential exists at the interface of two conductors in contact with two different materials ($U_K^{A/B}$ and $U_K^{B/A}$ of Figure 19). In sheet metal forming, tool and sheet materials are in most cases different. Hence, it is presumed that a chemical potential also exists between tool and sheet metal. Moreover, 95% of plastic and friction work contribute to the heat generation in the forming and contact zone, which also leads to a temperature gradient in the forming zone [TRÖ15]. This temperature difference leads to thermal diffusion in the solid materials of work piece and tool, which causes the formation of a potential difference within the work piece and tools.

Two main topics have been studied in terms of the effects of thermoelectricity in metal forming. Demmel proposed a method to measure the contact temperature between tool and workpiece through the determination of the Seebeck-coefficient, according to the following equation [DEM14, TRÖ18]:

$$U_{Th} = \int S \cdot T \frac{dT}{dz} \quad (19)$$

Compared to equation 14 and 17, the chemical term is not included, since the temperature influence on the chemical potential difference in a material is negligible small [PEL05]. Only at the interface of two contact materials, the chemical term will be taken into account. Based on this theory, a device for Seebeck-coefficient determination has been developed [DEM14].

Already in the 1990s, Uehara has observed the influence of the thermoelectric current on the wear tendency in cutting processes [UEH92].

Based on the measurable Seebeck-coefficient, the influence of thermoelectricity on wear was studied in sheet metal forming. Tröber et al. have developed a tool set for the measurement of thermoelectric current or voltage blanking process. In this tool set, the tool and sheet metal are in a separated technical system and isolated through an isolating layer from the press [TRÖ16], see Figure 20.

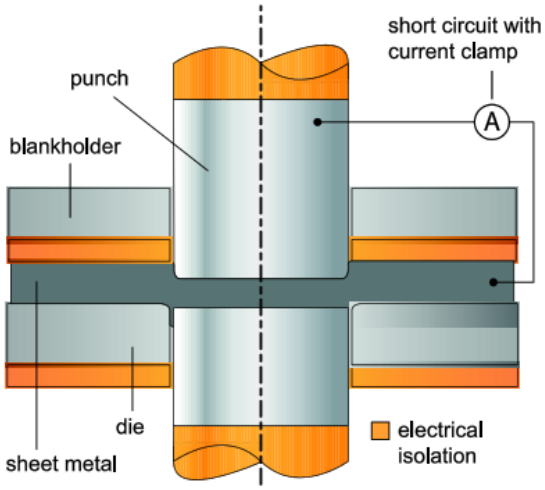

Figure 20 Tool set for thermoelectric measurement in blanking [TRÖ16]

The change of the current flow between two contacting conductor materials leads to the conversion of the chemical composition near the contact zone [HUA12]. As a result, the wear coefficient k of Archard's wear model is changed (see section 2.2.5).

The study of Tröber has confirmed that generated thermoelectric current correlates to the relative Seebeck coefficient between tool and sheet metal (see equation 18). And the higher the generated current, the higher is the tendency for adhesion on the tool surface [TRÖ17a].

In a recent study, it is confirmed that the tendency for adhesion can be weakened through different measures. Firstly, by deploying an external current in the opposing direction of the generated thermoelectric current, the adhesive wear can be reduced [TRÖ19, WEL20]. Moreover, through the modification of the chemical composition of the coating, the generated thermoelectric current

can be suppressed, which reduces the probability for adhesive wear occurrence [SCH21b].

The recent studies support a better understanding of thermoelectricity in metal forming. The temperature change is one of the reasons for the thermoelectricity generation. Therefore, it is an open question whether thermoelectric currents can be used for wear detection, as wear will result in higher contact temperature after surface roughening.

2.7 Tribometers for wear test

In the last part of this chapter, tribometers for wear tests are introduced. In sheet metal forming, increasing friction force always leads to premature tool wear when forming high-strength or ultra-high-strength steels (as discussed in section 2.1). For separate investigations of tribological conditions in a forming process, special tribometers were developed. They simulate the load conditions of actual processes through tool sets with simple geometries. The main aim of the experiments with the tribometers is the determination of the COF, which indicates friction behavior. An accurate COF determination is helpful for characterization of lubrication conditions for environmentally-benign lubricant [BAY08] or for understanding the influence of friction on the flow behavior of deformed materials [TRZ19]. In modern sheet metal forming, an accurate COF determination also optimizes the realistic forming simulation [SCH21a]. The tool geometries used for COF determination are summarized in Figure 21.

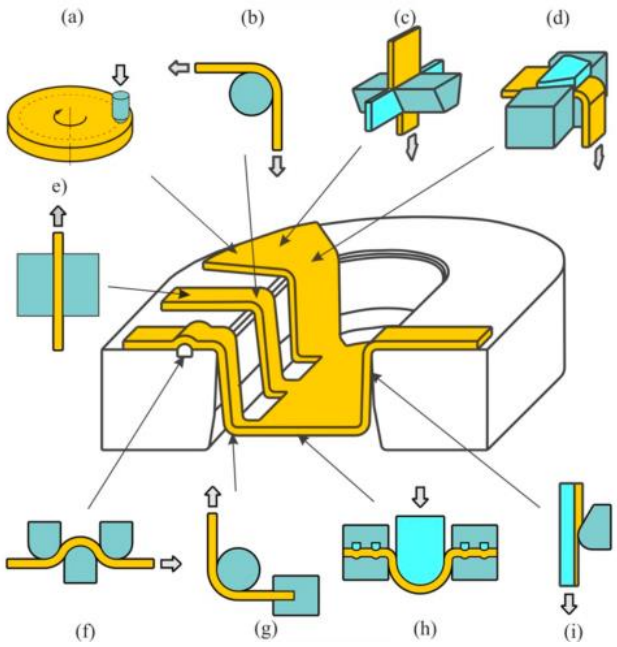

Figure 21 Tribometers representing the friction conditions in the specific areas of the work piece: (a) pin-on-disc, (b) bending under tension (BUT), (c) drawing with tangential compression,(d) bending with tangential compression, (e) flat die test (FD), (f) draw-bead test (DB), (g) strip-tension test, (h) hemispherical stretching, (i) strip reduction testing (SRT) [TRZ19]

From all the tribometers listed in Figure 21, several tribometers serve for the characterization of wear resistance of a tribological system in sheet metal forming. These will be discussed in the following section.

2.7.1 Categories of tribometers

According to the degree of abstraction, the tribometers are separated into six grades according to Czichos [CZI10] (see Figure 22). There is an inverse correlation between metrological accessibility and transferability to real forming processes [SCH21a]. In terms of sheet metal forming, DIN 50322 has classified that the categories 1 - 3 are actual and quasi-actual forming tests, which have high transferability. The experiments are deployed in actual, complicated environments, which are similar to actual processes. Categories 4-6 can be classified as model tests deployed in a laboratory environment. Tests from category 4 are forming tests with original or reduced size of tool sets, while the tribometers mentioned above can be classified to category 5 [CZI10]. In those tribometers, parameters such as contact stress, sliding velocity and temperature

can be adjusted to investigate the friction and wear behavior under specific tribological conditions. The tests of category 6 are standard general tribometers such as pin-on-disc or ball-on-disc tests according to DIN 51350, DIN 51834, ASTM D5707, ASTM D1894, ASTM G99 [SCH21a]. For sheet metal forming, this kind of tribometers has a low transferability to the actual process [GUO09]. Moreover, the sliding contact between the pin and disc is always located at the same position, which is different from sheet metal forming [EMM97].

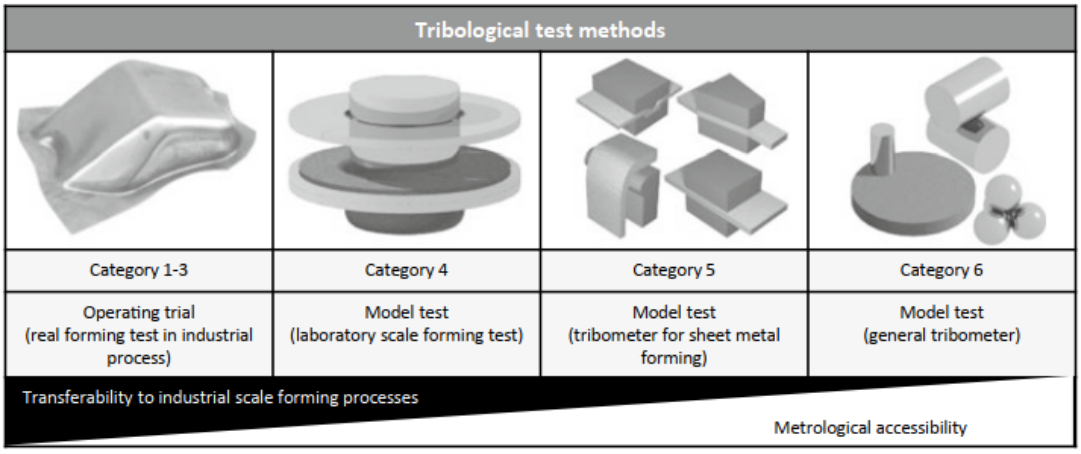

Figure 22 Categories of tribological test methods for sheet metal forming according to DIN 50322 [SCH21a]

2.7.2 The selection of tribometers for wear characterization

To investigate the wear behavior, the tribometers for wear tests are reviewed in Table 4. None of the tribometers are standardized except for the pin-on-disc test. The other tribometers listed are designed according to the tribological loads of actual processes.

Table 4 Overview of tribometers of wear characterization

Tribometer	Category	Forming process	Literature
Pin-on-disc	6	General	[DOH15, NOO16, OKO12, OKO11, TIL17, VEL17, YAO11]

BUT	4	Deep drawing	[BEH17a, BEH17b, GRO08, MOG17b, MOG17a, VAN02, YIL17]
SDT	5	Deep drawing	[ABR18, GRO11]
SRT	5	Ironing	[FIL22, MOG18, MOG19b, ÜST17, ÜST18]
Slider-on-flat-surface (SOFS)	5	General sheet metal forming	[GÅÅ08, GÅÅ09b, KAR12, VAN02, VAN01]
Actual test (such as cup test)	4	N/A	[OKO12, VOR17, VOS17]
FD	5	Flange of deep drawing	[DOM21]
DB	5	Stretching	[CHR16, CHR14, GRO13a, GRO19a]

As discussed in section 2.7.1, the pin-on-disc test is a basic tribometer that is not specifically designed for sheet metal forming. The advantage of it is the easy accessibility and low cost of testing. For other tribometers (in category 4 and 5) such as SDT, a metal coil should be used, and the amount of material consumption for a whole series of test can be over 1000 m [CHR16, GRO13a]. This high consumption of raw material and long test duration leads to a disadvantage with respect to the cost of testing.

For shortening the test duration, several measures have been developed. Firstly, the tools are designed to create higher loads and by that simulate more extreme tribological conditions. For example, the cylinder radius in SRT can be engineered smaller to obtain more sheet reduction [BAY08]. Secondly, Behrens et al. proposed an increased severity of conditions by adding wear particles to the contact zone between sheet and tools [BEH17a]. Thirdly, the normal force

of blank holders in SDT, SRT or DB can be adjusted to be higher and by that higher contact stress are set [GRO19a].

Hence, wear testing on tribometers is a useful method for characterizing the wear behavior and evaluating tool life span in sheet metal forming. Combined with the concept of WRD discussed in section 2.3.3, the life span under different load levels can be estimated. However, since the duration of an e.g. strip drawing test is very lengthy [GRO19a], it is necessary to discuss possibilities to obtain a satisfactory estimate by performing as few tests as possible. So far, data have been obtained at high contact stresses with comparatively low total sliding length. Based on these data, it is difficult to predict tool life under the loads commonly found in industrial forming processes. In order to extend the predictability of wear, an extrapolation of the derived data is required. Therefore, a wear resistance curve (WRC) described by a mathematical model is proposed and discussed in chapter 6. With the help of the WRC, a database for analysing the tool life spans can be obtained.

2.8 Summary of the chapter

In this chapter, the state-of-the-art of wear control in sheet metal forming was described. Until recently, a reliable method of controlling wear in sheet metal forming is still a challenge for several reasons:

1. A lack of a wear detection approach with high accuracy, sensitivity and real-time capability (discussed in section 2.5.4)

2. The widely used wear detection method such as roughness measurement have a poor measuring frequency, which is disadvantageous for determining the wear development and hampers the understanding of wear

3. Inadequate research on the influence of tool hardness and roughness (discussed in section 2.4)

4. The recent approach for wear prediction through wear models is still based on empirical values such as the wear coefficient k (discussed in section 2.3.2). The indirect wear prediction through load-dependent WRD has already been

initiated, but a database is needed to look up the life span under all load levels to enhance the application of this approach.

Therefore, an inline method for accurately detecting wear, a useful method for life span estimation of forming tools and a deeper understanding of the influence factors of wear behavior are the three main factors for improved wear control in sheet metal forming. The way for a reliable and effective wear control is illustrated as a triangle shown in Figure 23.

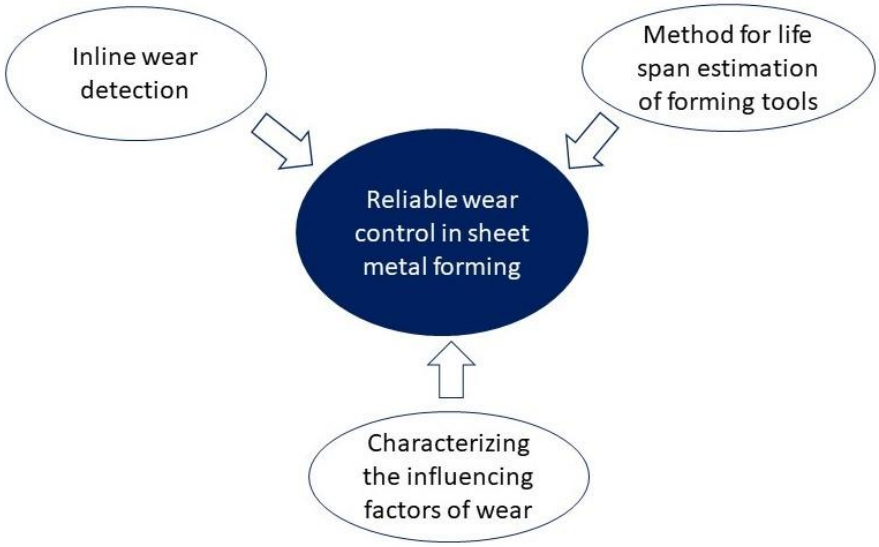

Figure 23 Necessary steps towards a reliable control in sheet metal forming

3 Aim and approach of the dissertation

3.1 Aim of the dissertation

According to the state-of-art discussed in Chapter 2, a number of challenges in wear detection and prediction are the main barrier for an effective wear control in sheet metal forming.

The reliable and non-destructive detection of tool wear in due time is a prerequisite to achieve the optimized wear control. So far, the detection of wear in forming technologies is based on offline visual assessment and optical roughness measurement of the tool surface. The time delay between the occurrence of unacceptable severe wear and the offline surface analyses increases the risk of scrap production. Consequently, alternative inline or online wear data acquisition with higher resolution in time is needed for real-time wear detection. The development of a concept for inline wear detection based on the approach of thermoelectric measurement (see Section 2.6) is the first aim of this dissertation.

Due to the system characteristic of a tribological system, wear prediction is still a challenge, since several factors such as contact pressure, material hardness and surface characteristics have an impact on the wear development according to different wear prediction models. For actual production, the estimation of life spans of forming tools is meaningful for an optimized planning of production and maintenance intervals for forming tools. Therefore, a method for life span estimation of an actual forming process based on the indirect wear prediction method, the wear resistance analysis (see Section 2.3.3), is the second aim of the dissertation.

After the derivation of the method for life span estimation, the investigation of different influence factors on the tool life span also fosters a comprehensive understanding of wear behavior, which is also beneficial for a reliable wear control. The characterizing of diverse influence factors such as the material hardness and the surface roughness on the tool life span is the third aim of the dissertation.

3.2 Approach of the dissertation

In order to cope with the challenges mentioned in 3.1, the approaches for wear detection, prediction and investigation of wear influencing factors are summarized in the mindmap of Figure 24.

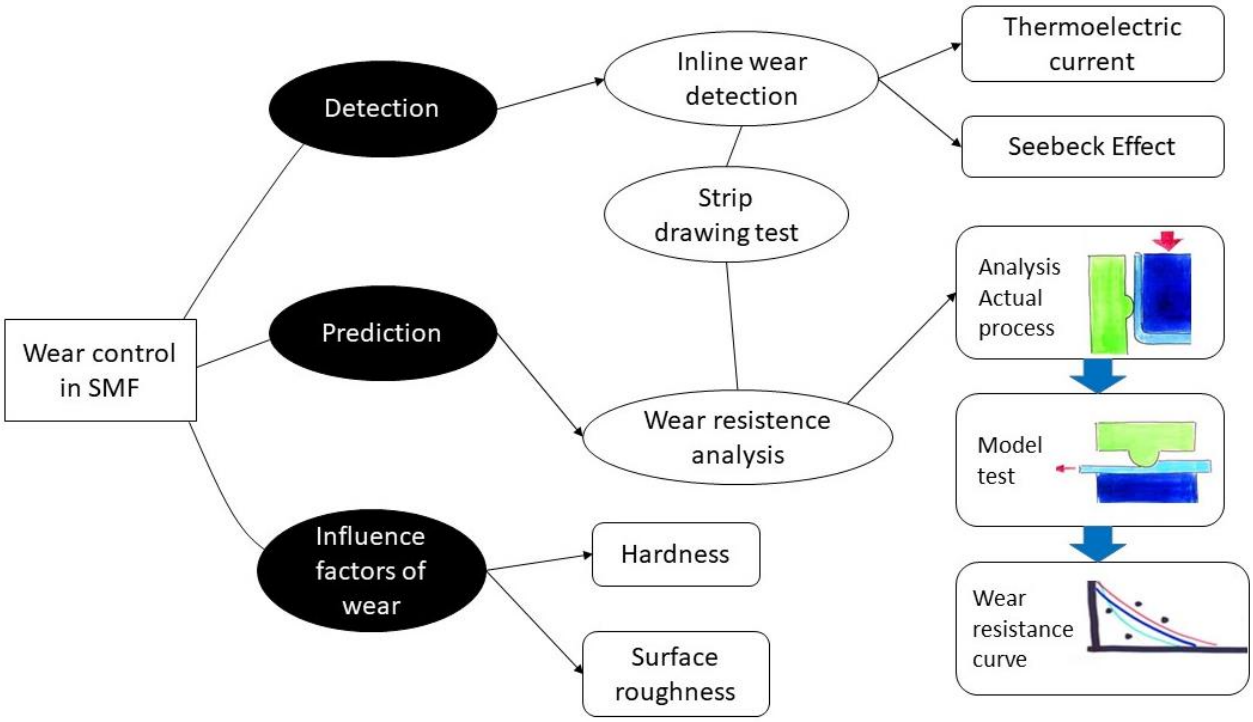

Figure 24 Mindmap of the dissertation

Firstly, a method for inline, non-destructive wear detection method is to be proposed through the measurement of thermoelectricity based on the Seebeck effect. The strip drawing test at the PtU with modified toolsets is used for this investigation. Based on the proposed method for inline wear detection, the life span of forming tools can be defined more accurately, which founds the basis for a reliable wear resistance analysis.

For wear prediction of an actual forming process, the critical factors on wear such as contact stress are analyzed by numerical simulations. The critical loci of wear are defined. Based on the analysis, tool sets for strip drawing tests are designed and manufactured. The wear tests are deployed under different load levels and the wear data are plotted into the wear resistance diagram (WRD). However, WRD is composed of scatter points with wear data. For a general

application, the wear resistance curve (WRC) is derived by a mathematical extrapolation based on the WRD.

Finally, the influence factors of wear such as hardness and surface roughness are characterized for a better understanding of wear in sheet metal forming.

4 Inline wear detection in sheet metal forming

As summarized in chapter 2, a reliable, sensitive and real-time wear detection has several advantages for optimizing the resource efficiency in metal forming. From an industrial point of view, the real-time detection of severe wear helps the detection of tool wear in due time and avoids scrap production. From the academic view, the determination of wear development in forming tools with high measurement frequency promotes a better understanding of the wear behavior in sheet metal forming. In this chapter, an inline wear detection method based on thermoelectric measurements is proposed. The contents of this chapter are part of the publications (co-)authored by the author ([GRO19b] and [WU21a]).

4.1 Introduction to the test stand

For a targeted investigation of friction and wear in a forming process, a modelling test method for wear detection is developed. The strip drawing test of the Institute for Production Engineering and Forming Machines (PtU) of the Technical University of Darmstadt is a model test for wear and friction testing. It simulates the contact condition of a real process with similar loads. Figure 25 shows the principle of the strip drawing test. It consists of two reels for coil unwinding and rewinding, a lubricating chamber, a sheet transfer system, the press and the gripper. For the press of the test stand, several testing tools with simplified geometries are designed for wear tests in order to simulate the real sheet metal forming process [NET95]. The cylindrical-flat die simulates the load of drawing rings of a deep drawing process, while the load between flat dies with plain geometry corresponds to the load at the flange area of deep drawing. The draw bead geometry models the multiple bending, which is widely used in car body drawing processes. Additionally, process parameters such as contact pressure can be independently controlled through adjusting the normal force for an accurate evaluation of their influence. In the test stand, the required normal

force is supplied by four hydraulic cylinders. Therefore, it can be classified as “Category 5” of tribometers according to Figure 22. Groche et al. also investigated the transferability of the results from strip drawing tests to real production processes. The results show a good agreement between the wear development of tools in laboratory wear model test and the industrial processes [GRO19a].

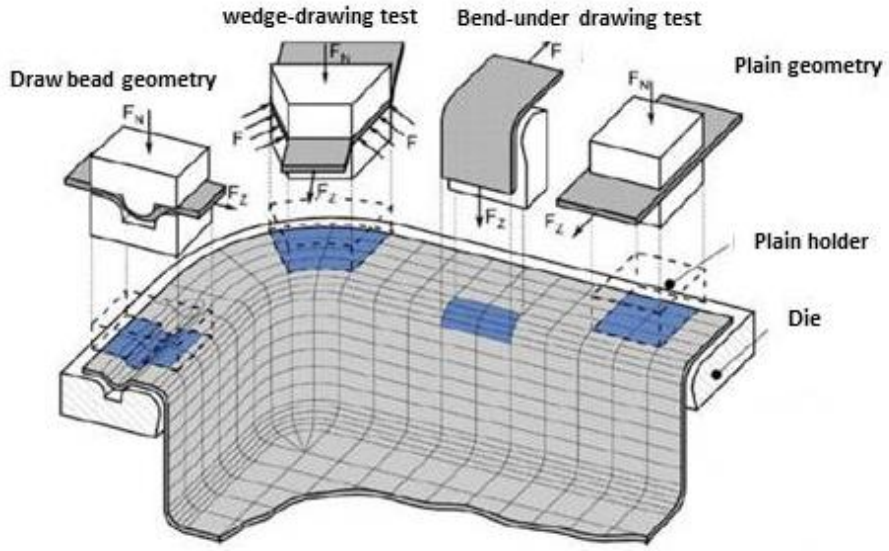

Figure 25 The sliding zones of a deep drawing process and simplified tools for strip drawing tests [NET95]

Based on its good transferability, it is reasonable to use this test stand for developing the method for wear detection and prediction. The characteristic parameters of the strip drawing test stand are shown in Table 5. The kinematics of the strip motion is applied by a gripper, which is attached to a cam and draws the strip through the closed tool discontinuously. The sheet metal is drawn with a speed of 100 mm/s with 100 mm stroke length. After one stroke, the gripper is opened, returns to the initial gripping position and draws the next stroke. The return motion lasts approximately 0.5 s. Meanwhile, the sheet metal remains in a static state [GRO13a]. With this kinematics, a continuous strip drawing test can be deployed automatically for wear behavior characterization. The test setup for inline wear detection is carried out on the strip drawing test stand.

Table 5 Parameters of the strip drawing test of PtU

Maximal normal force	150 kN
Recommended normal force for continuous tests	< 50 kN
Maximal drawing speed	100 mm/s
Sliding length pro stroke	100 mm
Compatible sheet metal width	20 -50 mm
Compatible sheet thickness	0.5 – 2 mm

4.2 Test setup and measurement principle

For the integration of the inline wear detection concept, a thermoelectric measurement is developed for the strip drawing test setup with cylinder-flat-geometry. The radius of the cylinder is 238 mm. The principle of the test setup is shown in Figure 26.

The sheet is loaded with a force F_N via blank holder and die tools. Two isolation layers are installed to avoid the electric contact between the tool holders and the tools. The material of the isolation layer is the glimmer plate GL-M of Brandenburger Isoliertechnik. The measurement module NI 9219 of National Instrument (NI) is applied for current measurements in this study. During the sliding of the sheet metal, frictional heat develops in the contact area between tools and sheet metal. An electric potential emerges between the hot and cold ends of a solid, which generates a thermoelectric current flow within the solid (the Seebeck Effect, see section 2.6.1).

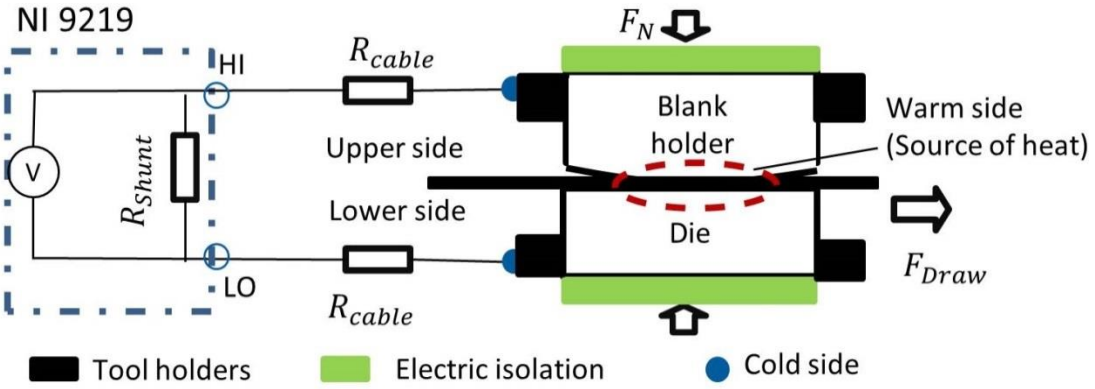

Figure 26 Test setup and principle of thermoelectric current in strip drawing tests with cylinder-flat geometry (Source: [GRO19b])

In the test setup, the contact area between tools and sheet can be regarded as the warm sides or the heat sources due to sliding between tool and sheet metal, while the junction ´HI´ and ´LO´ of the measuring module represent the cold sides. Figure 27 shows the electric schematic of the measurement principle.

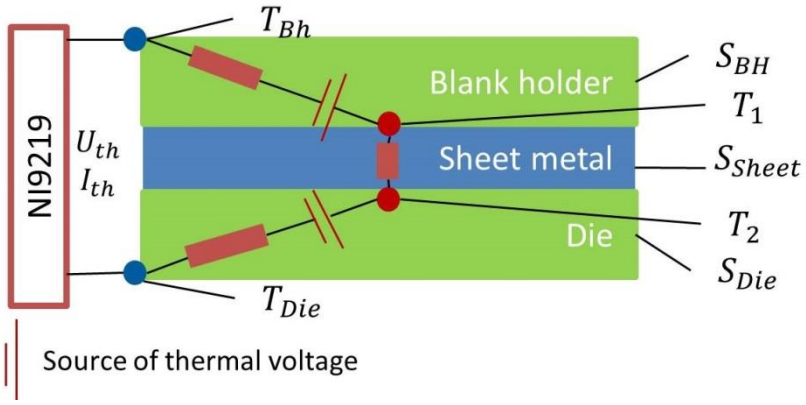

Figure 27 Electrical schematic of the measurement principle (Source: [WU21a])

The generated thermoelectric voltage can be described by the following equation:

$$\mathrm{U_{th}} = \mathrm{S_{BH}} \cdot (\mathrm{T_1} - \mathrm{T_{BH}}) - \mathrm{S_{Die}} \cdot (\mathrm{T_2} - \mathrm{T_{Die}}) + \mathrm{S_{Sheet}} \cdot (\mathrm{T_1} - \mathrm{T_2}) \quad (20)$$

where $\mathrm{U_{th}}$ stands for the thermoelectric voltage, T the temperature and S_i Seebeck coefficients of components i. According to the equation, the generated thermoelectric voltage is dependent on the Seebeck coefficient, the temperature difference between the contact (warm side) and the tool holder (cold side: $\mathrm{T_{BH}}$ and $\mathrm{T_{Die}}$). For simplification, equation 20 is transformed into equations as

followed, when the cold side temperature T_{BH} and T_{Die} is assumed to be identical with the room temperature T_{RT}:

$$U_{th} = (S_{BH} + S_{Sheet}) \cdot T_1 - (S_{Die} + S_{Sheet}) \cdot T_2 + (S_{Die} - S_{BH}) T_{RT} \quad (21)$$

$$U_{th} = S_{BH+S} \cdot T_1 - S_{Die+S} \cdot T_2 + r \quad (22)$$

It is obvious that the generated thermoelectric voltage is dependent on the sum of the Seebeck coefficient of tools S_{BH} and sheet metal S_{Sheet} (S_{BH+S}) as well as the sum of S_{Die} and S_{Sheet} (S_{Die+S}). Therefore, equation 21 can be simplified as equation 22, where S_{BH+S} and S_{Die+S} are the combined Seebeck coefficients of the tool and sheet metal. The residual $r = (S_{Die} - S_{BH}) \cdot T_{RT}$ is determined by the difference of both Seebeck coefficients of both tools and the room temperature. To eliminate the residual, the contact temperature T_1 and T_2 can be described as the sum of the room temperature T_{RT} and temperature rise ΔT_1 as well as the sum of T_{RT} and ΔT_2. As a result, equation 22 is simplified as:

$$U_{th} = S_{BH+S} \cdot \Delta T_1 - S_{Die+S} \cdot \Delta T_2 \quad (23)$$

The generated thermoelectric voltage is influenced by the temperature rise at the two contact loci ΔT_1 and ΔT_2 as well as the combined Seebeck coefficients. Since the signs of the two terms of equation 23 have a different direction, it can be assumed that a positive thermoelectric voltage is caused by the abrupt temperature increase due to severe wear occurrence on the blank holder, while a negative thermoelectric voltage derives from the wear-induced temperature rise on the die.

After connecting the cables to the measurement module NI 9219, an electric circuit is formed and the thermoelectric current is generated, which is described by the following equation:

$$I_{th} = U_{th} / (R_{Sheet} + R_{BH} + R_{Die} + R_{Shunt}) \quad (24)$$

where I_{th} stands for the thermoelectric current and R_{Sheet}, R_{BH}, R_{Die} and R_{Shunt} stand for the electrical resistance of the sheet, blank holder, die and shunt inside the measurement module NI 9219.

According to equations 23 and 24, it is assumed that, if wear occurs on a tool surface, the surface roughness of this tool and the corresponding sheet metal increases. It is assumed that more heat (ΔT_1 or ΔT_2) is generated due to the

increased friction resistance caused by the surface roughening. This results in increased thermoelectric currents. Evidently, if no heat or the same amount of frictional heat is generated in both contact areas in the contact zones no current I_{th} could be detected.

Depending on the locus of more pronounced roughening, either the first or the second term of equation 23 dominates. Therefore, the amount and the sign of the measured value I_{th} indicate the locus of wear and is an indicator for the degree of wear.

4.3 Correlation analysis for wear detection

In order to evaluate the measurement principle, an experimental wear test is employed. For examining the feasibility, a first test serves as proof for the correlation between tool wear and evolution of the thermoelectric current. The test matrix is shown in Table 6. Tools are made out of the cold working steel X153CrMoV12 (DIN: 1.2379), while the sheet metal consists of the high strength, low alloy steel H630LA, manufactured by C.D. Waelzholz. In former research, this type of sheet metal material has shown a high tendency to adhesive wear [GRO13b].

Table 6 Test matrix of correlation analysis

Tool material	X153CrMoV12 (1.2379)
Sheet material	Low alloy steel H630LA (Manufacturer: C.D. Waelzholz)
Lubricant	Multidraw PL61 (Manufacturer: Zeller+Gmelin)
Lubricant amount	2 g/m^2
Normal force	10 kN
Sliding velocity	100 mm/s
Sheet metal width	50 mm
Sheet metal thickness	1.5 mm
Tool width	40 mm

The strip drawing test is interrupted after every five strokes (i.e. 500 mm sliding length) and the 3d surface topography of the tools is scanned with the confocal microscope µSurf 2015. The obtained surface topographies are shown in Figure 28. A first material pickup at the blank holder could already be observed in the first measurement after the 5th stroke. With increasing sliding length, the ten-point height S_z (DIN EN ISO 25178) which is used to describe the worn surface according to [REI12], increases gradually until the 25th stroke. After the 30th stroke a drastically increased amount of adhesive wear becomes visible. It can be assumed that a massive galling is generated next to the pickup, which was built up between the 25th and 30th stroke, is responsible for this increase. The maximum height of asperities reaches up to 50 µm.

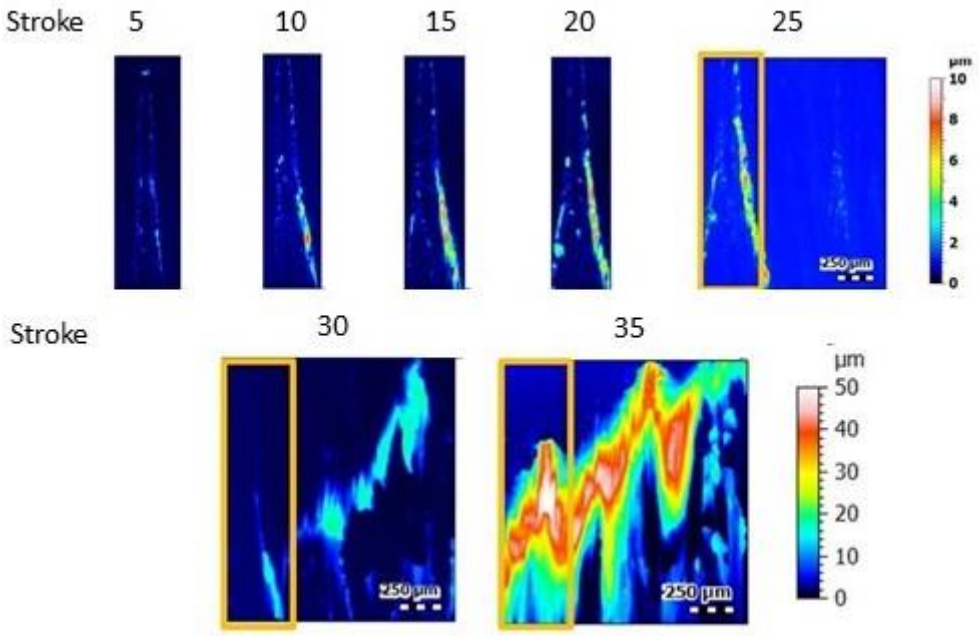

Figure 28 Surface topographies after every five strokes (Source: [GRO19b])

At the same time, the thermoelectric current is measured continuously. After the wear test, the 2d roughness profiles of the sheet are measured perpendicular to the sliding direction through tactile roughness tester Hommel Waveline T8000. The measuring length on the sheet metal is 40 mm, which is located symmetrically around the center of each stroke. The obtained 2d and 3d roughness as well as the thermoelectric current are shown in Figure 29.

It can be found from the plot that the S_z-value has an abrupt increase after the 25th stroke (see Figure 29b), which corresponds to the surface topographies. From the observed offline tool surface analysis, it can be figured out that the start of severe wear occurs between the 25th and the 30th stroke. According to Bayer, the moment of sudden jump of the wear rate can be defined as the beginning of severe wear [BAY04]. In this approach, the wear rate on the sheet metal is described through the characteristic value $|R_z(n+1)\text{-}R_z(n)|$, which depicts the absolute roughness change between stroke n and the next stroke (n+1).

As depicted in Figure 29c, the $|R_z(n+1)\text{-}R_z(n)|$ for the first 25 strokes fluctuates in a small interval and the value remains on a low level: However, the value increases abruptly from the 26th stroke onwards. This observation corresponds to the sudden increase of the measured sheet roughness R_z on the upper side of the sheet metal strip. Both values indicate the start of severe wear at the 26th stroke. This observation is also in good accordance with the surface roughness S_z of tools. From the sheet metal roughness measurements, it can be expected that severe wear on the blank holder tool occurs during the 26th stroke firstly.

The development of the thermoelectric current increases during each sliding movement of the sheet metal (see Figure 29a). The positive sign indicates that higher temperatures occur in the contact zone between blank holder and sheet compared to the contact zone between die and sheet. This can be reasoned by a higher contact stress resulting from the cylindrical tool surface. Between two strokes, the sheet metal does not experience any relative movement or sliding. Therefore, the current decreases to zero due to temperature equalization. The generated current rises with increasing sliding length up to the 25th stroke gradually. From the 26th stroke onwards, the maximum current values increase drastically with each stroke. This transition from stationary to suddenly increasing thermoelectric current is in agreement with the transition from stationary to severe wear on the blank holder surface as well as the sheet surface. This distinct correlation indicates that the thermoelectric current can serve as an indicator for severe wear occurrence. The gradient of the S_z-value and the thermoelectric peak value have a proportional relation. As a result, the

relation between the deviating wear coefficient k' and the peak value of the thermoelectric current can be approximated by:

$$k' = a \cdot P_{current} \quad (25)$$

with a representing an empirical factor depending on the tribological system and $P_{current}$ the thermoelectric peak current. Moreover, it can be stated that the end of the moderate increase of the thermoelectric current indicates the end of the stationary phase of wear development. In this case, the boundary value is about 9.8 µA (Figure 29b), which corresponds to $P_{current}$ at 25th stroke. It is assumed that severe wear occurs after reaching the boundary value.

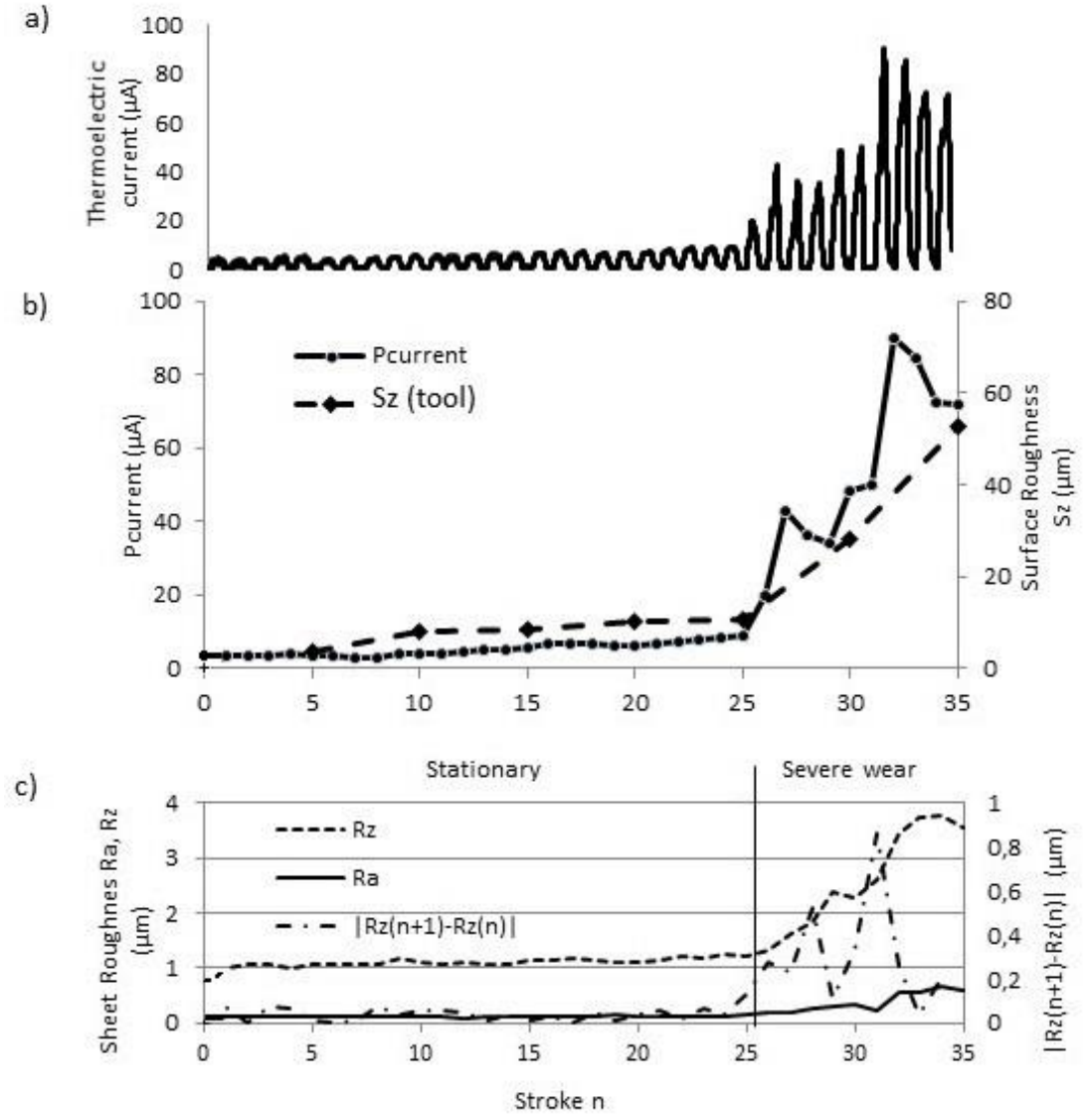

Figure 29 Correlation between thermoelectric current (a), conventional geometrical methods of wear detection on tools (b) and surface roughness on the sheets (c) (Source: [GRO19b])

4.4 Analysis of the reproducibility of thermoelectric measurements

After the correlation analysis of the measurement principle, the reproducibility is examined. Five strip drawing tests (Test 1 - 5) with identical blank holder loads, materials and process parameters are conducted. Test 1 corresponds to the results already described in section 4.3. To examine the influence of the thermoelectric current on the wear development, the cables for the current

measurement are disconnected in Test 5 and only the roughness values are recorded. The peak values of the thermoelectric current of each stroke as well as the sheet metal surface roughness values R_z are shown in Figure 30.

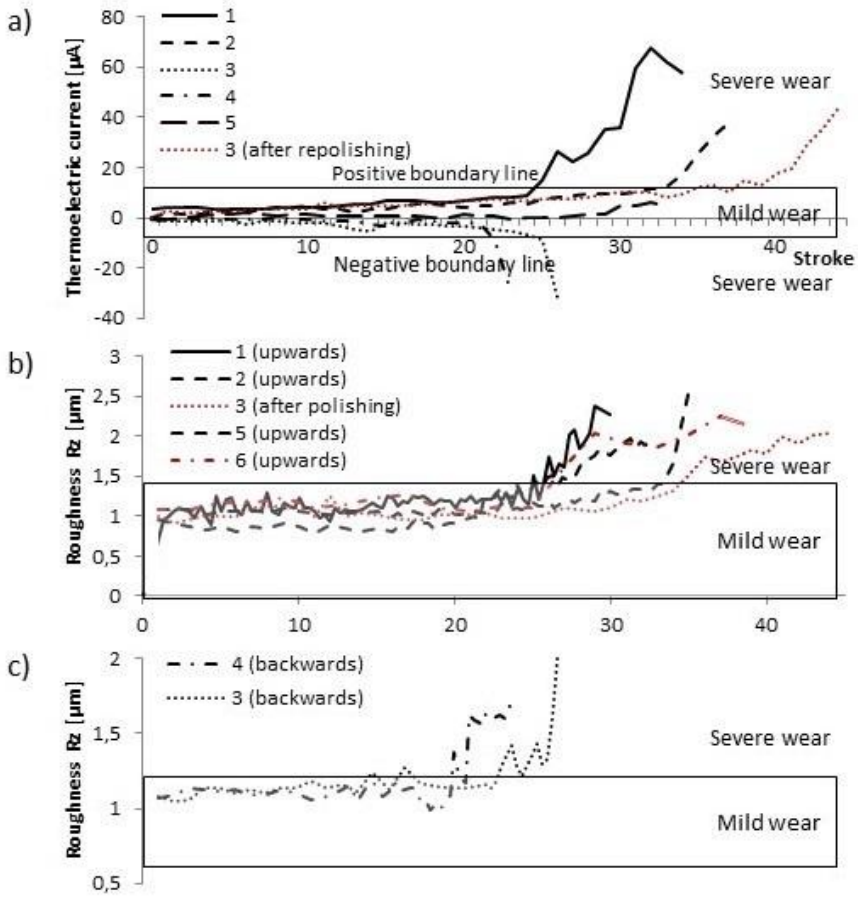

Figure 30 (a) Evolution of the thermoelectric peak current; (b) the sheet metal roughness R_z of the sheet where severe wear occurs on the upper side; (c) the sheet metal roughness R_z of the sheet where severe wear occurs on the lower side (Source: [GRO19b])

The transition from stationary to severe wear takes place between the 20th and 35th strokes for all investigated tribological systems. The stroke numbers for the transitions from stationary to severe wear are determined with optical and thermoelectric measurements. The transitions are marked in Figure 30b and c.

Regarding Test 1 - 4, as can be read from the diagram in Figure 30a, the values of the thermoelectric current in tests 1 and 2 are positive, while they are negative in tests 3 and 4. This implies that the wear on the blank holder (upper tool) dominates in tests 1 and 2, whereas the wear on the die (lower tool) dominates

in tests 3 and 4. These observations are in full accordance with the measurement of the sheet surface roughness. The transition from stationary to severe wear in tests 1 and 2 takes place on the upper side of the sheet surface. In tests 3 and 4, the severe wear can only be observed on the lower side of the sheet metal. Similar to the results of test 1 in Figure 29b, boundary values which indicate the end of stationary state of test 2 - 4, can also be identified in Figure 30b. The absolute boundary values range from 9.8 µA (Test 1) to 10.2 µA (Test 2). Therefore, it is concluded that the validity and reproducibility of the proposed test method is proven.

Test 5 of Figure 30 demonstrates the influence of the thermoelectric measurement on wear resistance. The roughness values of the sheet surface in test 5 increase sharply in the 26th stroke. This corresponds to the ranges of life spans determined in tests 1 to 4. Hence, this result shows no significant influence of the thermoelectric current measurement on the tool life span. This is contrary to the study of Tröber et al. [TRÖ17b]. The reason is that the generated thermoelectric current in this study is in the order of µA, compared to mA in the study of Tröber et al..

Test 6 is to examine the necessity to use the isolation layer in the tool set (see Figure 26). In this test, the isolation layer is not installed, but the cables for the thermoelectric measurement are still connected. The result of surface roughness shows a transition from stationary to severe wear at the 22nd stroke. However, the thermoelectric current shows no corresponding changes, but fluctuates around 0 µA. This confirms the necessity for the isolation layer to avoid the current flow to the tool holder.

The reasons for wear occurrence at two different loci can be interpreted by Vickers hardness measurements of the tools according to the standard ISO 6507 through a hardness tester DuraScan 20 (see Figure 31). In tests 1, 2, 5 and 6, the hardness of the blank holder is higher than the die. On the contrary, the die hardness is higher than the blank holder in tests 3 and 4. Therefore, the wear behavior of the tested tribological systems with respect to the locus of maximum wear can be divided into two groups based on Archard’s model, which determines the sign of the thermoelectric current.

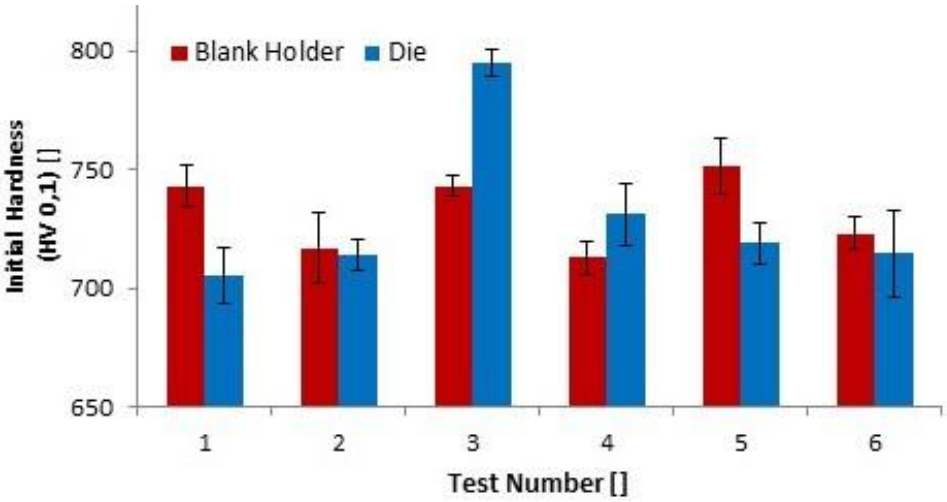

Figure 31 Initial hardness of the tools (Source: [GRO19b])

In summary, the method of the thermoelectric current measurement can serve as suitable basis for detecting wear on forming tools. A threshold value for the end of the moderate increase could be identified through evaluating all determined curves. For the tested tribological system, the value ±10.2 µA can be regarded as the critical value between stationary and severe wear (Figure 30a). If the thermoelectric current exceeds one of these limits, severe damage of the tools must be expected soon. This small amount of the current has no negative influence on the tool life span. For a reliable measurement, the isolation plate is necessary to be integrated in the tool set.

4.5 Influence of Seebeck coefficient on thermoelectric measurement in wear detection

After understanding the behavior of thermoelectric current throughout the whole wear development, several wear tests with different materials are used to obtain a deeper understanding of this wear detection method. Tröber et al. confirmed that the influence of different Seebeck coefficients has a pronounced influence on the generated thermoelectric current [TRÖ17b]. According to equation 23, the generated thermoelectric current is possibly around zero, when the combined Seebeck coefficient of tool and sheet are close to zero. Therefore, it is necessary to examine the influence of the Seebeck coefficient on the effectiveness of wear detection. For this study, three further materials, 99.9%

aluminum EN AW-1050A, the aluminum alloy EN AW 5083, the stainless steel X5CrNi18-10, together with the low alloy steel H630LA as reference, are used for the study.

4.5.1 Determination of Seebeck coefficients

The first step of the study is to determine the Seebeck coefficient of the investigated materials. The method corresponds to the approach of Demmel [DEM14]. A special equipment is designed and assembled for this approach. The introduction to the measuring equipment and measurement principle is shown in Appendix 1.

Firstly, the Seebeck coefficients of the four sheet materials are measured. Every material is measured with three repetitions. The result is shown in Figure 32. It can be stated that the low-alloyed steel sheet H630LA has the highest Seebeck coefficient, which is about twice that of stainless steel X5CrNi18-10 (DIN 1.4301) and the aluminum alloy AW 5083. The aluminum alloy AW 5083 and the stainless steel X5CrNi18-10 have a Seebeck coefficient similar to the result of Tröber et al. [TRÖ17a], where the difference in Seebeck coefficient between the aluminum alloy EN AW-1050A and the stainless steel X5CrNi18-10 is close to zero.

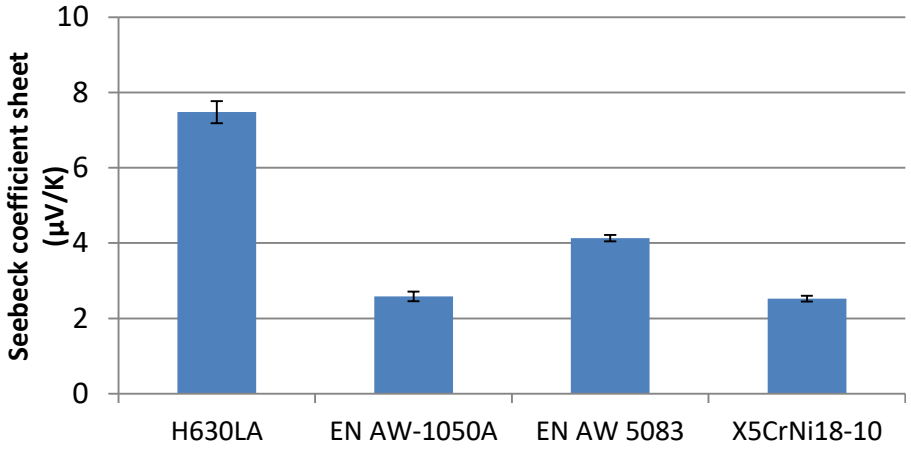

Figure 32 Measured Seebeck coefficient of different sheet materials (at room temperature (23 °C)) (Source: [WU21a])

Besides the sheet metal, the Seebeck coefficients of the tools also play an important role in the thermoelectric generation according to equation 23. Due to the different design of the wire connection at the tool holders, the Seebeck

coefficient of blank holder and die made of hardened cold working steel X153CrMoV12 (DIN: 1.2379) is determined separately. It can be seen from Figure 33a that the blank holder is mounted on the tool holder, which is made of the unhardened cold-working steel X153CrMoV12. On the side of the tool holder, a brass bracket is mounted for the cable connection. In the tool holder of Figure 33b, the bracket connects the die directly. For the thermoelectric measurement, the cable is fixed between the contact position of the tool (heating point: red) and the bracket (reference point: blue). At each position, two K-type thermocouples are connected at the heating and the reference points for temperature monitoring. With this measurement setup, the Seebeck coefficient of both sides of the tools can be calculated and the result after three repetitions is illustrated in Figure 33c. It can be stated that the Seebeck coefficients of the blank holder and die (Material: X153CrMoV12) are in the same level around 20 µV/K, which also corresponds to the results of Tröber [TRÖ17a]. The slight differences can be ascribed to the different connection methods of the brackets.

Comparing the Seebeck coefficient of sheet metals (Figure 32), the Seebeck coefficient of the tool material dominates. Based on equation 23, the combined Seebeck coefficient determines the generated current. The combined Seebeck coefficients $S_{\mathrm{BH+S}}$ and $S_{\mathrm{Die+S}}$ of four materials are shown in Figure 34.

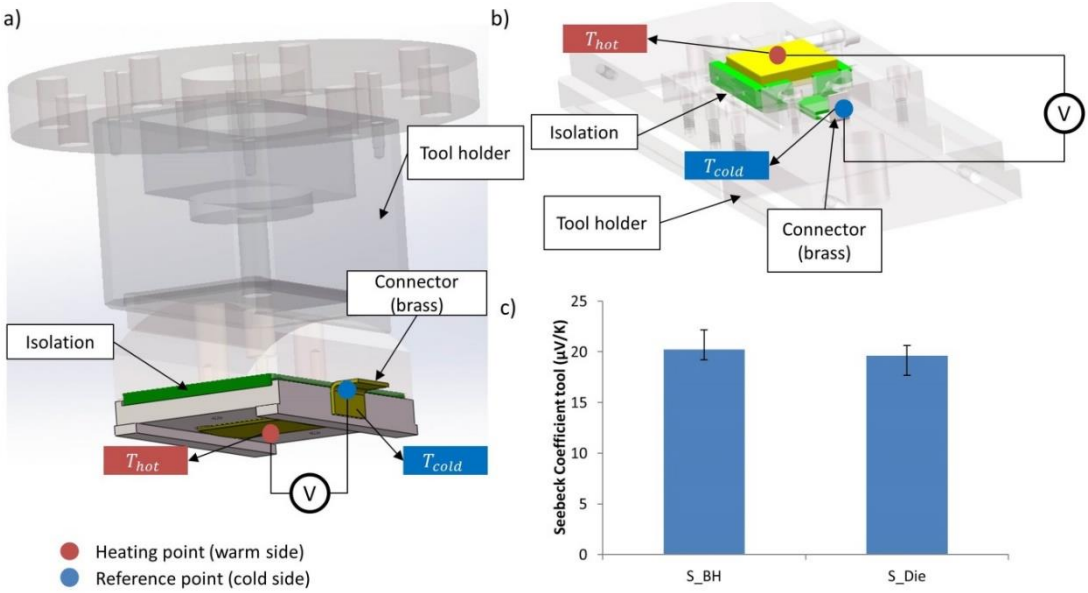

Figure 33 Measurement procedure of the Seebeck coefficient of the a) Blank holder; b) Die; c) the measured Seebeck coefficient of the blank holder S_{BH} and die S_{Die} (Source: [WU21a])

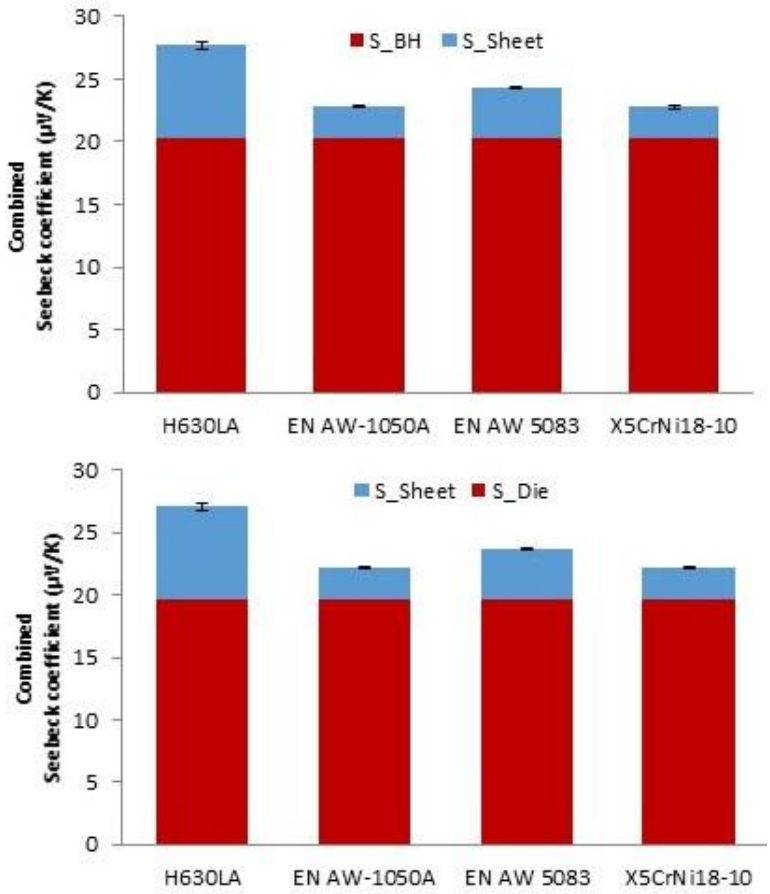

Figure 34 The combined Seebeck coefficients of tools and sheet metal (at room temperature of 23 ℃) a) blank holder; b) die (Source: [WU21a])

Similar to the results shown in Figure 32, H630LA shows the highest combined Seebeck coefficient, about a factor 1.2 higher than AW 5083 and X5CrNi18-10.

4.5.2 Wear test: influence of the Seebeck coefficient

After the determination of the combined Seebeck coefficient, wear test for characterizing the influence of the Seebeck coefficient on the wear detection are carried out. According to equation 23, the sign of the measured thermoelectric current is dependent on the loci of the wear. If the severe wear occurs in the blank holder, the sign is positive and vice versa. In order to obtain the value of the thermoelectric current on both the positive and negative sides in a targeted manner, the lubrication conditions are different for each wear test. Six tests are used for each material and the aim is to generate the severe wear three times on the blank holder (Test 1 - 3) and three times on the die (Test 4 - 6). In Table

7, the lubricating condition of each wear test is summarized. The strategy is: the lubricating amount on the upward and downward side of sheet is manipulated. For example, the amount on the downward side of test 1 - 3 is higher, which leads to a tendency to wear occurrence firstly on the upward side. The lubricating amount on the tool follows the same strategy.

Table 7 Summary of the lubricating condition in wear tests

Test material	Lubrication condition on sheet metal	Lubrication condition on tool
H630LA X5CrNi18-10	Test 1 - 3: upper side – 0.8 - 1 g/m^2 lower side – 1.8 - 2 g/m^2 Test 4 - 6: upper side: 1.8 - 2 g/m^2 lower side: 0.8 - 1 g/m^2	Test 1 - 3: upper side – 0.8 - 1 g/m^2 lower side – 1.8 - 2 g/m^2 Test 4 - 6: upper side: 1.8 - 2 g/m^2 lower side: 0.8 - 1 g/m^2
EN AW-1050A EN AW 5083	Test 1 - 3: upper side - no lubricant lower side – 0.5 - 0.8 g/m^2 Test 4 - 6: lower side: no lubricant upper side: 0.5 - 0.8 g/m^2	Test 1 - 3: blank holder: approximately 3 g/m^2 Die: no lubricant Test 4 - 6: blank holder: no lubricant Die: approximately 3 g/m^2

The wear test is deployed until severe wear occurs on one of the test tools. The boundary value of the thermoelectric current and the peak value of the thermoelectric current of the last stroke are documented. An example of the wear test with H630LA and its evaluated values is illustrated in Figure 35.

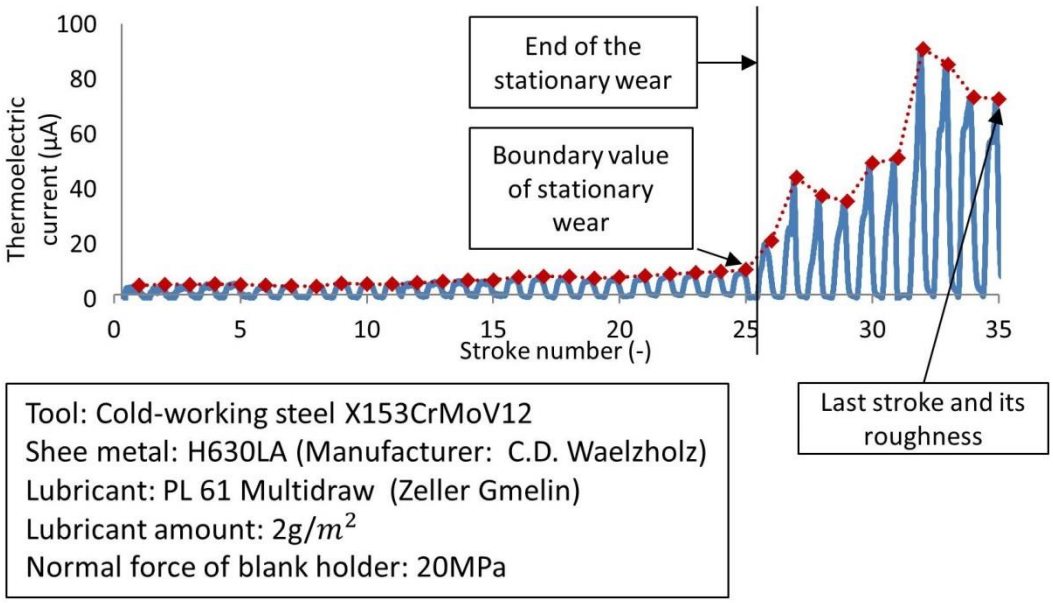

Figure 35 An example of thermoelectric current evaluation (Source: [WU21a])

Figure 36 shows the boundary value of stationary wear for each wear test for three materials. Since the wear development of EN AW-1050A shows an abrupt increase after the occurrence of severe wear and no steady-state phase can be detected, no obvious boundary value can be found. Compared to the measured Seebeck coefficient shown in Figure 34, the boundary value of the current is approximately proportional to the development of the combined Seebeck coefficient.

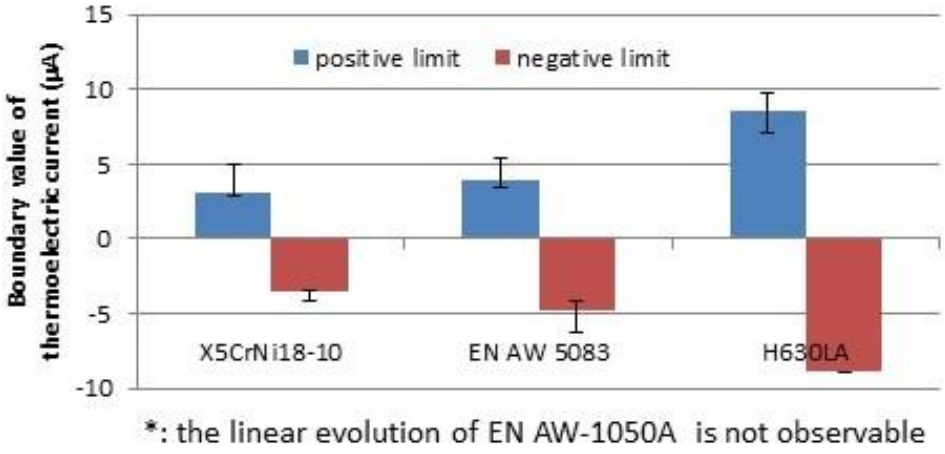

Figure 36 Boundary value of thermoelectric current for three test materials

From the results, the following conclusions can be drawn:

The tribological system with higher combined Seebeck coefficient (S_{BH+S} and S_{Die+S}) has a higher boundary value of the thermoelectric current. The temperature increase due to the surface roughening after wear is much easier detectable in tribological systems with higher combined Seebeck coefficient. Hence, the wear detection for tribological system with higher combined Seebeck coefficient has a higher sensibility. On the contrary, the wear is hard to detect when the combined Seebeck coefficient is close to zero. Therefore, for an optimal detection of wear with high sensibility, a higher combined Seebeck coefficient of tool and sheet metal is desired.

4.6 Behavior of thermoelectric current after severe wear occurrence

In section 4.4, the behavior of the thermoelectric current and its correlation with the surface roughness in the running-in, steady-state and the beginning of severe wear phase is discussed. In this section, the behavior of the thermoelectric current after severe wear occurrence will be discussed.

4.6.1 Behavior of thermoelectric current after wear occurrence

Another wear test deployed at room temperature with a low alloy steel in a strip drawing test is analyzed. The cold-working steel X153CrMoV12 and the low alloy steel H630LA are used in this test. The sheet metals are lubricated with the lubricant PL61 (Supplier: Zeller+Gmelin) with an amount of 2 g/m^2. The normal force of the blank holder is set to 20 kN for an accelerated wear development. Similar to the last tests, the sheet metal is clamped with a gripper, the sliding speed is 100 mm/s and the length of each stroke is 100 mm. After the wear occurred on both sides of the tools, the wear test was interrupted.

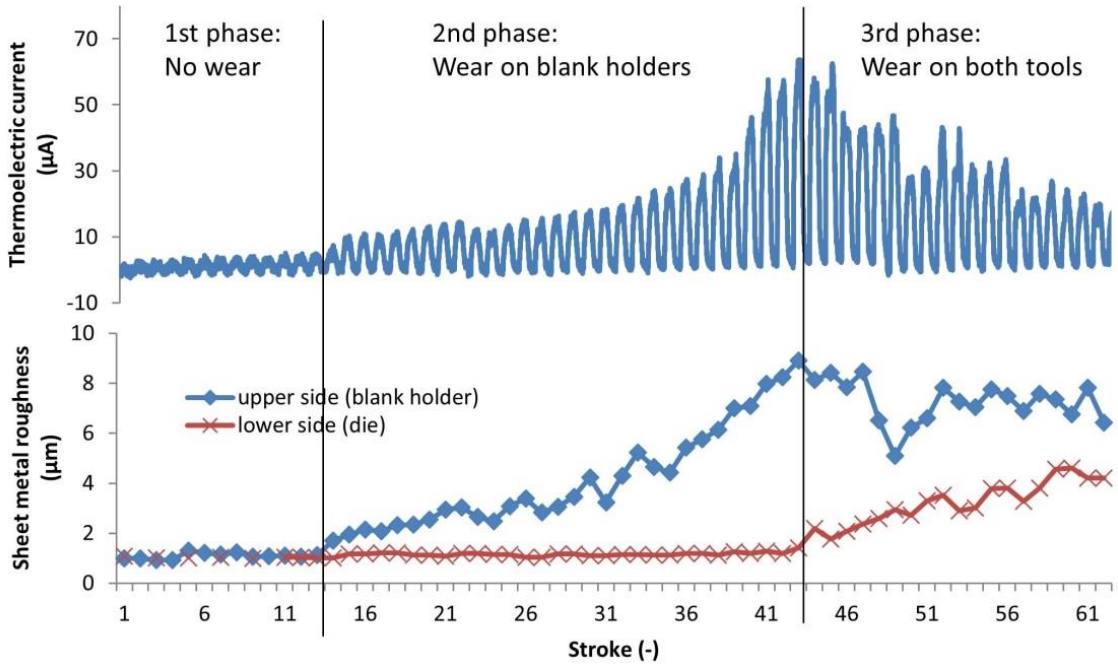

Figure 37 Case study for the explanation of the wear behavior after wear occurrence (tool: X153CrMoV12; sheet metal: H630LA, Source: [WU21a])

Figure 37 shows the measured thermoelectric current and the roughness on both sides of the sheet metal. After the occurrence of severe wear, the sheet is drawn for further 50 strokes (5 m of sliding length accordingly). By observing the thermoelectric current and the roughness, three phases of wear development can be identified. In the first phase, no change of roughness is observed on the lower side of the sheet, while the roughness of the upper sides increases only moderately until the 14th stroke. In comparison, the development of the thermoelectric current remains just above 0 µA in the low range and shows a linear increase up to the14th stroke with a value of 7.36 µA. In the second phase, the thermoelectric current increases abruptly from the 15th to the 44th stroke to a value of 62,83 µA. At the same moment, the sheet metal roughness on the upper side of the sheet metal increases abruptly up to the 44th stroke, which indicates a severe wear on the blank holder, while the roughness of the lower side of the sheet metal remains unchanged. From the 45th stroke onwards, the current starts to decrease and the wear development goes into the 3rd phase. The decline of the measured thermoelectric current can be derived from the increase of the sheet metal roughness on the lower side, which indicates a tool failure on the die.

Summarizing the results of the studies, it can be found that the thermoelectric current has an intense fluctuation after the occurrence of severe wear (see in Figure 29a and Figure 37). Therefore, interpretations are needed for this instable evolution.

4.6.2 Surface topography and thermoelectric current

For interpreting the instable thermoelectric current after wear occurrence, the correlation between the surface topographies, the roughness parameters and the thermoelectric current is determined. Figure 38 shows the thermoelectric current signal between the 24th and the 28th stroke of the test discussed in section 4.3 and Figure 29 (Test 1) in higher magnification. A sudden increase of the current can be observed at position 1 during the 26th stroke. A more detailed analysis of the upper surface of the sheet metal after this stroke with a high-resolution image and the respective surface topography is shown in Figure 38b. The width and depth of the groove on the sheet metal surface of Pos.1 grow drastically within a short sliding length. In particular, the depth of the groove has been increased by about 5 µm during a sliding movement of merely 2 mm length.

After the occurrence of severe wear, the thermoelectric current signal changes significantly with increasing sliding length (see Figure 38a). The reasons can be found in the obtained surface topographies between the tools in the 27th stroke. Pos. 2 and 3 depict the surface conditions at the beginning of the stroke and around the current peak value. Pos. 2 shows pronounced grooves, which clearly shows an abrasive wear on the sheet metal surface. This is caused by microcutting provoked by the pickups on the tool surface. On the other hand, the adhesive wear (galling) is observed next to the grooves in Pos. 3, which implies a mixed wear mechanism, abrasion and adhesion, on the sheet metal surface. Both mechanisms generate an increasing amount of heat in the contact zone. This phenomenon proves that the change of wear mechanisms has a very high impact on generated heat in the contact area, which causes the high difference of thermoelectric current between Pos. 2 and 3.

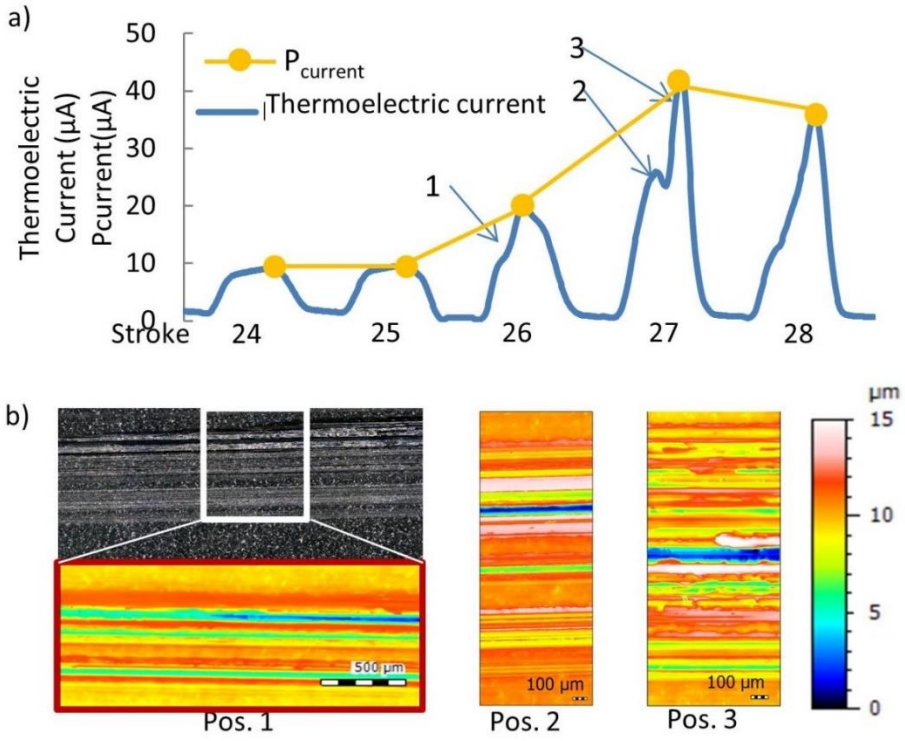

Figure 38 thermoelectric current signal and surface topography in the transition area (Source: [GRO19b])

4.6.3 Roughness parameters and thermoelectric current after severe wear

In section 4.3, the correlation between the roughness parameters R_a, R_z and the thermoelectric current is demonstrated before severe wear occurrence and at the transition. Compared with the surface roughness R_a, R_z and $P_{Current}$ after wear occurrence in Figure 30b and c, the thermoelectric current has a much greater change. Therefore, the correlation of the parameters in the “failure” phase of the wear development should be determined in a study.

Three different tribological systems, which were already used in section 4.5.2, are tested. The tests were run with the low alloy steel H630LA, aluminum alloy EN AW-1050 and EN AW 5083. The process parameters of the tests are summarized in Table 8.

Table 8 Test matrix: roughness parameters and thermoelectric current

Tool material	X153CrMoV12 (1.2379)

Sheet material	Low alloy steel H630LA (Manufacturer: C.D. Waelzholz) EN AW-1050A, EN AW 5083
Lubricant	Multidraw PL61 (Manufacturer: Zeller+Gmelin)
Lubricant amount	2 g/m^2
Normal force	10 kN
Number of repetitions	6

After the occurrence of severe wear, the sheet is drawn for further 10 strokes (1 m of sliding length accordingly). After tool disassembly, the tool surface roughness was measured through tactile measurement, which corresponds to the roughness of the "last stroke" (see Figure 35). Figure 39 shows the peak value of the thermoelectric current of the last stroke and the roughness of the wear mark R_t and R_z, based on standard DIN EN ISO 4287. It is found that the measured thermoelectric current correlates with the roughness parameter R_t, which indicates the highest peak value of wear marks. On the contrary, the roughness parameter R_z is not that sensitive to the change of the current. This effect can be explained by the higher micro-plastic deformation on the sheet metal, when the micro-asperities with high R_t on the tool surface cut the sheet metal. The higher deformation causes a higher temperature increase at the local area which leads to a higher thermoelectric current generation. This observation indicates that the maximal peak height of the wear marks plays a more important role on the thermoelectric current generation.

By comparing the results discussed in section 4.6.2 and 4.6.3, it can be found that the thermoelectric current is very sensible to the local surface change of tool asperities after wear occurrence. This surface change leads to a local plastic deformation on a microscopic level and a high temperature gradient, which generates a large amount of thermoelectric current. The correlation of Figure 39 indicates the possibility to detect this temperature gradient through thermoelectric measurements. This confirms that the tool surface degradation due to wear can be detected through thermoelectric measurement with high sensibility.

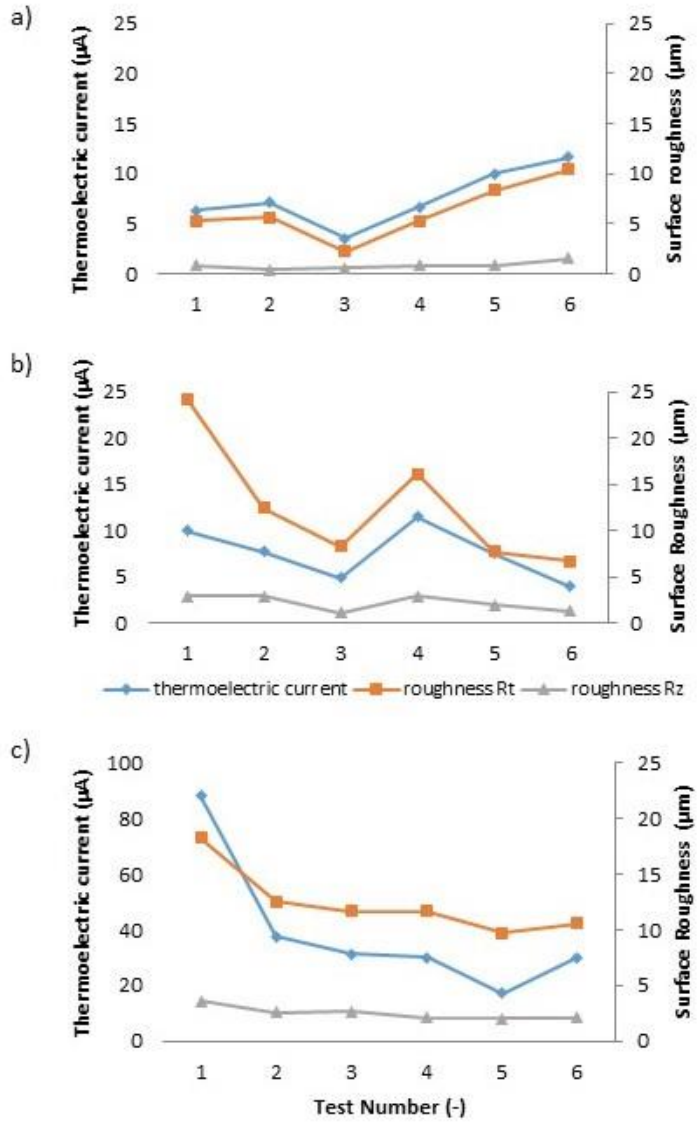

Figure 39 Comparison of the measured thermoelectric current and roughness a) EN AW-1050A; b) EN AW 5083; c) H630LA (Source: [WU21a])

4.7 Conclusions of the chapter

In this chapter, a new approach for inline wear detection through thermoelectric current is introduced. Sensitivity and reproducibility of this detection method for wear are approved. The correlation between the current and surface roughness is high, while the measuring frequency and resolution of thermoelectric current are much higher compared to conventional measuring methods as well. The

real-time capability of thermoelectric current measurements also has advantages in industrial applications.

Moreover, the influencing factors for thermoelectric wear detection are also investigated. Firstly, the Seebeck coefficient of the participating materials in the tribological system plays an important role in the sensitivity of wear detection. Secondly, after the occurrence of severe wear, the roughness parameter R_t has a better correlation than R_z to the thermoelectric current, which implies the higher sensitivity of the thermoelectric current to the local surface asperity change on the tool surface due to adhesion and abrasion.

Thirdly, the wear mechanism can also affect the measured thermoelectric current. By mixed wear mechanism, higher generation of thermoelectric current can be expected.

From this conclusion, it is stated that this new approach can serve as a promising method for wear detection with high potential for industrial applications, because of its real-time wear detection with high sensitivity. Moreover, no sensor is needed to be integrated inside the punch. This sensorless measurement provides a low-cost possibility for wear monitoring in forming processes. However, for further industrial applications, the following aspects should be considered:

(1) An optimal grouping of the combined Seebeck coefficient (the sum of Seebeck coefficient of tool and sheet metal) should be considered for an optimal sensitivity of the wear detection.

(2) For tribological systems with combined Seebeck coefficients close to zero, the effectiveness of wear detection through thermoelectric measurement is not favorable.

(3) For the tool design, a broader investigation of the isolation material is needed in terms of the mechanical strength, stiffness, fatigue strength, electric resistance and cost. The tool design with integration of isolation layer should consider further aspects of the production, such as the assembly/disassembly of the tools.

5 Influencing factors of wear resistance for tribological systems in sheet metal forming

After the discussion of the inline approach for wear detection in Chapter 4, a systematic method for wear prediction is considered. In section 2.3.3, the indirect method for wear prediction through wear resistance analysis is introduced. Christiany has developed a systematic method to characterize the load-dependent wear resistance and its wear behavior through the “wear resistance diagram (WRD)”, a diagram similar to “S-N curve” for fatigue strength analysis for materials [CHR16].

However, according to Archard’s wear model, the load is not the only factor which affects the wear resistance [ARC53]. The hardness and the surface topography of the bodies in the tribological system are also important factors. Conventionally, the hardness of tools is often processed as high as possible and the surface roughness are polished “as smooth as possible” to obtain an optimized wear resistance. These procedures can be challenged by raising the question, whether the tools with high hardness and smooth surface are always beneficial to the wear resistance of a tribological system. Furthermore, is it necessary to process the tool to the highest hardness and the lowest surface roughness in all circumstances? In this chapter, the influence of tool hardness and roughness on the wear resistance is characterized through wear resistance analysis. The results give answers to the questions posed above.

Besides the characteristics of the tools, the surface of the sheet metal can also affect the wear resistance. For corrosion prevention, the sheets are often covered with a galvanized coating. In car body drawing, in addition to contact forming, free deformation also exists. This leads to roughening of the sheet metal surface [LUD12, THO80]. According to Raabe et al., the surface roughening is caused by the elastic-plastic deformations which differ locally in the microstructure of the sheet material due to point defects and dislocations [RAA03]. The effects of the galvanized coating and its roughening due to pre-

straining on wear resistance and wear behavior are also discussed in this chapter.

In this study, the cold working steel X153CrMoV12 (DIN EN ISO 4957) and the nodular iron EN-GJS-700-2 (EN 1563 SYM) are used as tool materials, while the galvanized high-strength dual-phase-steels HCT980X and HCT580X serve as sheet metals. Both types of tool materials are widely used in sheet metal forming. Voids in the nodular iron are responsible for a premature damage of the material [BER01], which leads to a propagation of fracture inside the material [BAY04]. The performance of the two types of tool materials is evaluated based on the gained wear data. The wear development and the life span of the tools are determined through the inline thermoelectric measurement described in Chapter 4.

In the industrial application, worn tools often are reused after reworking processes such as grinding and polishing. For the wear type adhesion, a metallurgical change due to local welding on the tool surface occurs. This chemical changes cannot be eliminated through the physical tool reworking such as grinding and polishing. Therefore, it is also interesting to find out, whether the reworking of tools with adhesion history has an impact on the life span of the reused tools. This question will also be discussed at the end of this chapter. The contents of this chapter are part of the publications (co-)authored by the author ([GRO19b], [WU20] and [WU21b]).

5.1 Wear test setup

The influence of tool hardness and roughness as well as the characteristics of sheets on the wear behavior is investigated in strip drawing tests. A draw bead geometry is used for several reasons. Firstly, the tribological condition is extreme, since the contact stress can reach 800 MPa (tool material: cold working steel CP4M, sheet material: HCT980X). Secondly, the bending and unbending of the sheet due to the sliding through the bead leads to a pre-straining of the sheet surface, which helps to investigate the influence of surface roughening of sheet metals. Sketches of the draw bead geometry and the drawing direction of the sheet metal are shown in Figure 40. The penetration of

the draw bead in this illustration is 3 mm. The tool set consists of two blank holders with a rounding of 3 mm (BH1 and BH2), two dies (Die 1 and Die 2) and a draw bead (DB) with a radius of 5 mm.

During the process of draw bead testing, the sheet metal is bent three times at the rounding of the BH1, BH2 and the top of DB. According to the simulation results of Groche and Christiany, the contact stresses are locally concentrated and three critical positions with dominant contact stress can be defined [GRO13a]. The positions of high local stress are located on the rounding of the blank holders at both entrance and exit side (BH1 and BH 2) as well as on the top surface of the die at the exit side (Die 1). The three critical positions are marked as red points in Figure 40, where the contact stress at Pos. 1 is 694 MPa, at Pos. 2 810 MPa and at Pos. 3 794 MPa [GRO13a] for tests with the sheet metal HCT980X. The contact stresses on the exit side (Pos. 2 and 3) are the dominant ones and wear is most likely to occur at the Pos. 2 according to the Archard wear model [ARC53]. In the following part of this chapter, different wear tests are carried out as draw bead tests.

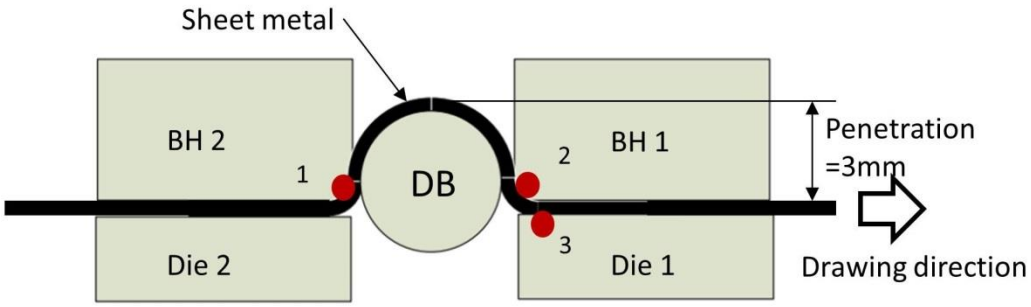

Figure 40 Draw bead geometry for strip drawing tests (BH=blank holder; DB=Draw bead)

5.2 Influence of tool hardness

For evaluating the influence of tool hardness, the cold working steel X153CrMoV12 is selected for the experimental investigation at five different hardness levels. The 4th level of tool hardness is identical to the sheet metal hardness. The scatter of the obtained life spans is determined by three test repetitions. The test matrix and the hardness of the tools after heat treatment are shown in Table 9 and Figure 41.

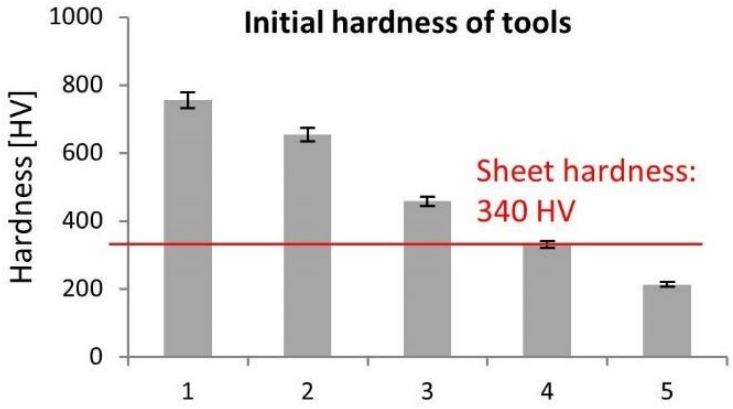

Figure 41 Influence of tool hardness on wear resistance: Initial hardness of tools (Source: [WU20])

Table 9 Test matrix: influence of hardness of tools

Tool material	Cold working steels X153CrMoV12 (DIN EN ISO 4957, 1.2379)
Sheet metal	HCT980X (DIN 10346), electro galvanized
Lubricant and amount	PL61 (Zeller Gmelin), 1 g/m^2
Normal force	25 kN
Velocity of drawing	100 mm/s
Length of each stroke	100 mm

Besides the thermoelectric measurement, the surface topographies of the tools are scanned after specified intervals (every 1, 5, 10, 50 m of sliding length).

The peak values of the thermoelectric current of each stroke as well as the surface roughness S_z of the tools are used to characterize the wear development of the tools with different hardness (see Figure 42). The roughness S_z is calculated from the obtained topographies (see Figure 43). Regarding the peak value of the thermoelectric current (Figure 42a), it can be found that the currents of the tools with the hardness level 1 to 3 are negative, while those with the hardness level 4 and 5 are positive. According to the principle of wear

detection through thermoelectric measurement (see Section 4.2), the loci of the higher thermoelectric currents determine the signs of the thermoelectric current. From the measured surface roughness (Figure 42b), the increase of roughness can be identified in the dies (D1) of the tests with hardness level 1 to 3 and in the blank holders (B1) of the tests with hardness level 4 and 5. No significant surface changes can be identified in other tools.

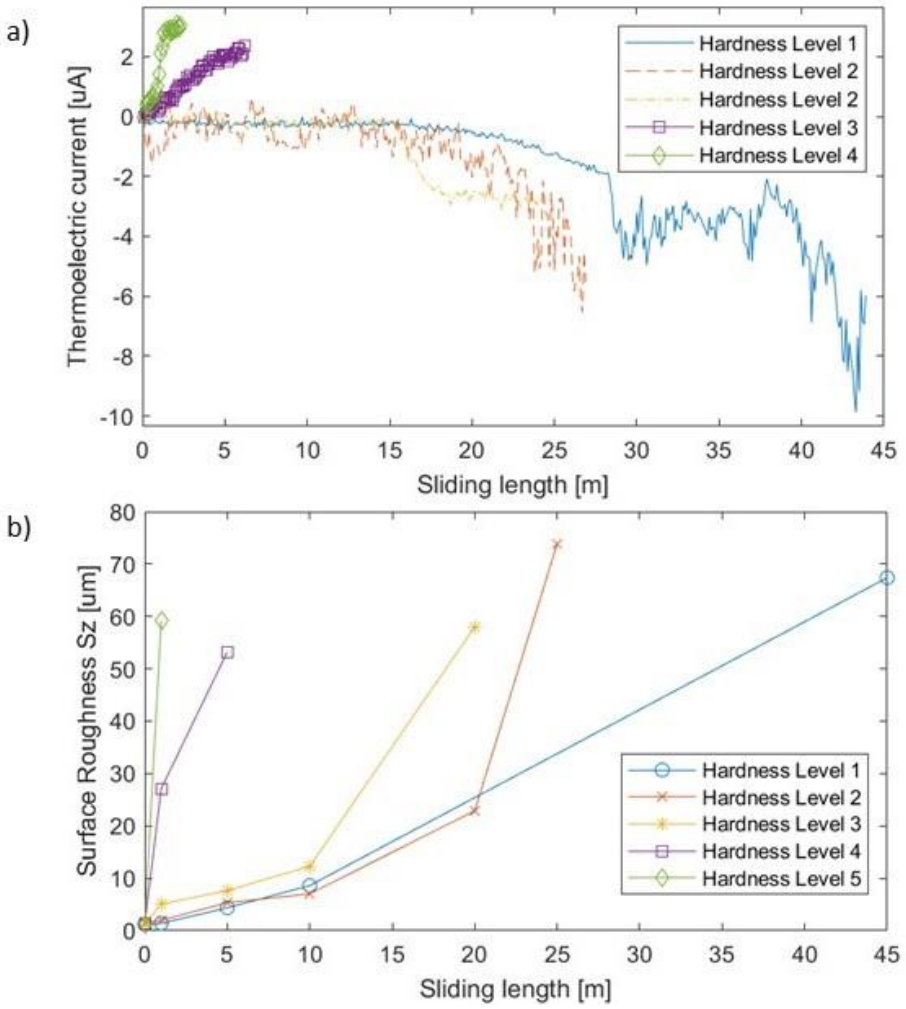

Figure 42 Wear development of tools with different hardness levels: a) Peak value thermoelectric current of each stroke; b) Evolution of surface roughness through the measurement of confocal microscope (Modified figure from [WU20])

Regarding the tendencies of the thermoelectric current, the evolutions vary with different hardness. The thermoelectric currents of hardness level 1 and 2 show a slight decrease at running-in and steady-state. After that, they decrease abruptly from the sliding length of 28 m (hardness level 1) and 22 m (hardness level 2) when exceeding the current value -2 µA. Comparatively, the current of

hardness level 3 decreases abruptly from 16 m of sliding length without any sign of transition. Other than the first three hardness levels, the wear development of tools with hardness level 4 and 5 does not show the phase “steady-state”, but increases linearly from the beginning of the sliding. Therefore, no transition phase can be identified in the curves of hardness levels 4 and 5.

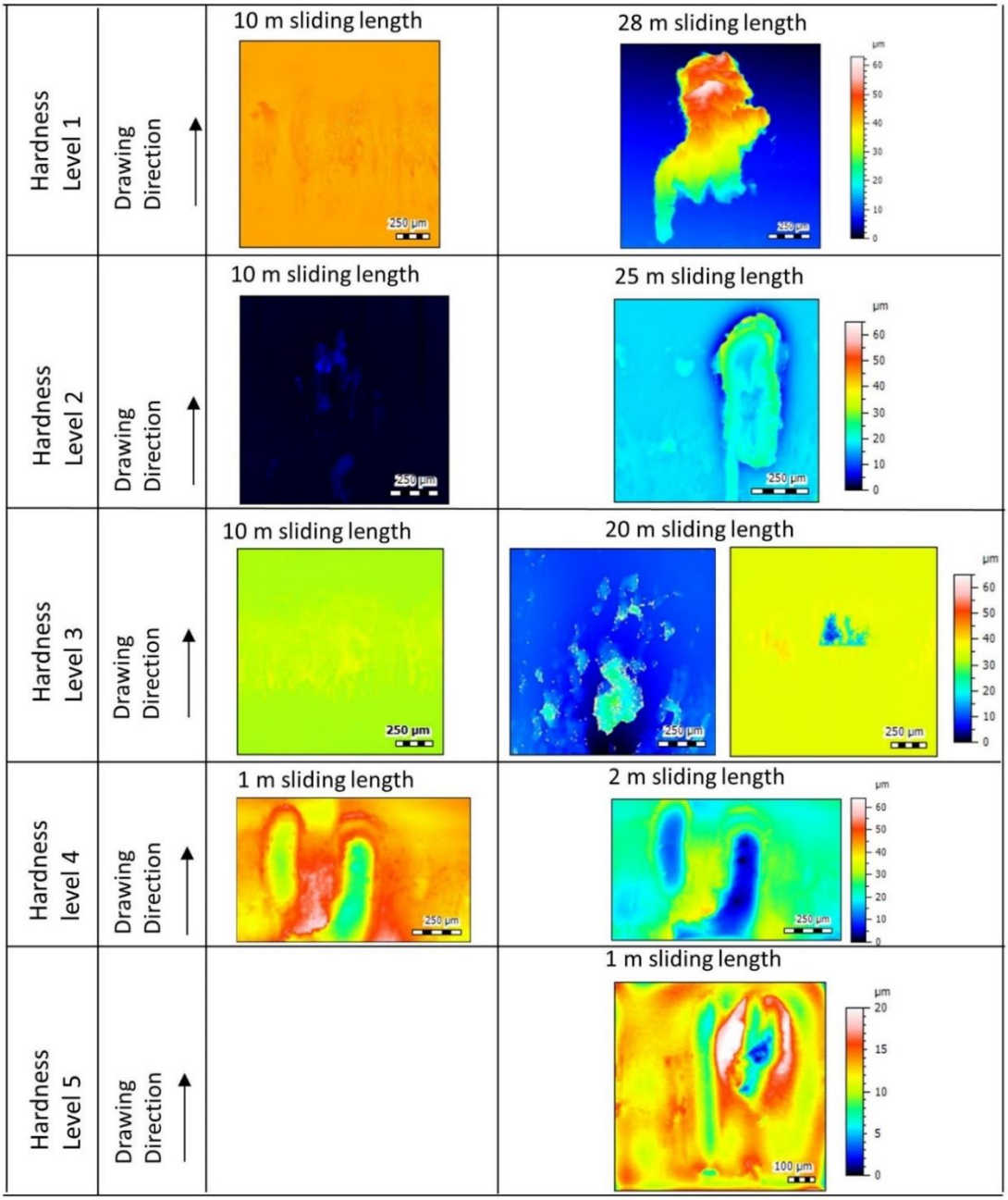

Figure 43 Topographies of wear marks during stationary wear (3rd column) to that of severe wear (4th column) for different tool hardness levels (Source: [WU20])

In order to explain the differences in the wear progress, the surface topographies of the wear marks for each test are scanned and shown in Figure 43. For the tools with hardness level from 1 to 3, the initial wear marks are detectable after a sliding length of 10 m (stationary phase of wear development). Following the initiated wear marks, the severe wear occurs at the same loci.

For tests with tool hardness levels 1 and 2, mild adhesive wear can be identified in the stationary state, indicated by only gradually increasing thermoelectric currents. Severe wear comes along with massive galling as a result of the cold-welding of the sheet metal coating on top of the tool surface. That leads to an abrupt change of the thermoelectric current and the surface roughness of the tools. On the contrary, the wear mechanism of the tool with hardness level 3 is different. Similar to hardness levels 1 and 2, the mild adhesion wear can be identified in the stationary state and an adhesion of galvanized coating (material zinc) can be identified on the tool. Nevertheless, the pitting on the tools can be regarded as another cause of severe wear on the tool due to the lower tool hardness. The tools with hardness levels 4 and 5 experience a plastic deformation just from the beginning of the sliding, which corresponds to a micro-ploughing. With the increasing of the sliding length, more material is removed from the surface and the grade of plastic deformation increases. This premature micro-ploughing leads to an increasing wear of the tools.

For the sake of reproducibility the analysis of the influence of hardness on the wear development, the tests are with three repetitions and the obtained life spans are depicted in a diagram with the ratio of tool hardness and sheet metal $\frac{H_W}{H_B}$ as the characteristic value. The WRD is shown in Figure 44. In terms of its evolution, it can be noticed that a higher hardness of the tools has a positive influence on the life span of the tools, which corresponds to the general understanding and Archard's wear model. According to the gradient, the curve can be separated into three zones. In zone 1, the tool hardness is lower than the sheet metal hardness. The micro-ploughing of the sheet metal asperities on the tool surface is the dominating wear mechanism, which leads to a premature tool failure within short sliding length. Moreover, an increase of the tool hardness has a restricted contribution to the life span improvement. Therefore, the tool hardness which is lower than the sheet hardness is not recommended to be

applied in forming high-strength-steels. In zone 2, the gradient of the curve is lower, which implies that an increase of the tool hardness has a positive effect on the wear resistance up to a specific tool hardness. Above this hardness level, the curve comes into zone 3 and the adhesive wear is the dominated wear mechanism. Because of the high gradient, the increase of tool hardness also leads to a limited improvement of the tool life.

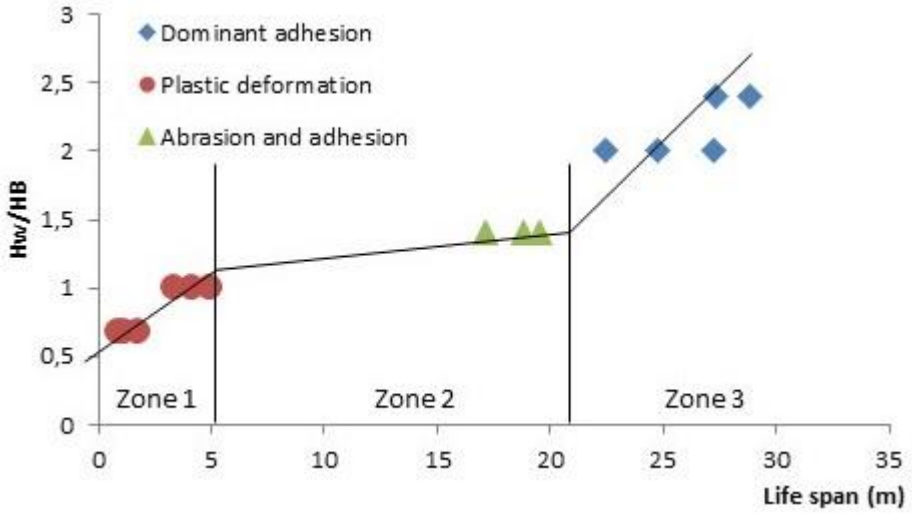

Figure 44 Wear resistance diagram (WRD): influence of tool hardness H_w : tool hardness; H_B: sheet hardness (Source: [WU20])

In summary, a tool with higher hardness is recommended to enhance the wear resistance, since higher hardness avoids the massive plastic deformation on the tool surface. A tool hardness higher than the sheet surface is mandatory for avoiding the pre-mature tool wear with high wear rate and low life span. Nevertheless, an optimized tool hardness $\frac{H_w}{H_B}$=1.4 can be identified, above which the wear resistance yields only in a limited increase. In the industrial application, it is recommended to select a proper heat treatment process in order to obtain the optimized tool hardness according to the production quantity.

5.3 Influence of surface roughness

The influence of the surface roughness on the wear behavior is investigated by studies with two types of tool materials, the cold working steels and the nodular

iron. These two types of material are widely used as tool material in sheet metal forming.

The tool surfaces are finished with four different processes: polishing, manual grinding with grain size 320 and 80 as well as sandblasting. For surface grinding, the groove direction corresponds to the drawing direction. Four roughness levels are obtained through this approach. The hardness of the tools is selected according to the hardness of typical industrial applications, i.e. 58 HRC (660 HV) for the cold working steel and 324 HV for the unhardened nodular iron. The test matrix and the initial roughness of the tools after finishing are shown in Table 10 and Figure 45. A surface area of 0.8×0.8mm is scanned through the confocal microscope µSurf. The ten-point height S_z as roughness parameter is selected to characterize the surface in the initial and the worn condition. The scatters of the measured surface roughness are determined by five repeated measurements on different samples.

Table 10 Test matrix: influence of surface roughness

Tool material	Cold working steels X153CrMoV12 (DIN EN ISO 4957, 1.2379)
	Nodular iron EN-GJS-700-2 (EN 1563 SYM)
Sheet metal	HCT980X (DIN 10346), electro galvanized
Lubricant and amount	PL61 (Zeller Gmelin), 1 g/m^2
Normal force	25 kN
Drawing velocity	100 mm/s
Length of each stroke	100 mm

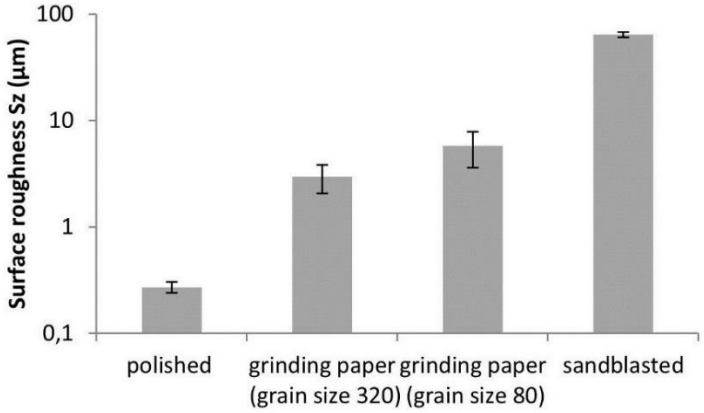

Figure 45 Initial roughness after surface processing (five levels) (Source: [WU20])

Figure 46 shows the measured thermoelectric currents and surface roughness S_z of the tools made of a cold working steel with different surface roughness.

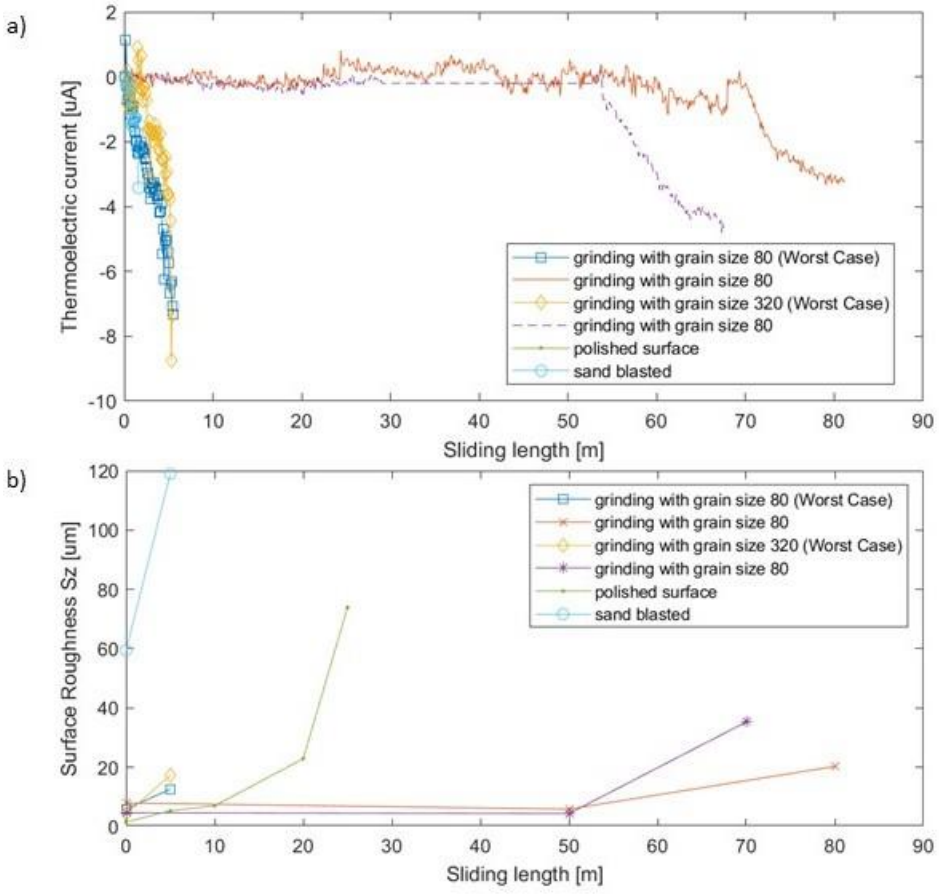

Figure 46 Tool wear development with different roughness levels (cold working steels): a) Peak value thermoelectric current; b) Surface roughness on dies (modified figure from [WU20])

The hardness of the cold working steel is 58 HRC (660 HV). From the evolution of the thermoelectric current, it can be found that the measured thermoelectric currents in the experiments with cold working steel are negative, which indicates a failure of the die. The surface roughness increases on the dies (D1) (see Figure 46b), which proves this statement.

Similar to the tools with polished surfaces, the tools ground with grinding paper of grain size 320 and 80 also experience the running-in, stationary and failure phases (see Figure 46a). The transitions can be identified after a sliding length of 55 m (grain size 320) and 71 m (grain size 80). The wear development of sandblasted tool is linear without steady-state. In order to analyze the influence of the wear development, the wear tests are repeated three times. When the thermoelectric current exceeds $\pm 2\ \mu A$, the tool's life spans are considered to be reached.

The same process is repeated for the tests with nodular iron. The development of thermoelectric current and surface roughness is shown in Figure 47.

On the contrary, all of the nodular iron tools experience a linear increase of wear. The measured thermoelectric currents of nodular iron are positive, which corresponds to a failure of the blank holders. The severe wear occurs on the nodular iron after a very limited sliding length. The thermoelectric current reaches $2\ \mu A$ only after a short sliding length. The steady-state of tool wear is not detectable according to the wear development. Even the tools with polished surface can only reach 3.2 m of sliding length. Smoother surface produced by polishing and grinding lead to merely longer life spans compared to those with rough surfaces. According to the Figure 47b, the roughness value S_z reaches in general over 50 µm after merely 5mm sliding distance. From the scanned topographies shown in Figure 48, both the galling and the adhesion of the sheet metal coating can be identified after a short sliding length. This characteristic shows that the nodular iron in the unhardened state is not suitable for forming high-strength-steels. It is deduced that the sheet material is prone to adhere on the surface of tools because of the voids in the nodular iron.

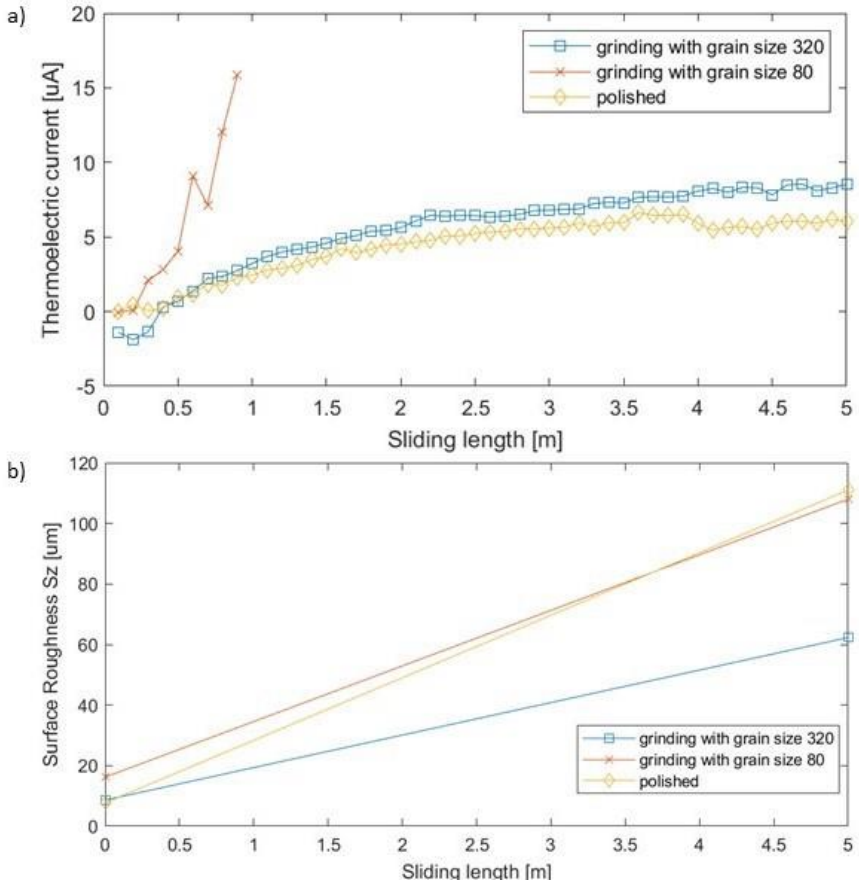

Figure 47 Tool wear development with different roughness levels (nodular iron): a) Peak value thermoelectric current; b) Surface roughness of the dies after specified sliding length (modified figure from [WU20])

Similar to the approach described in section 5.2, the life spans of all tests are summarized in a WRD for a broad analysis (see Figure 49). The surface roughness S_z is used as the characteristic value.

However, it is interesting to find in the WRD that the life spans of the tools after grinding have a great variation (see Figure 49). In the “worst case” of the three tests with ground surface, the wear development shows a linear development and the severe wear occurs after a short sliding length (see Figure 46a). Regarding the wear behavior, the adhesive wear occurs on the asperities of the rough surface directly for the worst cases (see Figure 50a and c), while the rough grooves after grinding in other cases are flattened at first and the galling occurs after a stationary state on the smoothened surfaces (see Figure 50 b and d). The differences can be explained by the fluctuations of the surface

topography created during the manual grinding operations. The distribution of the asperities on the surface is not homogeneous, which leads to a high difference in local surface pressures and deformations.

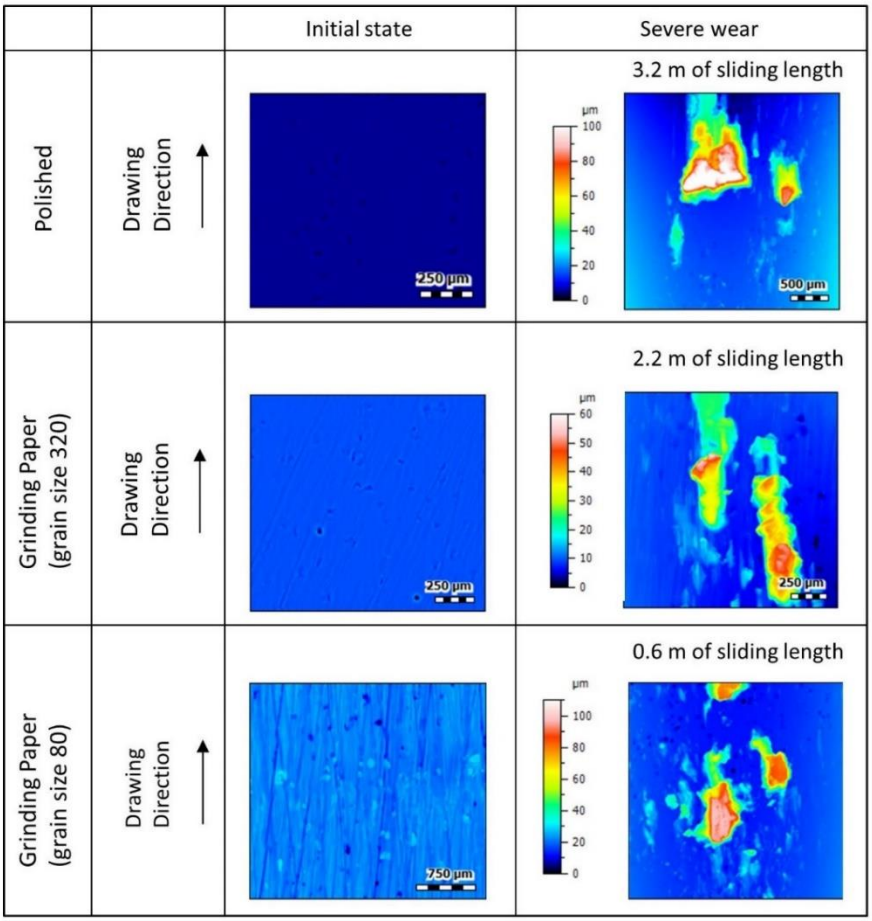

Figure 48 Surface topographies of tool surfaces: from initial state to severe wear (Nodular iron) (Source: [WU20])

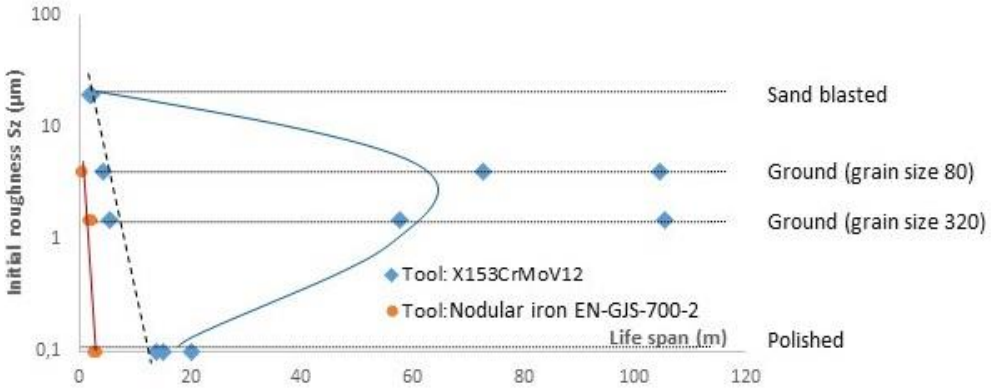

Figure 49 Wear resistance diagram (WRD): influence of tool roughness (Source: [WU20])

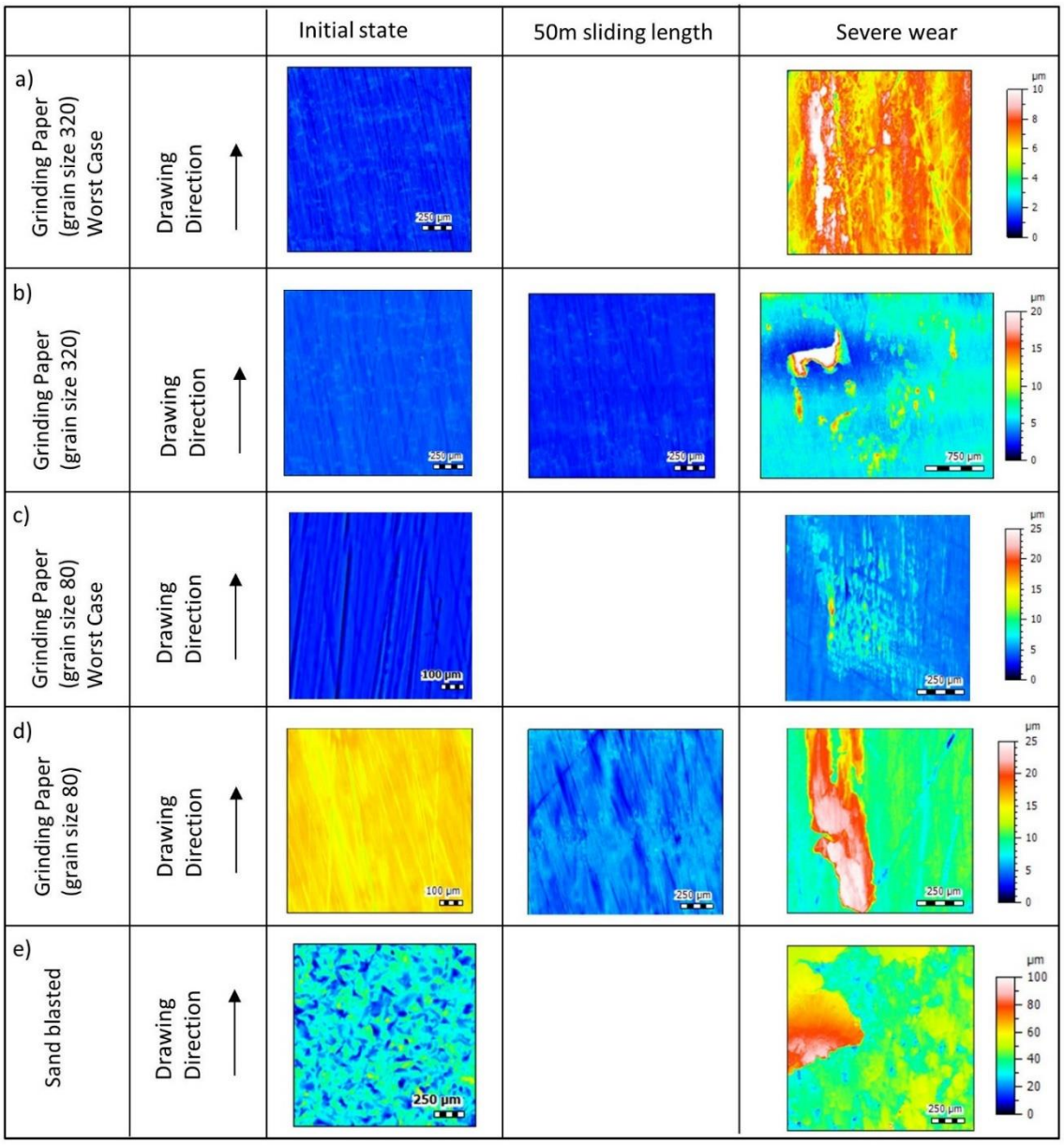

Figure 50 Surface topographies of tool surfaces: from initial state to severe wear (cold working steel) (Source: [WU20])

From the results of this section, it can be concluded that the nodular iron without heat treatment is not suitable for forming high-strength-steels because of its low hardness. In the case of the cold working steel, an optimized surface roughness can be identified on the WRD by observing the average life span (see Figure 49). It can be concluded that the surface with higher roughness causes in some cases a better wear resistance than those with lower roughness. In lubricated

circumstances, the grooves of rough surface serves as a storage of the lubricants and the debris detached from the tool surface. Under advantageous conditions, it is possible to build up a three-body contact consisting of lubricant and debris. The storage of the lubricants as well as three-body sliding reduce the friction and enhance the wear resistance. However, on the other side, severe wear can occur on the rough surface prematurely in worst cases and the wear resistance is smaller than the corresponding one of polished surfaces (see dashed line in Figure 49). Because of the large variation, it is risky to apply a rougher tool surface in sheet metal forming of high-strength-steels. Hence, the characterization of tool surfaces for wear resistance optimization is a good topic for future studies of wear behavior.

5.4 Influence of pre-straining on the sheet metal

Besides the tool hardness and surface roughness, the character of sheet metals also has an impact on the wear development. In car body forming, a free deformation without tool contact often takes place. In this case, the influence of sheet surface roughening due to contactless deformation on the wear development is of interest.

The dual-phase-high-strength-steel HCT580X (DP600) with galvanized coating Z140 (galvanizing amount 140 g/ m^2 on both sides) is selected for this investigation. Two different material types are used to characterize the strain-induced surface roughening on tool wear: the cold working steel X155CrVMo12-1 (1.2379) with a hardness of HRC 58, and nodular iron EN-GJS-700-2 (DIN EN 16482) with two different hardness levels (HRC 58 and 48). The summary of the experimental parameters is shown in Table 11.

Table 11 Experimental parameters for characterizing the influence of pre-straining

Sheet metal type	HCT580X, 50 mm width, 1.2 mm thick
Drawing velocity [mm/s]	100
Tool material	X155CrVMo12-1 (1.2379) 58 HRC; EN-GJS-700-2 (DIN EN 16482) 58 HRC;

	EN-GJS-700-2 (DIN EN 16482) 48 HRC
Lubricant amount [g/m^2]	2
Lubricant	Zeller Gmelin PL61
Blank holder force [kN]	30
Sliding length per stroke [mm]	100

Firstly, a numerical simulation of the strip drawing test with draw bead geometry is deployed to determine the pre-straining of the sheet metal during the test. The surface roughness after the pre-straining is also determined through surface scanning of the sheet surface with the highest pre-straining. After that, the wear tests are deployed for three different tools. Similar to the former approaches, the wear developments are determined through thermoelectric measurement. The obtained life spans and the contact stress are also summarized in WRD for a general analysis.

5.4.1 Process simulation of strip drawing tests with a draw bead geometry

First, the strain on the top and bottom side of the sheet metal during the strip drawing process is determined by numerical simulation. For a better illustration of the strain distribution on the sheet metal, a 3d numerical model is built up in the FE-Software ABAQUS, illustrated in Figure 51. The model consists of the bodies blank holder (BH1 and BH2), dies (Die 1 and Die 2) draw bead (DB) and the sheet metal. The tools are modeled as rigid bodies, while the sheet metal can be deformed elastic-plastic. The penetration of the draw bead is set as 3 mm. For tool strain evaluation, a coordinate system s is created with its origin at the beginning of the contact between BH2, Die 2 and sheet metal (see yellow line of Figure 51). Along the coordinate system s, a path is created in ABAQUS on both sides of the sheet metal and the strains are evaluated in the x-direction (PE11) and in the z-direction (PE33). The boundary conditions of the numerical model are illustrated in Figure 51.

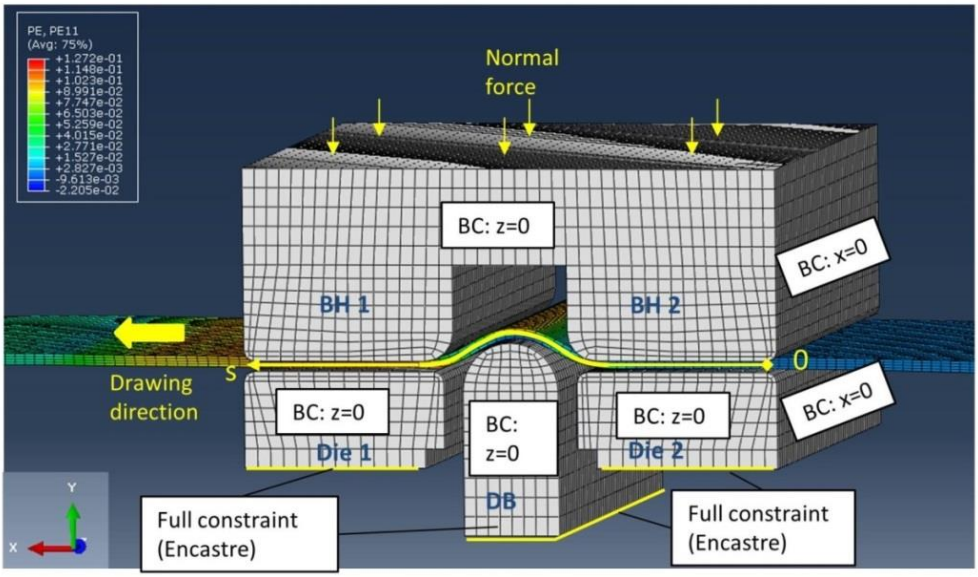

Figure 51 3d FE model for the determination of the strain distribution in wear tests with draw bead geometry (after sheet drawing with a distance of 40mm in drawing direction) (Source: [WU21b])

In order to evaluate the strain distribution in the z-direction of the sheet, three positions along the width of sheet metal are selected for strain evaluation and a path is created for each position on each side of the sheet metal. The strain in the center of the contact area (25 mm from edge) is characterized by path 1 and the strain at the edge by path 3. Path 2 characterizes the strain distribution in the middle between paths 1 and 3 (12.5 mm from edge). The evaluated paths are shown in Figure 52.

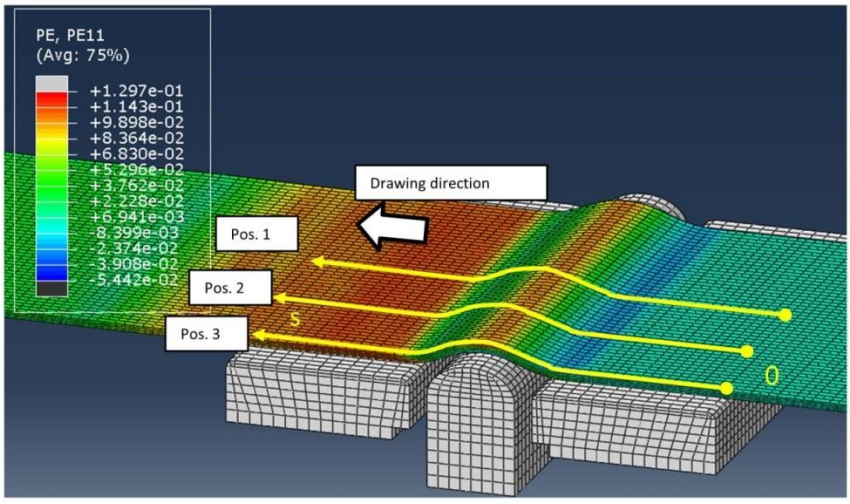

Figure 52 The evaluated paths for strain distribution on the sheet metal (Source: [WU21b])

Figure 53a and b show the strains at different positions on the top and bottom sides regarding the normalized coordinate system s. Between s=0 – 0.28, the contact zone between BH2 and Die 2 is located, while the contact zone of BH1 and Die 1 is positioned between s=0.72 - 1. In the area between s = 0.28 and 0.72, the sheet metal is bent three times. Since the surface roughening results from the free deformation without contact, only the maximal strain outside the contact area on both sides is evaluated. In general, the strain in x-direction is dominating. On the top side, the maximum strain in x-direction at the edge (s = 0.52, Pos. a) is 0.105, while the maximum strain on the bottom side in the center of the sheet metal (s=0.66, Pos. b) is 0.122. The corresponding strains in z-direction in Pos. a and b are negative.

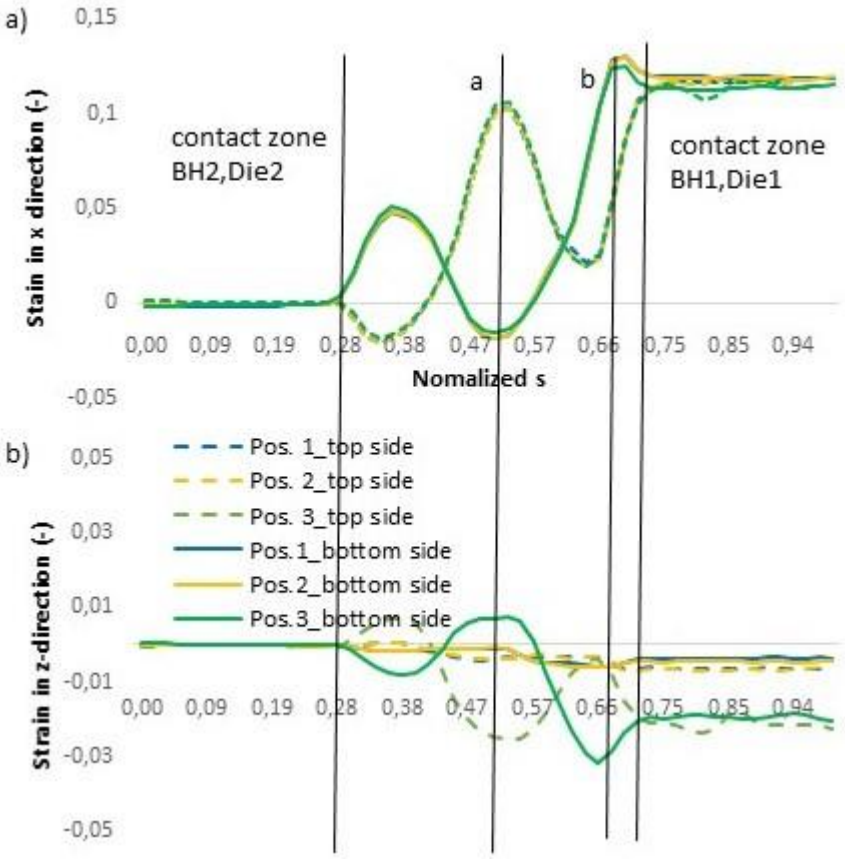

Figure 53) Numerically calculated strain in x-direction regarding normalized s; b) numerically calculated strain in z-direction regarding normalized s (Source: [WU21b])

The calculated maximum strain on the top and bottom sides are summarized in the diagram in the Figure 54a. It can be seen that the maximum pre-straining on the bottom side of sheet is higher than on the top side. With the sliding motion,

the resulting surface roughening on both sides will influence the tribological condition of the critical contact point on BH1 (Pos.2 of Figure 40) and on Die 1 (Pos. 3 of Figure 40). The measured surface roughness S_z in Figure 54b reveals that the strain-induced roughening in Pos. b (average value 10.4 µm) is more severe than in Pos. a (average value 9.2 µm), which is in accordance with the simulated maximum pre-straining in Figure 54a. It can be concluded that the sheet surface roughness after contact with the tools on Pos. 2 and 3 is different. Since the contact stresses at Pos. 2 and 3 are comparable, the influence of the surface roughness difference can be evaluated by means of a draw bead test.

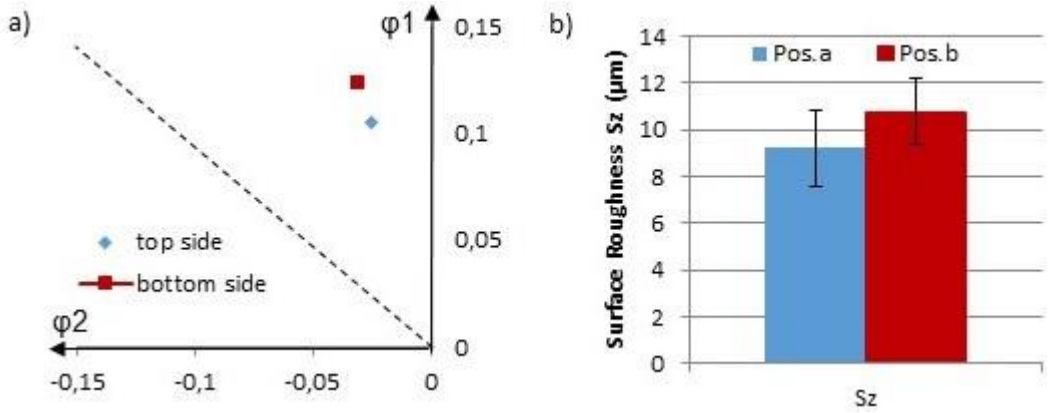

Figure 54 a) maximal strain on top and bottom side (top side: Pos. a; bottom side: Pos. b; d) surface roughness S_z at Pos. a and b according to 3d surface scanning through µSurf (Source: [WU21b])

5.4.2 Wear tests for characterizing the influence of pre-straining

The wear test of each tool is deployed once until severe wear occurs. The wear development is documented through the thermoelectric current, which is illustrated in Figure 55.

Regarding the measured thermoelectric current of the test with cold working steel, it increases from 0 µA to about 10 µA in the first 10 m sliding length. This is caused by the increasing temperature of the test tools as a result of friction. Between the sliding length 10 m and 70.2 m, the thermoelectric current is stable with only slight fluctuations. This implies that both temperature and wear conditions remains in steady-state. From the sliding length of 70.2 m, the

thermoelectric current starts to fluctuate in negative direction, which indicates the severe wear on the die (Die1 according to Figure 40). With the increasing sliding length, the amplitude of the fluctuation also increases, which is caused by the increasing severity of the die wear.

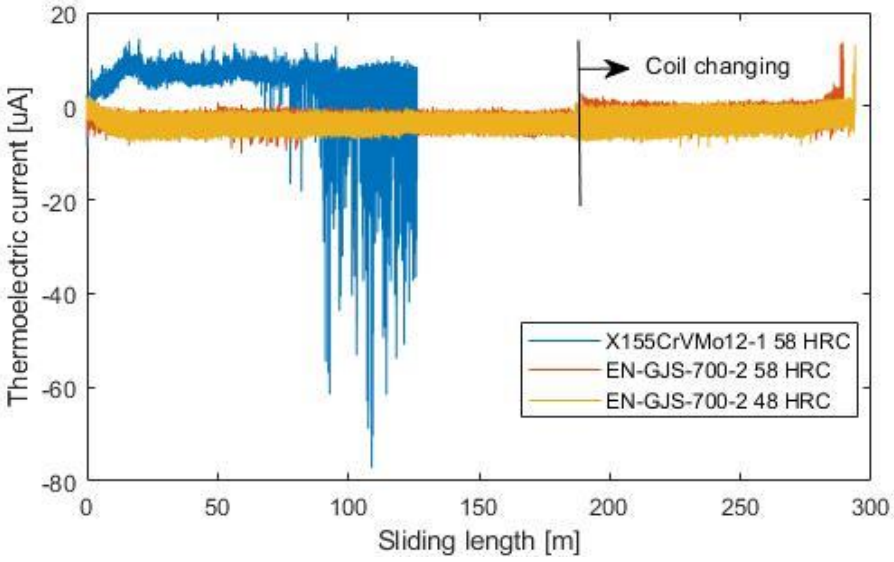

Figure 55 Evolution of thermoelectric current with sliding length in strip drawing test (modified figure from [WU21b])

The pictures of the tools after the wear tests in Figure 56a show, that adhesive wear marks (1 and 2) can be seen clearly on Die1. This corresponds to the measured thermoelectric current. The severe adhesive wear is mainly caused by the accumulation of zinc coating particles on the test tool. Wear mark 1 is located in the critical contact area (Pos. 2 of Figure 40), but the larger wear mark 2 is observed at the exit of Die1. This observation can be explained by the particle detachment from the galvanized sheet due to strain in the draw bead test. The study by Moghadam on the draw bead tests of ultra-high-strength-steel HCT980X with electrogalvanized coating also showed a similar wear mark distribution. The severe wear is mainly caused by the adhesion of the particle powdering [MOG19a]. This effect of strain-induced loss of galvanized coating is called “strain-induced powdering” by Rangarajan, which is mainly caused by bending and unbending strains in combination with the influence of contact stress and friction shear stress [RAN96]. Figure 53a shows that the sheet metal is bent three times before entering the critical contact area (Pos. 2 and 3), which

meets the demand of the strain-induced powdering effect. Under these circumstances, the strain-induced particles penetrate into the tribological system in the critical contact area between BH1 and Die1 and the resulting three-body contact may lead to great effects on the frictional condition and wear mechanism of the test tools. With the increasing sliding length, increasing number of particles penetrate and accumulate into the tribological system, which changes the distribution of contact stress in the tribological system and forms a new critical position with high contact stress. Pos. 2 of Figure 56a is such a new critical position, where large amounts of particles accumulate and a higher local contact stress occurs in this position.

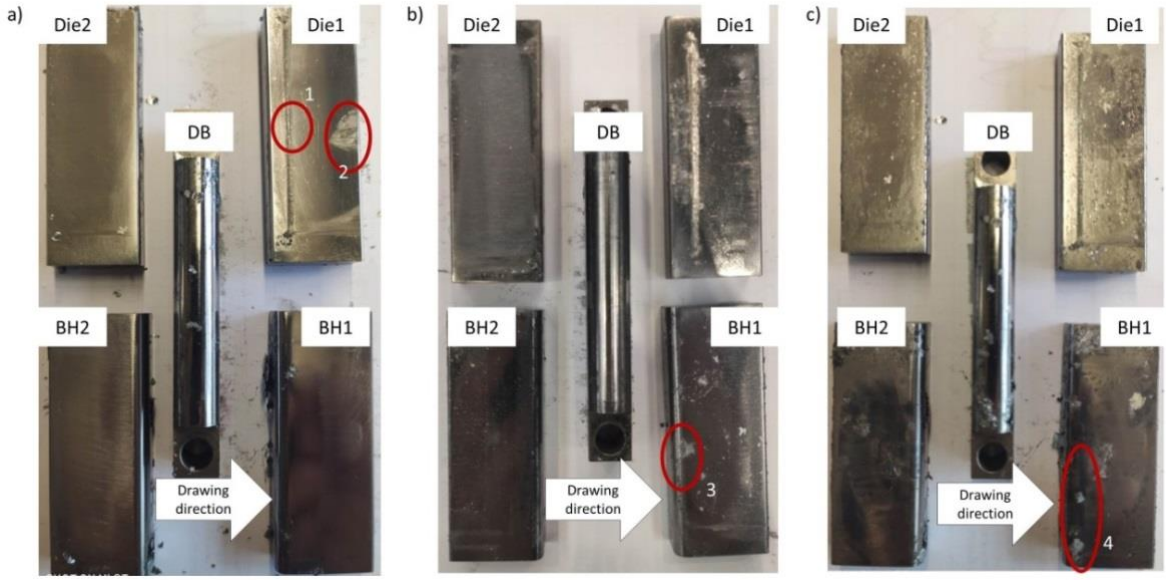

Figure 56 Wear marks on test tools after severe wear occurrence: a) 1.2379 with hardness HRC 58; b) EN-GJS-700-2 with hardness HRC 58; c) EN-GJS-700-2 with hardness HRC 48 (Source: [WU21b])

Compared to the signal derived with the cold working steel, the behavior of nodular iron is different. Two tool sets with different hardness (HRC 58 and HRC 48) are tested. Firstly, the measured thermoelectric current decreases to an average value of -3 µA within 5 m of sliding length and moves on to a steady state. After the sliding length of 180 m of both tests, the wear test is interrupted because of coil changing, which leads to a slight increase of the thermoelectric current because of the cooling of the test tools. However, the tendency of the thermoelectric current remains stable and the tool wear stays in steady-state. The steady state lasts until the sliding length of 287.5 m for the tools with higher

hardness (HRC 58) and 274.4 m for the tools with lower hardness (HRC 48) is reached. After the steady-state, the signals of thermoelectric current for both tool systems start to increase abruptly. This indicates the occurrence of severe wear on the blank holders of both tests. The adhesive wear marks can also be detected visually on the rounding of BH 1 (Pos. 3 and 4) of both tests, which is shown in Figure 56b and c. This observation also corresponds to the evolution of the measured thermoelectric current. The reason for a lower detected thermoelectric current in the test of nodular iron can be explained by the different Seebeck coefficients of different tool materials [TRÖ17b], which leads to different amounts of thermoelectric current.

5.5 Derivation of wear resistance diagram (WRD) with combined influencing factors and interpretations

In section 2.3.3, the specific wear force $\widetilde{F_V}$ (equation 13) has been introduced for wear resistance characterization. This parameter combines the influencing factors such as tool hardness, sheet hardness, roughness and contact stress. It implies the friction force, which leads to wear resulting from the sliding in sheet metal forming processes. The forming tools are much more prone to severe wear with higher $\widetilde{F_V}$ than that with lower $\widetilde{F_V}$ and accordingly the life span is shorter. With the help of this parameter, the life span and its wear behavior can be predicted with one characteristic value.

According to equation 13, the exponent n was not determined because of the lack of the wear resistance characterization with respect to hardness and roughness.

In this section, specific wear forces of the tested tribological systems of section 5.2 - 5.3 are first summarized in a WRD for the determination of the exponent n. The procedure for WRD derivation follows the approach of Groche et al. [GRO19a]. The results of the calculation are summarized in Table 12.

Table 12 Parameters and results to calculate the specific wear force

Tool No.	Influence factors	Contact stress	Pene-tration z	Tool hard-ness		Specific wear force $[N \cdot \mu m/mm^2]$		
		[MPa]	µm	HV	N/mm^2	n=2	n=3	n=4
H1	Hardness level 1	833	0.087	756	2510	4.591	2.002	0.873
H2	Hardness level 2	833	0.091	655	2190	7.262	3.631	1.815
H3	Hardness level 3	833	0.096	459	1485	24.382	17.979	13.257
H4	Hardness level 4	833	0.098	331	1060	68.221	70.473	72.80
H5	Hardness level 5	833	0.099	214	690	251.452	399.04	633.26
R1	Roughness level 1	833	0.091	655	2190	7.262	3.631	1.816
R2	Roughness level 2	833	1.412	655	2190	111.871	55.936	27.968
R3	Roughness level 3	833	4.239	655	2190	335.766	167.883	83.942
R4	Roughness level 4	833	16.8	655	2190	1331.25	665.63	332.81

Together with the obtained life spans of the strip drawing test from section 5.2 to 5.3, the WRDs are plotted. Since the exponent n of the model specific wear force (1) is limited to values around 3 based on the former considerations, three curves with n= 2, 3 and 4 are plotted in order to limit the exponent adequately (see Figure 57).

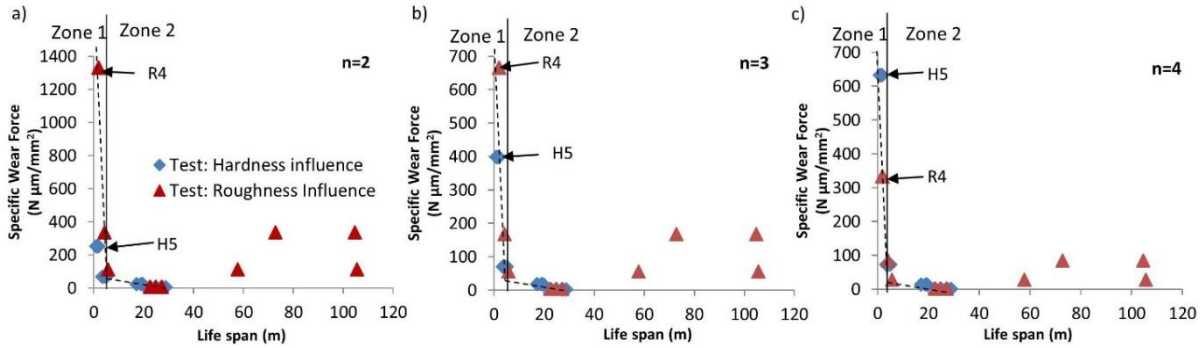

Figure 57 WRDs with variation of exponent n (Source: [WU20])

Similar to the approach in section 5.2 and 5.3, three repetitions have been conducted for scatter determination. In general, it can be found that the life spans of two tests with tool number R2 and R3 are considerably longer than in the third test (the “worst case”). Except for these four tests, the life spans of the other tests are distributed around a trend line (dashed line). This trend line can be divided into two zones of linear development. In Zone 1, the life spans of the tools are relatively short and the gradient of the trend line is high. This indicates that the tool life spans are sensible to the variation of specific wear force $\widetilde{\mathrm{F_V}}$. Comparing the distribution of the points along the trend line of the three plotted curves, it can be concluded that the characteristic curve with exponent n=4 is more feasible, since the life spans increase proportionally with the decreasing specific wear force. This conclusion is based on the points of the test number R4 and H5. The life span of the tools of test H5 are higher than that of R4, although the calculated specific wear force is lower in Figure 57a and b. Hence, $\widetilde{\mathrm{F_V}}$ can be written in the following form:

$$\widetilde{F_V} = \frac{{\sigma_N}^2 z}{H_T}\left(\frac{H_S}{H_T}\right)^4 \tag{26}$$

After the derivation of $\widetilde{\mathrm{F_V}}$, the calculated parameters and the specific wear forces of the tests in section 5.4 are summarized in Table 13. For the characterization of pre-straining, the reproducibility of the wear resistance analysis is not investigated because of a lack of material.

Table 13 Calculated parameters and specific wear force for wear resistance characterization (Influence of pre-straining)

Tool No		C1	N1	N2
Description		Pos.3 of 1.2379 (HRC 58)	Pos.2 of EN-GJS-700-2 (HRC 58)	Pos.2 of EN-GJS-700-2 (HRC 48)
Contact stress	$[MPa]$	486	486	486
Penetration z	[µm]	4.61	4.58	4.68
Tool hardness	HV	756	756	655
	$[MPa]$	2510	2510	2190
Sheet hardness	$[MPa]$	1095	1095	1095
Specific wear force(n=4)	$[N \cdot \mu \frac{\mu m}{mm^2}]$	82.4	82.04	127.53

According to Figure 54b, the strain-induced surface roughening of the sheet at Die 1 (Pos. b) is higher than that on NH1 (Pos. a). However, from the result of the calculated penetration z, the difference of the strain-induced roughening does not lead to a significant difference in the penetration depth z, which also does not lead to a significant difference in the specific wear force as well. This can be explained by the relatively high hardness difference between the tool and the sheet metal. The penetration of sheet asperities into the tools is suppressed due to its low hardness. Therefore, it can be concluded that strain-induced roughening has a minor effect on wear resistance.

The experimentally derived WRD is summarized in Figure 58. The wear development of different tests according to the measured thermoelectric current is also demonstrated. The linear development in Zone 1 is obvious and corresponds to the linear wear development according to Figure 42a, Figure 46a and Figure 47a. On the contrary, the gradient of the linear development in zone 2 is low and the wear progress shows the typical wear development (running-in, stationary and failure).

The life spans of test R2 and R3 (also see Figure 49) are two exceptions, which do not fit to the obtained WRD. Nevertheless, the worst cases of the test R2 and R3 do match the derived characteristic curve. It can therefore be concluded that

this curve is suitable for practical application, since only the worst cases are taken into account for the evaluation of tool wear in industrial manufacturing.

In the test which investigates the pre-straining influence, the specific wear force is smaller, since a relatively softer sheet (HCT580X) is applied. The life spans are much higher than for tribological systems with HCT980X, which also fits to the theory of specific wear force.

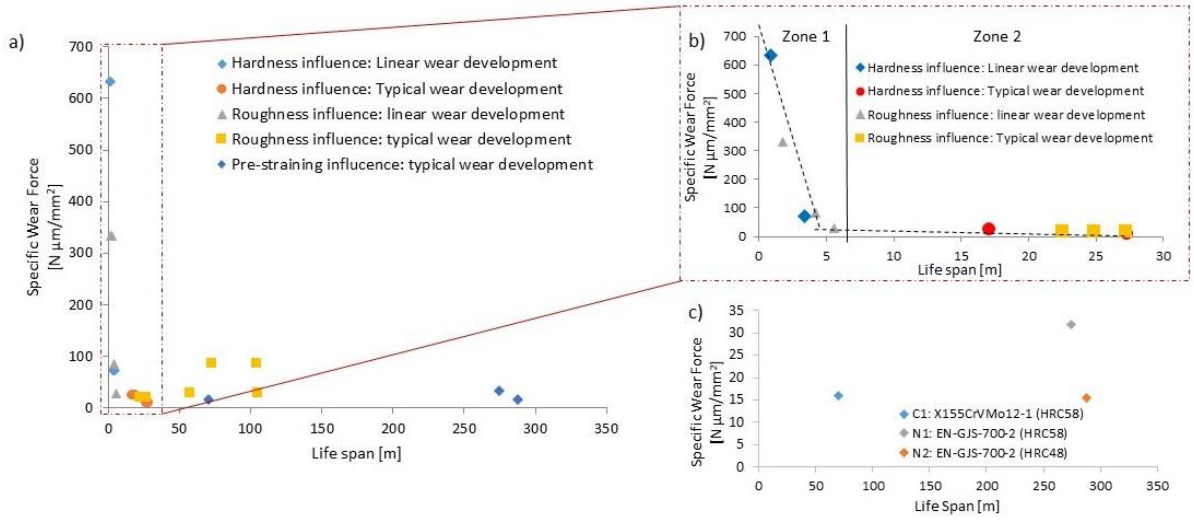

Figure 58 WRD by applying specific wear force a) All test data; b) Amplified points with low life spans; c) WRD with pre-straining influence (modified figures from [WU21b] and [WU20])

However, according to the detailed WRD with pre-straining influence (see Figure 58c), some interesting effects can be found. For similar tool materials with different hardness like EN-GJS-700-2 (HRC 58) and EN-GJS-700-2 (HRC 48), the higher specific wear force results in a lower wear resistance. Although the different types of tools X155CrVMo12-1 (HRC 58) and EN-GJS-700-2 (HRC 58) have a similar specific wear force, the life span is significantly different.

For the explanation of this observation, the powdering effect mentioned in section 5.4.2 is regarded as the main reason. The strain resulting from bending leads to the formation of particles from galvanized coating. Figure 59 shows the size of abraded particles from the experiment with nodular iron EN-GJS-700-2 and cold working steel X155CrVMo12-1. It is shown that the size of the particles from the experiment with the cold working steel is about 6 times larger than that from the experiment with the nodular iron. Bayer states that the small particles

in combination with the lubricant build a so-called three-body sliding, which is in some circumstances beneficial to friction behavior and wear resistance of the tribological system [BAY04]. Furthermore, the large particles, which penetrate into the tribological system, cause the change in the contact stress distribution. It is also difficult for the big particles to escape from the tribological system, which leads to an accumulation of particles inside the contact area. That explains why the tool made of nodular iron shows a higher wear resistance than that made of the cold working steel at similar specific wear force. The change of contact stress distribution as a result of particle accumulation can explain the severer wear mark on the exit side (Pos. 2) compared to the critical contact area on Pos. 1 of Die 1 (see Figure 56a).

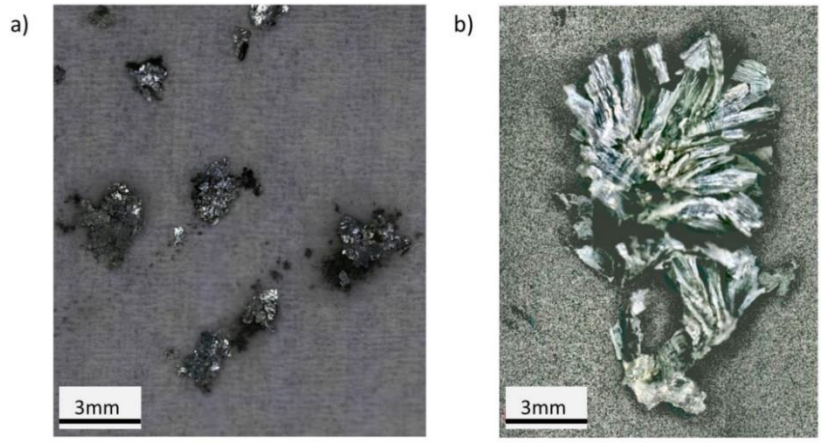

Figure 59 Illustration of abraded particle size of the galvanized HCT580X under Zeiss microscope Smartzoom 5 a) particles in experiment with nodular iron EN-GJS-700-2; b) particle in experiment with cold working steel X155CrVMo12-1 (Source: [WU21b])

For interpreting the reason for the different sizes of particles, the surface topographies of wear marks on positions where severe adhesive wear occurs (Pos. 2 on nodular iron and Pos. 3 on cold working steel according to Figure 40) are analyzed. It is obvious that a pitting is formed as a result of the extreme stress on both kinds of tools. From the 2d-profile of the pitting (see Figure 60c and f), it can be found that a bulge is formed before the pitting with a height of about 6 µm due to the plastic deformation (micro-ploughing). The bulge resists the sliding of the sheet in the drawing direction, which leads to a separation of the galvanized coating and a formation of particles with larger size. Comparatively, small particles are formed, since no such bulge is formed. In

addition, the depth of pitting on cold working steel is higher than on nodular iron. These different types of 2d-profile and the depth of pitting can be interpreted by Gahr's microplasticity theory, who stated that the section view of wear groove is composed of three parts, the groove and two bulges. The size of the bulges is determined by the plasticity of the material. For brittle material, the height of the bulge is small, while for ductile material the bulge height is larger due to the material plasticity [GAH88]. For the two investigated materials, a bulge is formed on the surface of the tools made from ductile cold working steel, which causes the formation of larger particles.

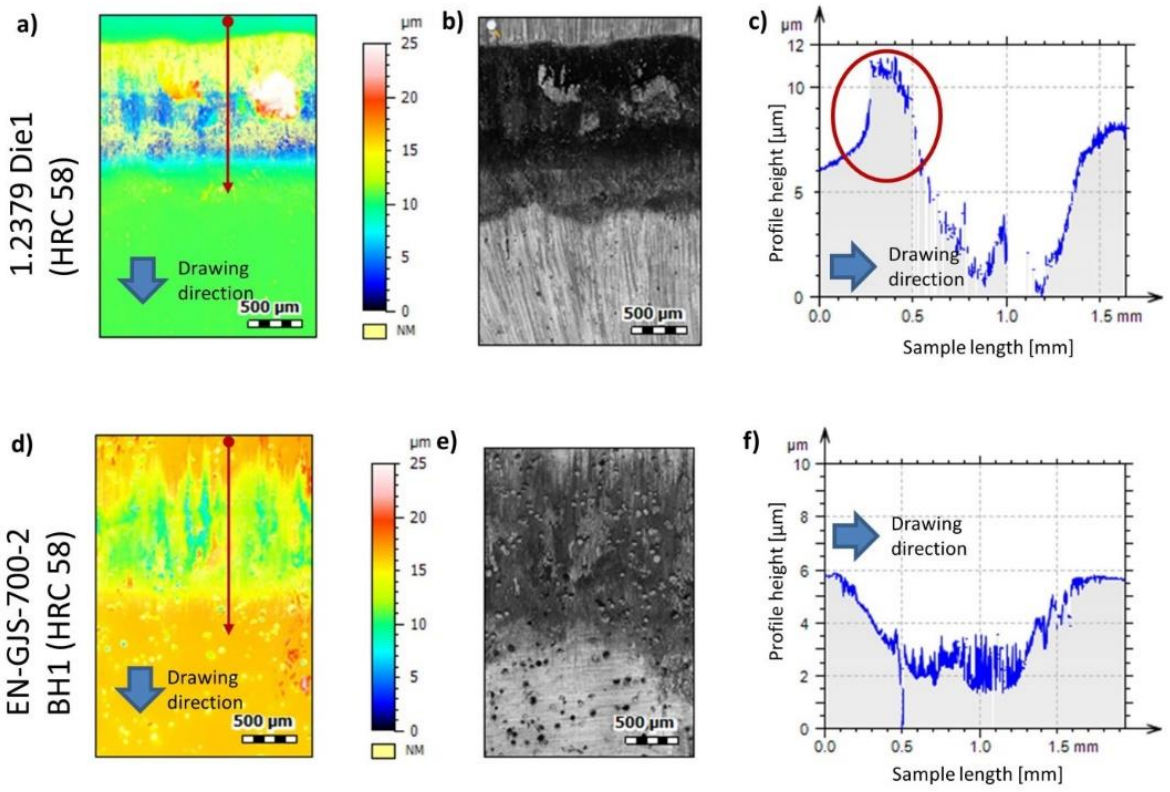

Figure 60 a) Surface topography ; b) Optical picture; c) 2d profile of the wear mark on Die1 made of cold working steel X155CrVMo12-1; d) Surface topography ; e) Optical picture; f) 2d profile of the wear mark on BH1 made of nodular tool EN-GJS-700-2 (Source: [WU21b])

Summarizing all the evidence revealed in this section, it is possible to predict the wear development and estimate the life span of the forming tools in tribologically similar systems with the help of the WRD. With the calculation of the parameter specific wear force $\widetilde{F_V}$ and the determination of the behavior of

wear development (linear or typical “three phase”), the life span can be predicted correspondingly through WRD.

5.5.1 Summary of the study

From this study, several exceptions in the WRD can be found. For example, tool with higher roughness can extend the life spans, but in worst cases, its wear resistance can be lower than those of polished surfaces. This effect can be explained by the indeterministic surface processing of rough surface. However, the positive effects of high surface roughness is worth to be studied in future investigations.

Another exception is the influence of pre-straining. From the obtained WRD, it can be concluded that strain-induced surface roughening has little effect on the wear resistance. However, the abrasive particles caused by strain, especially bending and unbending, cannot be ignored in wear resistance investigations. The size of the particles plays an important role in the wear behavior and in the tool life span.

In industrial production, the tool reworking through grinding and polishing of the worn-out tools is a very common approach for tool reuse. Therefore, the life spans of the tools after reworking are also interesting for industrial applications. This investigation will be discussed in section 5.6.

5.6 Influence of tool reworking on tool life spans

In industrial forming processes, worn-out tools often have to be repaired by welding, cutting, grinding and polishing operations to achieve the initial state for further utilization. In this study, a tool is reworked by grinding and polishing after reaching the transition zone between stationary and severe wear. The wear behavior of the reworked tools is compared with new tools.

Three worn-out tools are selected for further investigations. The test matrix is shown in Table 14. For Test 1 and 2, the worn-out tools of the approach in section 5.3 are reworked, while test 3 corresponds to the rework of tools described in section 4.4.

Table 14 Experimental study: life span after tool reworking

Test number	1	2	3
Tool material	Nodular iron EN-GJS-700-2	Cold working steels X153CrMoV12	
Sheet materials	HCT980X with galvanized coating		H630LA
Initial surface	Polished		
Initial hardness	324 HV	720 HV	
Procedure of reworking	Grinding paper with 80 grain size → 320 grain size → polishing		

The wear detection is also deployed through thermoelectric measurement. The test is aborted three strokes after reaching the threshold value of the thermoelectric current. The worn-out blank holder and die are ground and polished until the initial state of surface topography is reached.

The initial hardness, the hardness of wear mark and reworked surface are summarized in Figure 61. It can be found that the tool hardness of Test 2 (cold working steel) cannot be significantly changed through reworking, while an improvement of the tool hardness of nodular cast iron (Test 1) after reworking is detectable.

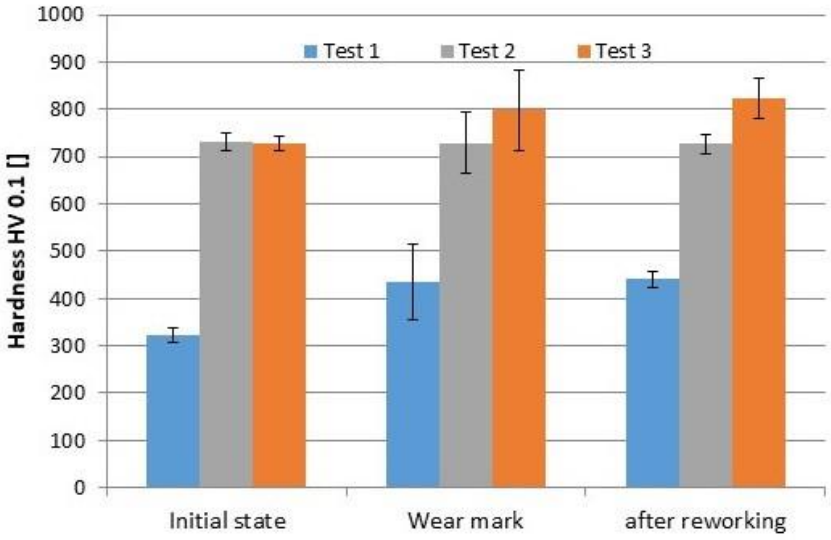

Figure 61 Tool Hardness before and after reworking (Modified from figures of [GRO19b] and [WU20])

In terms of the life spans of tools after reworking (see Figure 62), the life spans of Test 3 have extended dramatically after reworking. For the other two tests, no clear improvement can be found. This observation can be caused by hardness improvement of Test 3 (see Figure 61).

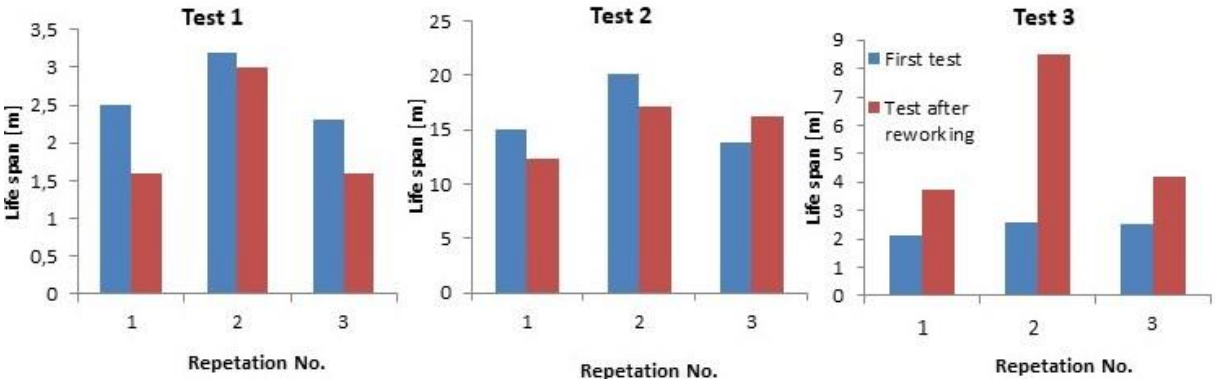

Figure 62 Life span of tools before and after reworking (Modified from figures of [GRO19b] and [WU20])

The life spans of nodular iron have not improved after reworking, although the hardness improves after reworking. From the section view, it is deducted that the adhesion is caused by the accumulation of zinc coating initiated from the voids on the surface (Figure 63). After reworking these voids are still visible, which explains the limited contribution of rework to the reduction of adhesion on the tool surface for nodular iron.

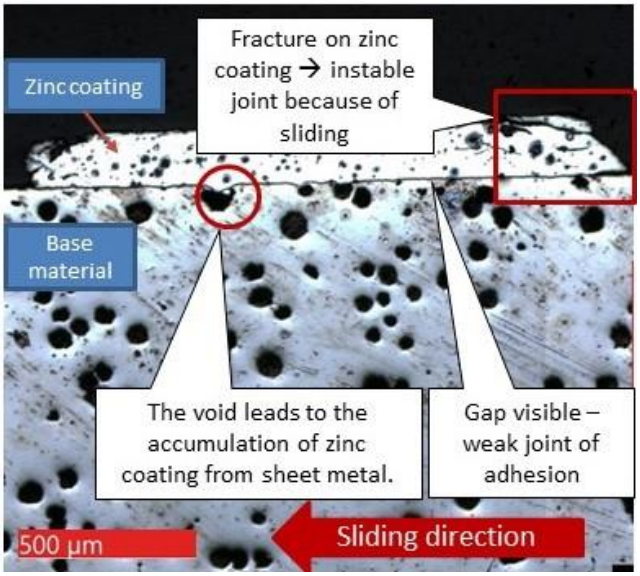

Figure 63 Section view of adhesion on nodular iron2 (Source: [WU20])

This difference in wear behavior between the different studies with cold working steels (Test 2 and 3) can be explained by the different wear mechanisms of different sheet types. The severe wear of test 1 and 2 is caused by the joining of the galvanized coating from the sheet metal with the tool. The joining is weak since a gap between the adhesive mark and base material is visible. Additionally, fracture can be seen from the section view of adhesive marks (see Figure 63). It implies that the wear mark is instable because of its lower hardness.

Comparatively, galling in test 3 is caused by the chemical reaction between the base materials of tool and sheet metal. The robust joint of the base material and the tool surface is depicted in the section view of Figure 64. A high density of plastic deformation close to the surface can be identified. Unlike the joint of Test 1 and 2, no gap can be identified between adhesive mark and base material of tools, so the joint of adhesive wear is more robust. This kind of robust joint fosters an increasing work hardening of the tool surface, which further improves the hardness after reworking.

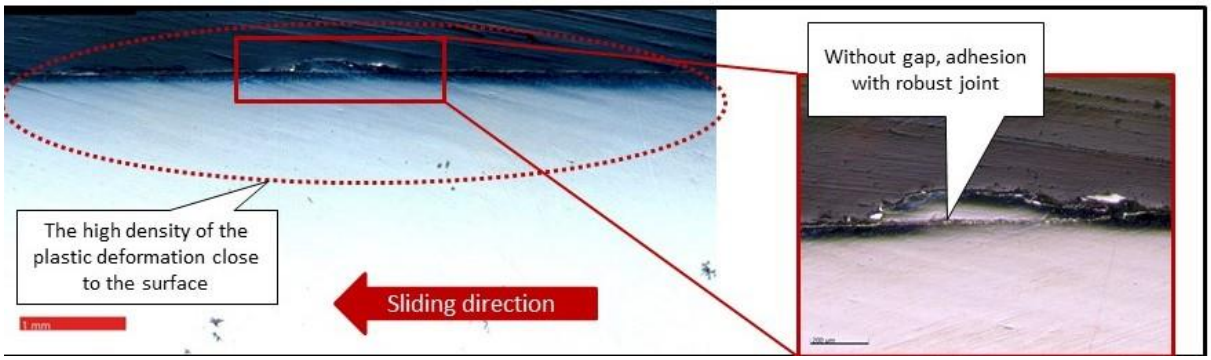

Figure 64 Section view of cold working steel (Test 3) (Source: [WU20])

From the test results of the section, it can be concluded that the judgement of the effectiveness of life span improvement after reworking cannot be based merely on the hardness before and after tool reworking. Several other factors such as the wear mechanisms and the structure of the tool surface should be taken into account.

5.7 Summary

In this section, the influence of tool hardness, roughness and pre-straining of sheets on wear development are discussed. The wear resistances of the investigated tribological systems are analyzed through WRD. The following conclusions are drawm:

1. An adequate tool hardness is mandatory for a satisfying wear resistance. For the tested tribological system, an optimized hardness feature between tool and sheet (e.g. $\frac{H_W}{H_B} = 1.4$ in section 5.2) can be determined for an optimized resource efficiency.

2. A perfect “smooth” surface with low surface roughness does not always lead to a perfect wear resistance. Sometimes, a surface texture with higher roughness extends possibly the life span, but it can also lead to pre-matured wear occurrences after a short sliding length. Therefore, the influence of surface texturing on wear resistance is a future research direction with promising potential.

3. The surface roughening due to pre-straining of a free deformation has a limited influence on the wear resistance, but the effect of strain-induced powdering of galvanized coating of sheets on wear is unneglectable.

4. WRD is a good tool for life span prediction. The parameter specific wear force $\widetilde{\mathrm{F_V}}$ can also serve as a characteristic value for wear resistance quantification.

5. The reworking of a worn-out tool can extend the tool life span for future use, when the worn-out tool is based on the galling. Due to the high-strength joining caused by a plastic deformation of the base material, a local case-hardening occurs, which leads to an increasing hardness after tool-reworking. However, the reworking of adhesive wear due to powdering of abraded particles does not help to extend the tool life span.

6 Estimation of wear resistance curves (WRC) for life span estimation

6.1 Introduction

After the investigation of the method for wear detection and different influencing factors, the investigated method for wear prediction will be applied in an actual application of a forming process.

As discussed in section 2.3.3, a method for wear prediction using the life span estimation through wear resistance diagrams (WRD) was developed. These diagrams have been used to characterize the wear resistance of different tribological systems in laboratory tests [GRO19a]. The WRD summarizes the tool life spans under different contact stress, quantified by the reachable sliding length in the strip drawing test. The results of previous studies show that the life spans deviate significantly at different load levels, not only in terms of the absolute value of life span, but also in the scatter of the life spans under the same stress conditions. At lower load levels, the obtained life span und its deviation increase dramatically, while at higher load levels the life span is significantly lower and its deviation decreases distinctively [CHR16, GRO19a]. In chapter 5, the WRD is used to characterize different influence factors on wear resistance such as tool hardness, roughness and pre-straining of sheets.

The main barrier for the WRD application is the required amount of wear data, especially at lower tribological loads. So far, data have been obtained at high contact normal stresses and comparatively low total sliding length. Based on these data it is difficult to predict tool life under the contact stress usually found in industrial forming processes. Moreover, WRD is composed by scatter points, so it is difficult to estimate the life spans at all required load levels. In order to extend the general application of WRD, an extrapolation of the derived data is required. Therefore, a wear resistance curve (WRC), based on WRD, described by a mathematical model is proposed. Since the concept of WRD was inspired by the S-N curve of the material fatigue strength estimation [CHR16], the transferability of the S-N curve estimation approaches to wear prediction is investigated in this chapter. In addition, the duration of a strip drawing test for

life span determination is very lengthy [GRO13a], so it is necessary to discuss possibilities to obtain a satisfactory estimation by performing as few tests as possible. In this chapter, only the behavior and its established WRC of uncoated tools are discussed. The behavior of tools with coating will be discussed in the case studies in chapter 7. The contents of this chapter are part of the publications (co-)authored by the author ([WU22]).

6.2 Approaches for WRC estimation

The pre-selection of fitting models and the mathematical approaches for curve fitting based on Maximal Likelihood Evaluation (MLE) are described in Appendix 2. Four models for S-N curve estimation with highest citing frequency are selected for WRC estimation, shown in Table 15.

Table 15 Pre-selected models and equations

S-N curve models	**Original equation**
Basquin	$p = \alpha(L)^{\beta}$
Weibull	$p = p_{uT} \cdot \exp(-\alpha(\log L)^{\beta})$
Henry and Dayton	$p = \frac{\alpha}{L} + \beta$
Hwang and Han	$p = p_{uT}(1 - \frac{L^{\beta}}{\alpha})$

Four WRDs of four tribological systems with uncoated tools are discussed for WRC estimation. These include tribological systems with both high and low wear resistances. The tested tribological systems are summarized in Table 16. The wear data of the tribological systems No. 1, 2 and 4 are based on the author's former research [GRO19a, GRO19b]. The data amount and its load levels are also summarized in Table 16.

The first two tribological systems have a relatively high wear resistance (over 500 m at a contact stress of 590 MPa), while the other two tribological systems have relatively low life spans (within 10 m at the contact stress of 200 MPa). In

this study, it is interesting to discuss the compatibility of the pre-selected models on the WRC estimation for tribological systems with both high and low life spans.

Table 16 Tested tribological systems with uncoated tool

No.	Tool	Sheet metal	Data amount	Load levels	Lubricant
1[GRO19a]	CP4M	DP980	15	3	PL61 of Zeller Gmelin Amount 1 g/m^2
2[GRO19a]	CP4M	ZStE1000	9	3	
3	X153CrMoV12	X5CrNi18-10	19	5	
4[GRO19b]	X153CrMoV12	H630LA	12	3	

In the tribological system No.3, the cold working steel X153CrMoV12 (1.2379) is the tool material and the stainless steel X5CrNi18-10 (1.4301) the sheet material. It is also a critical tribological system with low wear resistance [MOG17a]. For this tribological system, 19 tests are deployed under five load levels. The life span of the tribological system is obtained through the measurement of thermoelectric current, which is described in section 4.2.

For WRC estimation, the parameter p_{uT} should be defined separately. As discussed in Section 6.1, p_{uT} is defined as the contact stress, from which the severe wear of the tribological system occurs with a sliding length of 1 m. The $\mathrm{p_{uT}}$ value are summarized in Table 17.

Table 17 Value of $\mathbf{p_{uT}}$ of the four tested tribological system

No. of tribological system	$p_{uT}\ [MPa]$
1	880
2	910
3	550
4	518

6.3 The estimated WRC of tested systems – median

The median estimation follows the procedure of fitting parameters' calculation according to equation (A-4). The estimated WRC for the median of the tested tribological systems 1 - 4 and the goodness of fitting, depicted by Mean Square Error (MSE) are shown in Figure 65. From the fitted curves, some generality in the trend of the models from Basquin, Weibull and Henry can be found. At higher load levels, the gradient of the curve is steep and most data of the WRD are located at the right side of the derived curves, which indicates the tool lives are underestimated. On the contrary, the gradient of the curves of the three fitting models becomes flatter at low load levels. At the lowest load level of the fitting data, most of the data is located on the left side of the derived curve, which implies an overestimated tool life at low load level. For these three models, the life spans are sensible to contact stress at higher load levels, but insensible at lower load levels.

Compared to the three other models, the model of Hwang and Han shows a different behavior. The gradient of the curves is flatter at higher load levels and steeper at lower load levels. The data of each load level is relatively evenly distributed on both sides of the fitted curve, which means that the Hwang and Han model shows better predictability of tool life span for all load levels. Regarding the calculated MSEs, it also confirms that the model "Hwang and Han" has the least MSE in comparison to the other three models for all four tribological systems.

Regarding the validity for tribological systems with high and low wear resistance, it can be seen that the model "Hwang and Han" is compatible for estimating the average tool life span of tribological systems generally for uncoated tools. Since the validity of the models can be approved under different experimental conditions for different tribological systems, the robustness of the models can be approved [SHA19].

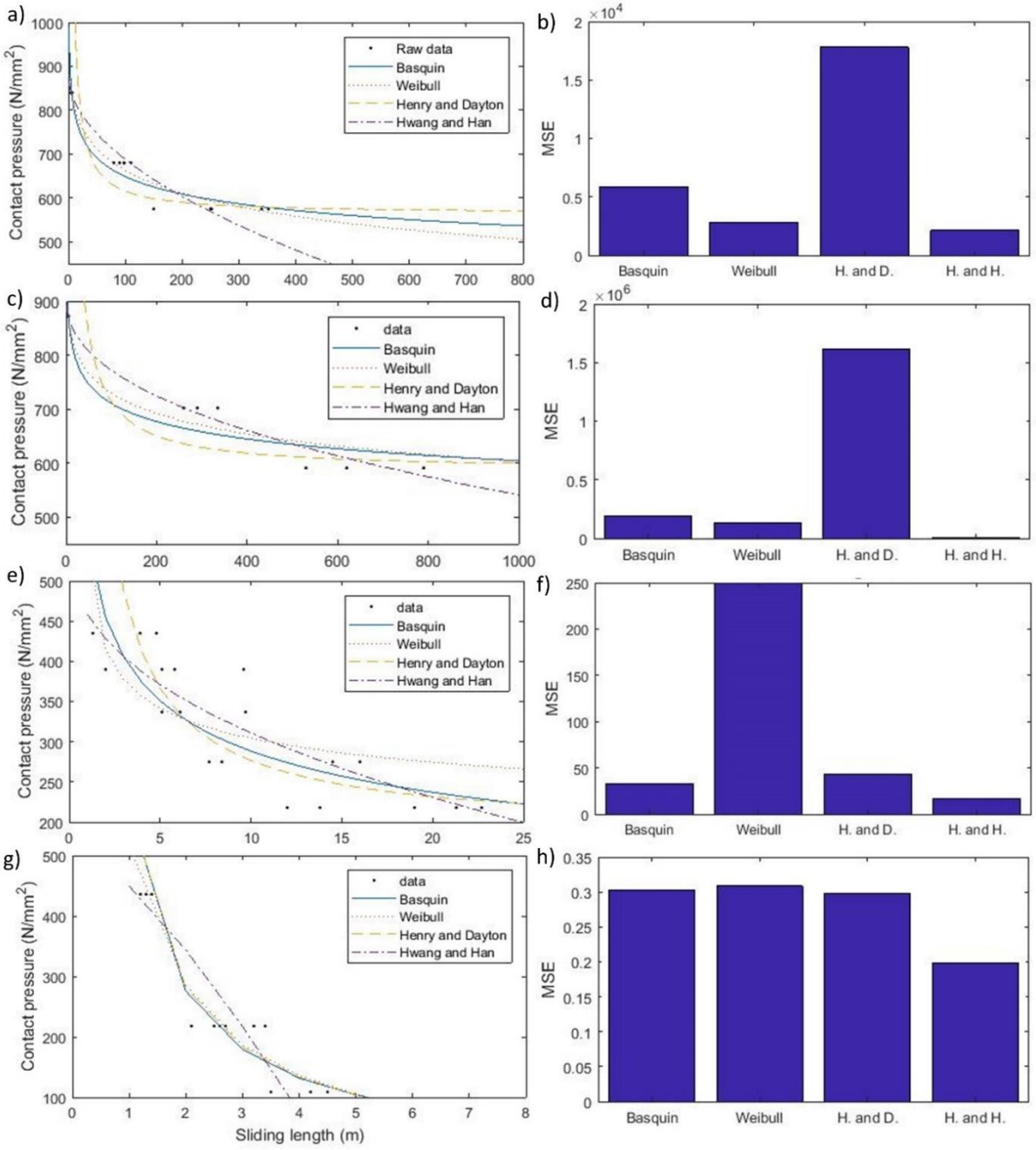

Figure 65 The results of curve fitting and the goodness of fitting for different fitting models a) b) tribological system No. 1; c) d) tribological system No. 2; e) f) tribological system No. 3; g) h) tribological system No. 4 (Abbreviation: H. and D. – Henry and Dayton; H. and H. – Hwang and Han, Source: [WU22])

6.4 Quantile calculation for uncertainty estimation

The results in section 6.3 show that the median estimation is suitable for tribological systems with low variation of the life span at both higher and lower load levels. However, in practice, the variation of the life spans is load-dependent [GRO19a].

In Appendix 2, the equation for quantile estimation is described. The difference between the median and the quantile estimation is the conversion of the fitting parameter according to equation A-5.

In this section, the curves with confidence levels 95%, 80%, 70% and the median (quantile 5%, 20%, 30% and 50%) are plotted for all four tested tribological systems according to the three models with the best goodness of fit (see Figure 65). The results are illustrated in Figure 66.

After the derivation of the quantile, it is possible to determine the uncertainties of the estimation, especially for lower load levels. It can be found that most failures can be pre-estimated through the application of the curve with a confidence level of 95 %. Only limited number of exceptions for several test points which are located on the left side of the estimated curve, can be identified (see Figure 66a and d).

The main difference among models is the life span at lower load levels. For example, for tribological system No.1 (Figure 66a), the lowest load level of the test data is 580 MPa, but the estimation for an even lower load level like 500 MPa reveals large deviations when different fitting models are applied (For confidence level 95%, “Hwang and Han” estimates 230 m, while the model “Basquin” estimates 800 m). In practice, the effectiveness of the fitting for lower load levels also determines its applicability. Therefore, it is necessary to validate the estimation by additional tests for the life spans at lower load levels.

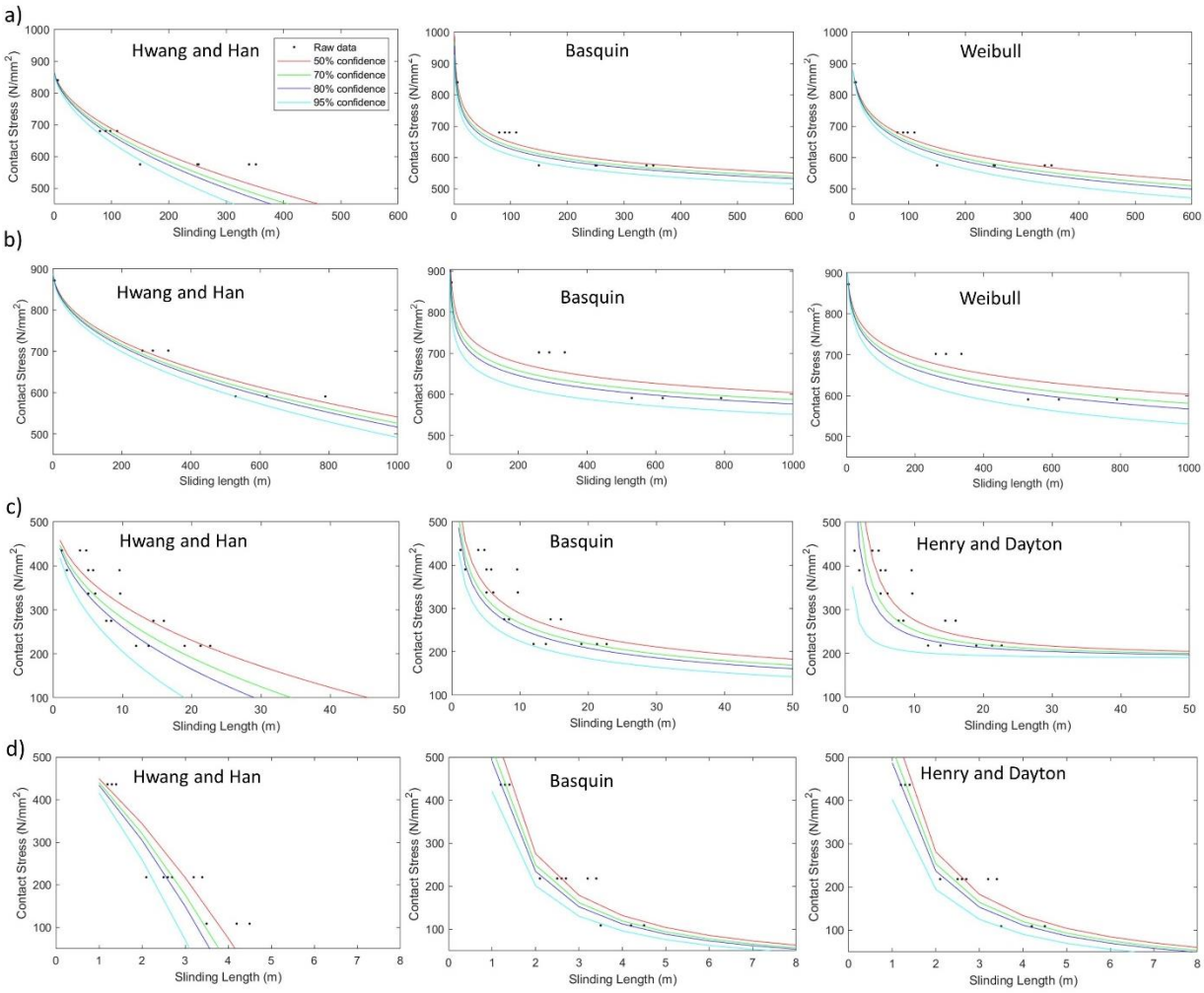

Figure 66 Quantile of different confidence levels of the three best models with goodness of fitting for a) tribological system No.1; b) tribological system No.2; c) tribological system No.3; d) tribological system No.4 (Source: [WU22])

6.5 Validation of the models at lower load levels

For examining the fitting models at lower load levels as well as the load levels other than the tested level, several additional tests are deployed for validation by repeating the strip drawing test. In this section, the tribological system No. 3 is used, since it has the highest data number of all the tribological systems. For characterizing the life span at lower load levels, wear tests are deployed four times at the load 163 MPa (30% to p_{uT}), which is about 75 % of the lowest load level of the fitting data. For further validation, three tests with randomly selected contact stresses are deployed. The test matrix and the resulting life spans are illustrated in Table 18.

Table 18 Test matrix for fitting model validation

Test No.	Contact stress [MPa]	Number of Repetition	Life span [m]	Lubricant
1	163	4	15.1 16.3 33 42.6	PL61 of Zeller Gmelin Amount 1 g/m^2
2	247	1	12.5	
3	312	2	8.9 11.5	

The life spans of the test matrix are illustrated as scattered points in the diagram of estimated WRC in Figure 67. The life spans of Test No. 2 and 3 with intermediate load levels are located on the right side of the curve with 80 % confidence level for all three models. The four life spans for the validation under the lowest contact stress (Test No. 3) show a greater variation, which corresponds to the former research of the authors that the variation of the life span increases with decreasing contact stress.

From the validated results of the other two fitting models, it can be seen that the estimated life spans for the lower load levels are extremely overestimated even for the estimation with 95 % confidence. In comparison, the estimation by the model “Hwang and Han” shows much better performance in estimating the life span under the lower load levels, since all data points are located on the right side of the WRC with 95 % confidence (Figure 67a).

Summarizing the results of sections 6.3 and 6.4, it can be seen that the estimation with the "Hwang and Han" model not only has the highest accuracy of curve fitting compared to the other fitting models, but also a better performance in estimating the service life for even lower load levels. Through quantile calculation with high confidence levels, tool wears for both higher und lower load levels can be predicted.

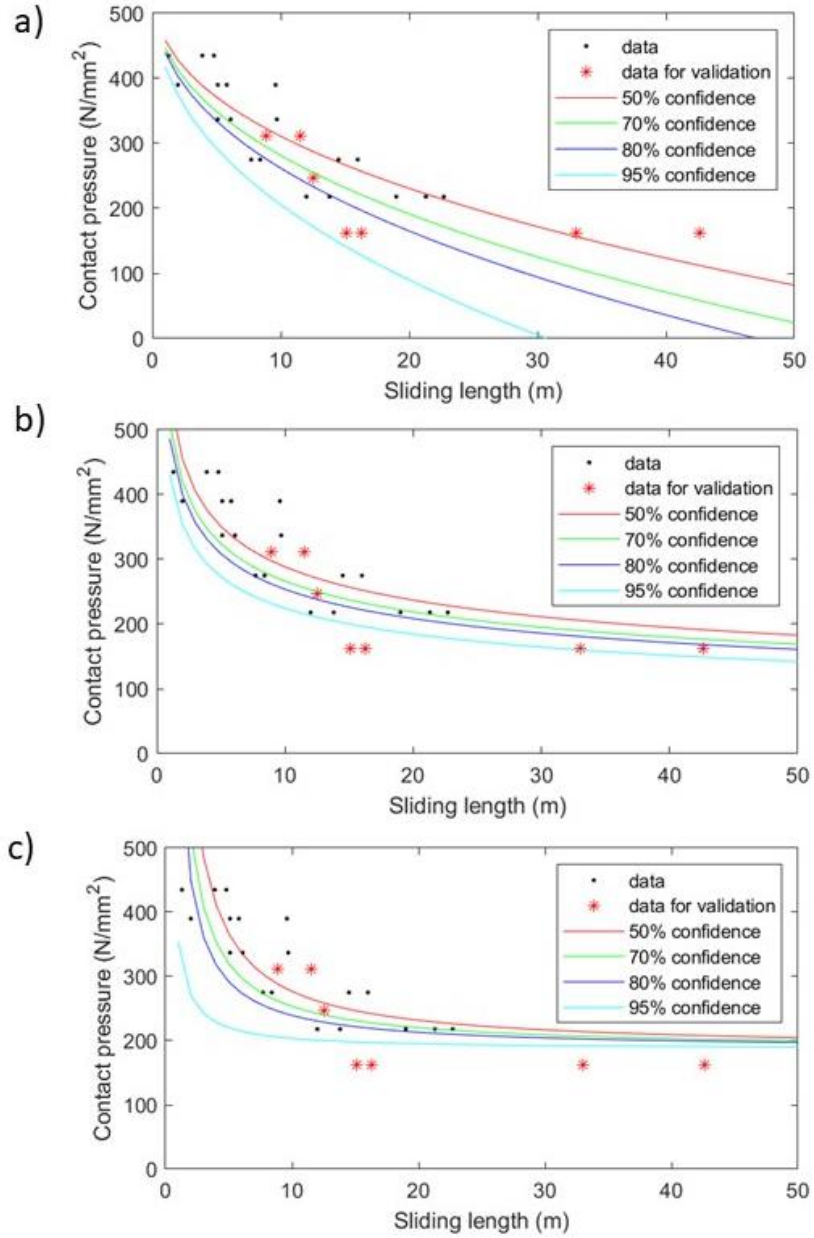

Figure 67 Validation of the models from a) Hwang and Han; b) Basquin; c) Henry and Dayton (Source: [WU22])

6.6 Discussion

6.6.1 Evaluation of the models in different circumstances of application

In the former sections, the applicability of the models was evaluated merely by calculating the MSE of all data. However, it is necessary to consider the models'

performances in industrial applications, in which the load levels vary in different sheet metal forming processes. Therefore, the goodness of fit should be evaluated for both higher and lower load levels.

The tribological system No. 3 is used as an example to show how the required parameters are obtained. Firstly, the MSEs are calculated separately for the highest load level (435 MPa) and the lowest load levels (218 MPa) of the tested data (see Figure 66b). The results of the parameter calculation are shown in Figure 68.

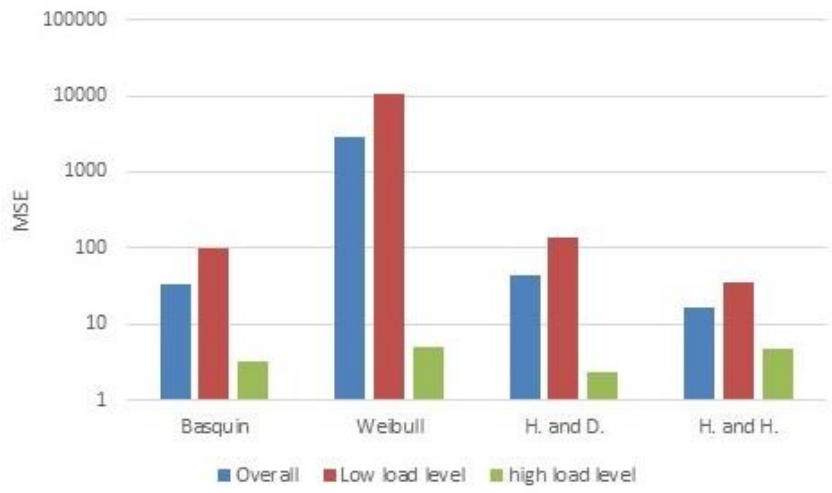

Figure 68 MSE for different load levels (Tribological system 3) (Source: [WU22])

Combining the goodness of fit at both low and high load levels, it can be seen that the fitting model “Hwang and Han” shows the best agreement in fitting the life spans at both high and low load levels.

6.6.2 Interpretation of the results

In the former sections, it is found that the model “Hwang and Han” is suitable for the life span estimation of uncoated tools. This model was originally derived for the fatigue strength estimation of composite materials with glass fiber [HWA86]. It seems that the fatigue strength of composite material and the wear resistance of the uncoated tools are two different kind of problems. However, it is well worth considering why the "Hwang and Han" model can be used to estimate the wear resistance of the uncoated tools. The similarities between fatigue strength and wear resistance will be discussed in this section.

Firstly, regarding the damage development, both the fatigue damage [SHA19] of the composite material and the wear development show three phases (see Figure 69a and e). In the first phase, the running-in phase, the degradation of the composite material, which is characterized by the “fatigue modulus”, shows a regressive development until saturation. After the saturation, it experiences a long-term “stationary phase” until an abrupt “failure” [SHA19]. Comparatively, wear development shows a similar trend according to Habig [HAB80], who proposed the typical wear development curve for metals. According to the typical wear development proposed in section 2.3.1, the obtained wear development shows a similar development with three phases. Therefore, the damage development of fatigue strength and wear is the first similarity.

Secondly, in terms of the damage mechanisms of each phase, several similarities can also be found. In the first phase of the fatigue damage of composite material, cracks are initiated on the whole matrix of the composite material (see Figure 69b) [SHA19], while tiny adhesive pick-ups emerge on the tool surface, which is shown in Figure 69f. These cracks within the composite materials, as well as tiny adhesion marks, grow in the stationary phase, the second phase of the damage development (see Figure 69g). According to the damage development of material under cyclic load, the length of cracks can not only be extended, but also be suppressed [CLA10]. This leads to a relative slow development in the stationary phase. Similarly, in the wear development, the roughness asperities of the adhesion marks can grow but can also be flattened, which also provokes a lower gradient. However, the overall size of wear marks tends to increase instead of being flattened and the wear marks merge gradually to form a severe wear mark (see Figure 69h), which cannot be flattened and therefore is irreversible. After the formation of the merged wear mark, the “failure” of the tool surface occurs. In comparison, in the development of fatigue failure of composite materials, the crack propagates to a certain extent and leads to a fracture of the material (see Figure 69c and d).

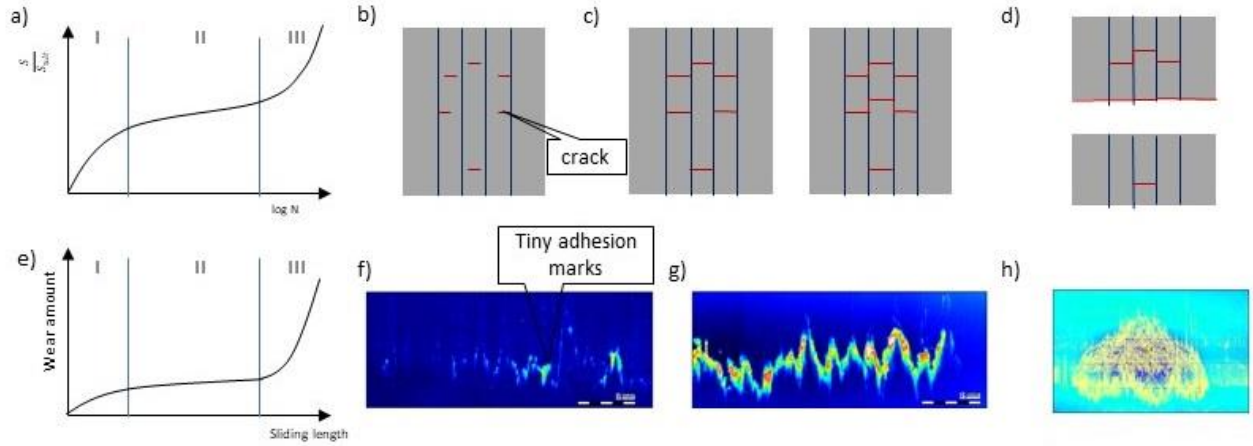

Figure 69 a) Fatigue development of composite material and its failure mechanism at b) running-in, c) steady-state and d) fracture phase [REI12]; e) typical wear development according to Habig and the wear mechanism at f) running-in, g) steady-state and h) severe wear phase (Source: [WU22])

Another question is, why the fitting model for composite materials such as “Hwang and Han” [HWA86] instead of the models for single steels (such as “Basquin” [BAS10]) is more suitable to the life span estimation of the uncoated tools investigated in this paper. This can be explained by the number of cracks in the initiating phase of failure development between composite and single material. Within the composite material, a larger number of cracks initiates during the running-in phase [REI12], while the fatigue damage of metal starts from a single crack initiated within the material [CLA10]. Similar to the composite material, the tiny wear marks initiated during the “running-in” phase occur at several loci, which is also similar to the crack initiation within the composite material.

After analyzing the failure development and failure mechanism of composite fatigue failure and wear in composite materials, several similarities have been observed. These evidences of physical similarities support the applicability of the model “Hwang and Han” for the life span estimation for uncoated tools.

6.7 Discussion of minimal number of tests for wear estimation

Another objective of wear estimation by the WRC derivation is that the estimation should be satisfactory with a limited number of wear tests. Therefore, the influence of the number of tests and the selected load levels on the goodness of curve fitting will be discussed.

As an example, the tribological system No. 3 with 19 data points at five load levels is used. Firstly, it will be examined, if it is possible to estimate the tool lives for lower load levels through the test data of higher load levels. Therefore, the 19 data points are split into two parts, the data for fitting and the data for validation. The test matrix is shown in Table 19.

Table 19 1st Attempts for influence for load levels on fitting quality

Attempts	Load levels for fitting	Load level(s) for validation
1	1, 2	3, 4, 5
2	1, 2 ,3	4, 5
3	1, 2, 3, 4	5

The models with the best performance “Hwang and Han” with 50 % confidence are used for this investigation. Three tests are made. In the first attempt, the results with the highest loading level 1 and 2 serve as the fitting data, and the fitting parameters are defined according to the fitting model in equation (A-4).

The estimated life spans for load levels 3, 4 and 5 are calculated and summarized in Table 20. The same procedure is repeated for the 2nd and 3rd experiment according to Table 19. In Table 20, the estimated load levels at the whole load levels with 19 data points are also included as a reference. The relative errors of attempts 1 - 3 with respect to the reference (attempt 4) are also listed in Table 20 in brackets.

Table 20 Estimated life span and its relative error with higher load levels as reference to the estimated life span with whole load levels

Attempts	Estimated life span (m) and its (relative errors)		
	Load level 3	Load level 4	Load level 5
1	205.7 (2610%)	2197 (15604%)	12593 (57219%)
2	-	58.04 (315%)	137.3 (525%)
3	-	-	31.24 (42.2%)
4 (reference)	7.59	13.99	21.97

The results in Table 20 indicate that the errors for attempts 1 and 2 are high and therefore, this approach is not applicable for life span estimation. In attempt 1, for example, the estimation of load level 3 has already an error with factor 26, while the estimation for load level 5 has an error with factor 572. For the 3rd attempt, the error is decreasing to an error of 42 %. Nevertheless, it is still unacceptably high and the estimated life spans are overestimated with all the experiments. It can be stated that the estimation for lower load levels through fitting data from higher load levels results in poor quality. Therefore, these experiments are not suitable for WRC estimation for all load levels in practical application.

In the following, three more tests are deployed. In these tests, the number of load levels corresponds to the attempts 1 - 3 (see Table 19). The only difference is that the data of load level 5 always serve as fitting data. The attempts 5-7 are summarized in Table 21.

Table 21 2nd Attempts for influence for load levels on fitting quality

Attempts	Load levels for fitting	Load level(s) for validation
5	1, 5	2, 3, 4
6	1, 2, 5	3, 4
7	1, 2, 3, 5	4

Similar to test 1 - 3, the model „Hwang and Han“ with 50 % confidence is used for curve fitting. The estimated life span and its relative errors are illustrated in Table 22.

Table 22 Estimated life span and its relative error with higher load levels as reference to the estimated life span with whole load levels

Attempts	Estimated life span (m) and its (relative errors)		
	Load level 2	Load level 3	Load level 4
1	3.91 (23.5%)	8.82 (16.2%)	18.26 (30.5%)
2	-	8.42 (10.9%)	15.27 (9.1%)
3	-	-	14.89 (6.4%)
4 (reference)	3.82	7.59	13.99

From the results, it can be seen that the estimation quality of experiments 5 - 7 has improved dramatically compared to attempts 1-3 after implementing of load level 5 for curve fitting. Even the lowest number of load levels for fitting data (attempt 5) offers a better quality of fitting than the fitting data of four load levels (attempt 3) without the participation of load level 5. When the number of load levels for curve fitting increases to three (attempt 6), the relative error decreases to around 10 %. Therefore, it can be concluded that the pre-requisite of a high-quality fitting for WRC is the consideration of the wear data of both high and low load levels. By using the pre-selected models in Table 15, it is hard to obtain a satisfactory estimation of the whole load levels by using only the first two load levels with the shortest test duration of the strip drawing test. The wear data of lower load level is necessary for a more accurate estimation.

6.8 Case study: wear resistance of different lubricants

In the industrial manufacturing, lubrication is a key factor for increasing tool life spans. In this section, a case study about the WRC characterization for different lubricants is described. This investigation was deployed in Technical University of Denmark.

In this case study, the derived WRC of stainless steel X5CrNi18-10 (Tribological system No.3 of Figure 66) is used as the reference tribological system. The lubricant Multidraw PL61 of Zeller Gmelin was used. Due to its relative low viscosity (58 mm²/s), it does not fit the actual industrial application for stainless steel forming and the life span is very short (see Figure 65c). In this study, six different lubricants specialized for stainless steel forming of two manufacturers are used. The lubricants and their viscosities of this study are summarized in Table 23.

Table 23 Summary of the used lubricants of stainless steels

Name of Lubricant	Viscosity 40°C [mm²/s]	Manufacturer
Multidrawi PL61 (reference)	58	Zeller Gmelin
Rhenus SF125	125	Rhenus
Rhenus SU 200A	200	
Rhenus SU 500A	500	
CLF 130 HL	130	Raziol Zibulla & Sohn
CLF 250 S-KR	250	
CLF 400 E	400	

The stainless steel X5CrNi18-10 is used as sheet material and the cold working steel X153CrMoV12 as tool material in this investigation. The tests are deployed as strip reduction test (SRT), which simulates the load condition of an ironing and deep drawing process. The test load is set through adjusting the sheet reduction. The used lubricants have two levels of viscosity. The lubricants with the lowest level of viscocity, Rhenus SF 125 and CLF 130 HL, are used for deep drawing of stainless steel. The reductions of this test are set as 2%, 4% and 6%. The lubricants of middle level, Rhenus SU 200A and CLF 250 S-KR and those of the highest level, Rhenus SU 500A and CLF 400E are used for ironing processes with severe tribological conditions caused by high thickness reduction. The reductions for strip reduction tests are set as 4 %, 6 %, 10 %, 12 % and 16 %. During the strip reduction test, the sheet metals are lubricated

manually with a huge amount of lubricant (> 2 g/m^2). The drawing speed is 100 mm/s and the stroke length 100 mm, which is in agreement with the approach with the test of PtU (see Section 6.2). The procedure of contact stress calculation corresponds to the approach of Üstünyagiz [ÜST17]. The test matrix and the calculated contact stress are summarized in Table 24.

Table 24 Test matrix: Wear resistance of lubricants

Viscocity levels	Lubricants		Reduction [%]		
			Contact stress [MPa]		
Low	Rhenus SF 125	CLF 130 HL	2	4	6
			564	643	740
Middle	Rhenus SU 200A	CLF 250 S-KR	4	6	12
			643	740	787
High	Rhenus SU 500A	CLF 400E	10	12	16
			765	787	867

According to section 6.7, three load levels with each three tests are necessary for a satisfactory WRC derivation. For the tests with each viscosity, nine tests in all the three levels are deployed for Rhenus lubricants and the WRCs for Rhenus lubricants are determined. Comparatively, three tests under two load levels are carried out with lubricants of the series CLF. The wear development is determined through measuring the drawing force at a test stand at DTU. When the force signal has a sudden increase, it can be regarded as the start of severe wear, according to [ÜST17].

Figure 70 shows the WRD of Rhenus lubricants. Even at the severe load condition over 500 MPa, the wear resistance is improved compared to the reference lubricant PL61. Probably, the higher viscosity of the lubricant is the reason for the improvement.

For a better qualification of the lubricant influence of load-dependent wear resistance, the WRC is derived from the raw data of WRD, which are shown in Figure 71. The best model “Hwang and Han” for uncoated tools is used for curve

fitting. In this diagram, not only the curves of median but also those of with 95% confidence, are plotted. The area between the median and the 95 % curve can be regarded as the wear resistance characteristic field of the lubricant. With the help of these characteristic field, it can be found that the wear resistance of tools is improved significantly when a lubricant with a viscosity of 200 mm²/s is applied.

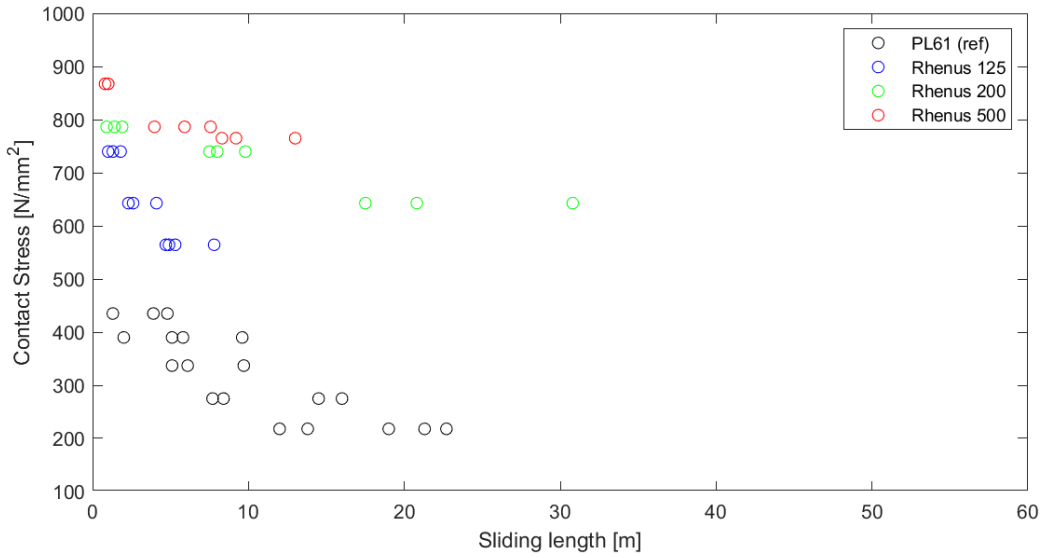

Figure 70 WRD of lubricant series Rhenus (Lubricant PL 61 as reference)

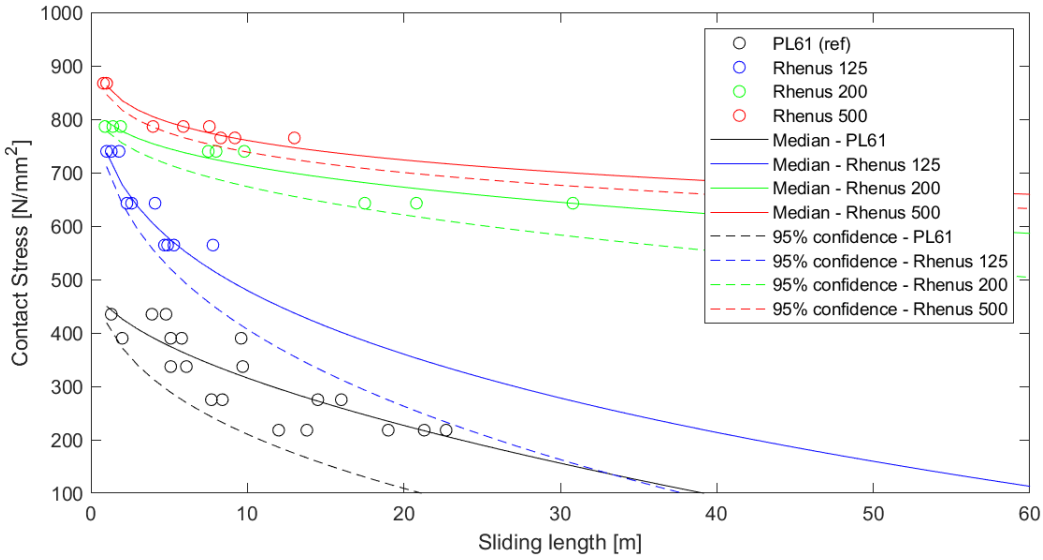

Figure 71 WRC (Characteristic field) of lubricant series Rhenus (Lubricant PL 61 as reference)

After the WRC determination, four characteristic fields for four lubricants with different viscosities are derived. These four WRCs can be used as reference for wear resistance characterization for different viscosity levels.

Figure 72 shows an example of application. In this diagram, the life spans of the CLF series lubricants are demonstrated in the diagram. Compared to the Rhenus series, all the points of CLF 400E are located on the median WRC of the Rhenus series, which indicates an identical wear resistance between these two lubricants for stainless steel ironing. The points of other two variants, the CLF 250 S-KR and CLF 130 HL, are located at the left side of the median WRC of the Rhenus series, which implies a poorer performance than the reference lubricant.

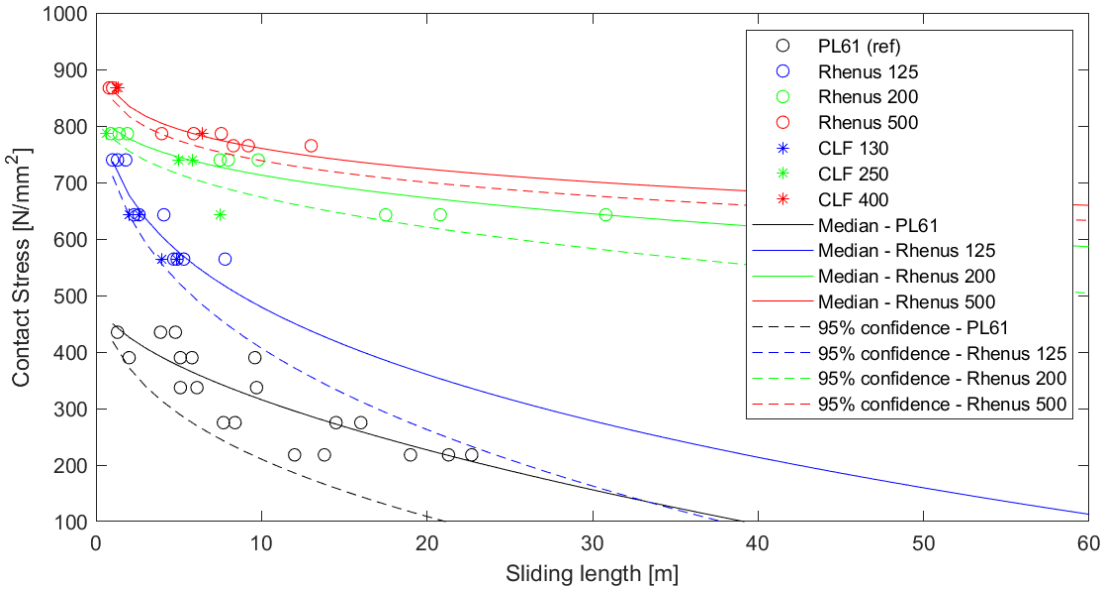

Figure 72 A practical example for wear resistance analysis based on reference WRCs

6.9 Conclusions

In this chapter, the process for WRC estimation is described. Four basic models for S-N curve estimation are used. Not only the median but also the curves for different quantiles are calculated. Of all the models, the model „Hwang and Han“ is most suitable for the WRC estimation for different kinds of tribological systems with different wear resistance through the analysis of the mean square errors (MSEs). Regarding the fitting functionality for higher and lower load levels

separately, the fitting through the model „Hwang and Han“ also has a good fitting accuracy at both higher and lower load levels. Therefore, the model for fatigue life estimation for composite material “Hwang and Han” serves for the life span analysis of uncoated tools of forming processes. The similarities in the mechanisms and development between composite fatigue life and tool wear life are also discussed in this paper to support this finding.

Since wear tests are very time consuming, the possibility of life span estimation at lower load levels using data at higher load levels with short-term tests is also discussed in this chapter. It is concluded that the accuracy of fits for predicting wear behavior at lower load levels based on data from only the higher load levels is unsatisfactory. Thus, this strategy for life span estimation is not applicable. For a satisfactory estimation of the WRC the prediction of wear data for higher and lower life spans is a pre-requisite.

The approach described in this section offers a new aspect for life span estimation in sheet metal forming processes. With empirical data on the life span of the actual forming process corresponding to the lower load level, and the wear data in model tests at higher load levels such as strip drawing tests, it is possible to estimate the life spans and its uncertainties by applying estimation models like „Hwang and Han“ for all load levels. As a result, through the estimation process of the WRC, the planning of tool maintenance can be optimized.

The case study described in section 6.8 shows an example for WRC application for different lubricants. After the determination of typical WRCs with different viscosity levels of lubricants, the performance of deviating lubricants (for example deviating additives or base oil) can be determined through a limited number of tests. This approach will be discussed further in section 7.7.

The derived WRCs in this chapter serve for the life span estimation for tools without coating. In actual forming processes, tools with coating are widely used. The procedure for life span estimation for tools in actual forming processes is described in the following chapter with two case studies.

7 Case study: Life span estimation for industrial forming processes

In previous sections, methods for inline wear detection through thermoelectric current (Chapter 4) and life span assessment through wear resistance analysis (Chapter 6) are described. These two approaches are the main foundations for effective control of wear in sheet metal forming. In this section, two case studies from actual forming processes are presented for these two approaches applied to them.

The example forming processes are ironing process and sheet-bulk forming (SBF) of a gear. Contrary to the processes described in the former chapters, the tools of the two actual processes are coated. The behavior of wear detection through thermoelectric current for tools with coating is discussed in this chapter. Moreover, the wear resistance curves (WRC) for tools with coatings will be estimated in this section and the difference between the WRCs for tools with and without coating is discussed.

7.1 Procedure of life span estimation

Figure 73 shows the procedure for life span estimation for an actual ironing process. According to section 6.7, for a satisfactory WRC estimation, three load levels are necessary. Firstly, the actual process is analyzed. Through numerical simulation, the contact stress in the process is calculated. The life spans found in the actual forming process are also documented. Existing data relating to the contact stress and life spans supply data-points for the WRD at low load levels. To estimate the WRC, wear data for two higher load levels are found through strip reduction testing. Before utilizing the strip reduction test, the tools for the test should be designed. The wear data for higher load levels is also summarized in the WRD. By extrapolation through models mentioned in 6.2, the WRC for the actual process is found.

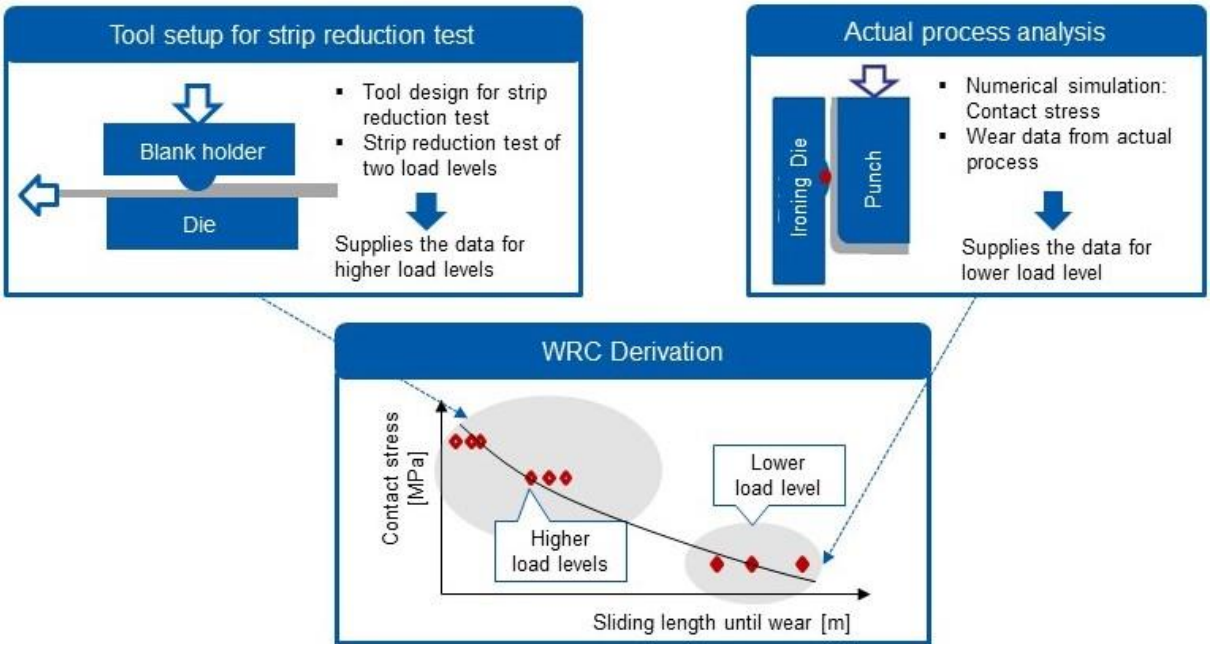

Figure 73 Procedure of life span estimation for an industrial forming process (Cup ironing as example)

7.2 Actual process analysis

7.2.1 Ironing process

The combined deep-drawing and ironing process serves for the manufacturing of a “Cup” part. It consists of three deep drawing processes and two ironing processes. The 2nd ironing process has the highest risk of wear for two reasons: firstly, the sheet thickness reduction in ironing is 10% which is the highest of all the process steps; secondly, the lubrication conditions in the 2nd ironing process are more severe. Similar to the industrial process, the initial lubricant amount is set to 4.5 g/m^2. According to the industrial partner, the lubricant is scrapped and the remaining lubricant before the 2nd ironing process is around 1 g/m^2.

The process parameters of the ironing process are summarized in Table 25.

Table 25 Process parameters of the combined drawing and ironing process

Sheet metal material	HSM760 (988) from ThyssenKrupp
Tool material	HWS Premium from STM
Coating	Duplex-Variantic 1000

	(Manufacturer: Eifeler)
Lubricant	Dionol ST V1842 (Manufacturer: MKU)
Sheet metal thickness [mm]	2.1
Sliding length per stroke [mm]	0.3

The 2nd ironing process consists of two ironing levels, the first of which involves a reduction of 10% and the second of which involves a reduction of 5%. To calculate the contact stress, a numerical simulation is deployed in Simufact 16. The parameters used in the simulation are summarized in Table 26

Table 26 Parameters for simulation: ironing process

Mesh type	Tool: Ringmesh Sheet: sheetmesh
Element size [mm]	0.7
Punch velocity [mm/s]	100
Coefficient of friction [-]	0.08
Initial die temperature [℃]	92
Initial temperature of punch and sheet [℃]	20
Young’s module [GPa]	210
Tool hardness	60 HRC
Poisson's ratio	0.3

The initial temperature of the die is measured by a thermal camera. It corresponds to the stable die temperature at steady state conditions. The coefficient of friction is determined through strip drawing tests according to VDA-Standard 230/213.

Simulation results are shown in Figure 74. It can be found that the contact stress during the first level of ironing (Ring 1) is the highest with an average contact stress of 1392 MPa, while the average contact stress of Ring 2 is 1115 MPa.

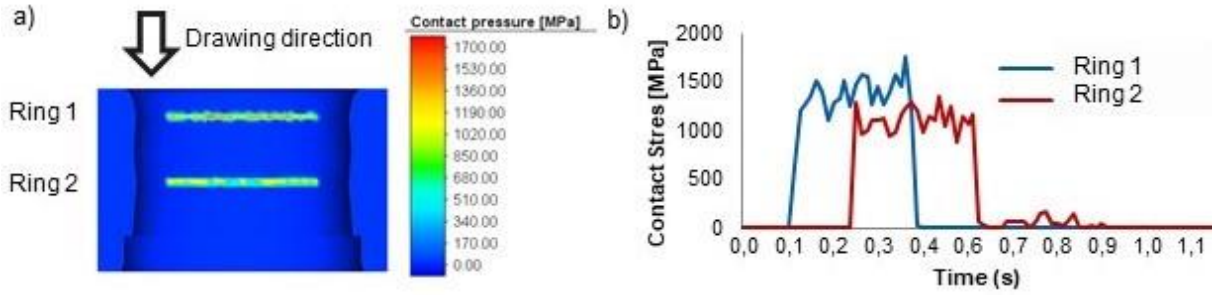

Figure 74 a) Illustration of contact stress evolution; b) contact stress within a stroke of production

7.2.2 SBF of gears

SBF of gears is an important process in manufacturing of clutch housings for automobiles (Figure 75). Sheet metal with a thickness of 5 mm is first blanked and drawn to form a cup. Subsequently, the gear-shaped contour is formed using a gear-shaped punch.

During sheet-bulk forming of gears, the work piece has a large local forming strain, which leads to large contact stresses at the tooth area. This high contact stress causes localized premature wear on the tool edges. In most circumstances, the dominating wear mechanism leads to fracture of the coating. This fracture degrades the accuracy of the teeth and leads to the occurrence of chips in the production processes. Since fracture occurs abruptly and is not easy to predict, tool life estimation is also useful for SBF of gear.

Figure 75 Left: clutch housing; right: wear mark of the tooth (Source: ZF Friedrichshafen AG)

The process description of SBF of the gear are summarized in Table 27.

Table 27 Process description: SBF of gear

Sheet metal material	S420MC
Tool material	CPOH plus
Coating	Duplex-Variantic from Eifeler
Lubricant	DRAWLUB S13/20 (1 g/m^2)
Sheet metal thickness [mm]	5
Sliding velocity of the punch [mm/s]	43
Sliding length of a stroke [mm]	43

Numerical simulation was used to illustrate the evolution of contact stresses. The result is shown in Figure 76. It can be found, from the stress distribution, that the maximal contact stress is located at the front of the tooth, where the punch has direct contact with the sheet metal. However, the front of the tooth geometry does not experience the largest wear in the actual process. Therefore, the distribution of contact stresses on the tooth edge are investigated in this study.

Along the tooth edge, five positions with a spacing of 5 mm are selected and the contact stress distribution across a full stroke is plotted (Figure 76a and b). The contact stress along the tooth edge is found to be position-dependent. The contact stress and the contact length during a stroke vary significantly along the tooth edge. The highest contact stress is located at Pos. 4, at the top half of the tooth edge. However, the contact length found in this position is only 40% of the whole sliding length. Pos. 2 and Pos. 3 have lower contact stresses but a higher contact length over a stroke compared to Pos.4. Figure 76c shows the calculated wear according to Archard wear model with the wear coefficient k=1×10^{-9}. The critical position for wear occurrence in this process is clearly located at Pos. 3, which is at the middle of the tooth edge. The average contact stress is 1166 MPa and the contact length is 70% of the whole sliding length over a full stroke (30 mm).

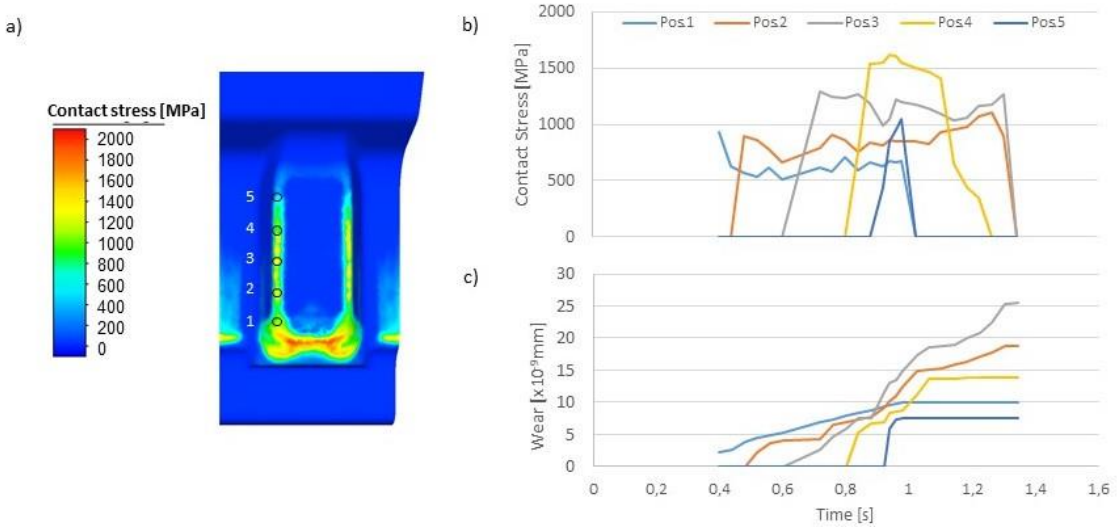

Figure 76 Process simulation of sheet bulk forming of gear a) Contact stress distribution over a single tooth (Source: ZF Friedrichshafen AG); b) Contact stress and c) Wear amount (Archard, $k = 1 \times 10^{-9}$) during a stroke of the forming process

7.3 Test setup for strip drawing tests

The analysis of the ironing process serves for the determination of the contact stress in the actual process. The load level of the process corresponds to the lowest load level of the WRD of this study (see Figure 73).

For WRC estimation, it is necessary to know the life spans under three different load levels. Hence, a life span estimation of the investigated tribological systems at higher load levels is performed using a strip drawing test. Through the adjustment of process parameters such as contact stress and sliding velocity in the strip drawing tests, the load can be set to more severe conditions than those found in the actual forming process.

In this section, the parameters used in strip drawing tests emulating the two investigated actual forming processes are determined. Firstly, tools for the strip drawing tests are designed based on the geometry of the actual forming tools. After manufacturing of the tools, process parameters such as the normal force are determined and the contact stresses at higher load levels are calculated through numerical simulation. The recommended maximal normal force for continuous operation of the combined strip drawing test stand at PtU TU Darmstadt is 36 kN. It is demanded that the resulting contact stress during strip

drawing tests should be at least double that of the contact stress in the actual forming process.

Figure 77a shows the numerical model built to emulate the strip drawing test. The strip drawing test is composed of a blank holder and a die. The die is designed as flat and the blank holder as cylindrical, which simulates the load of “Ring 1” in the actual process (see Figure 76). Through adjusting the normal force F_N, more severe load levels can be achieved. In this case, two levels of normal force, 32 kN (load level 1) and 24 kN (load level 2) are used. For contact stress evaluation, the maximal contact stress of three elements with a contact length of 0.75 mm in each time increment within a stroke are plotted in Figure 77c. The average contact stresses are shown in Figure 77d. It can be found that load level 2 is 1.6 times and load level 1 2.2 times higher than those found in the actual process.

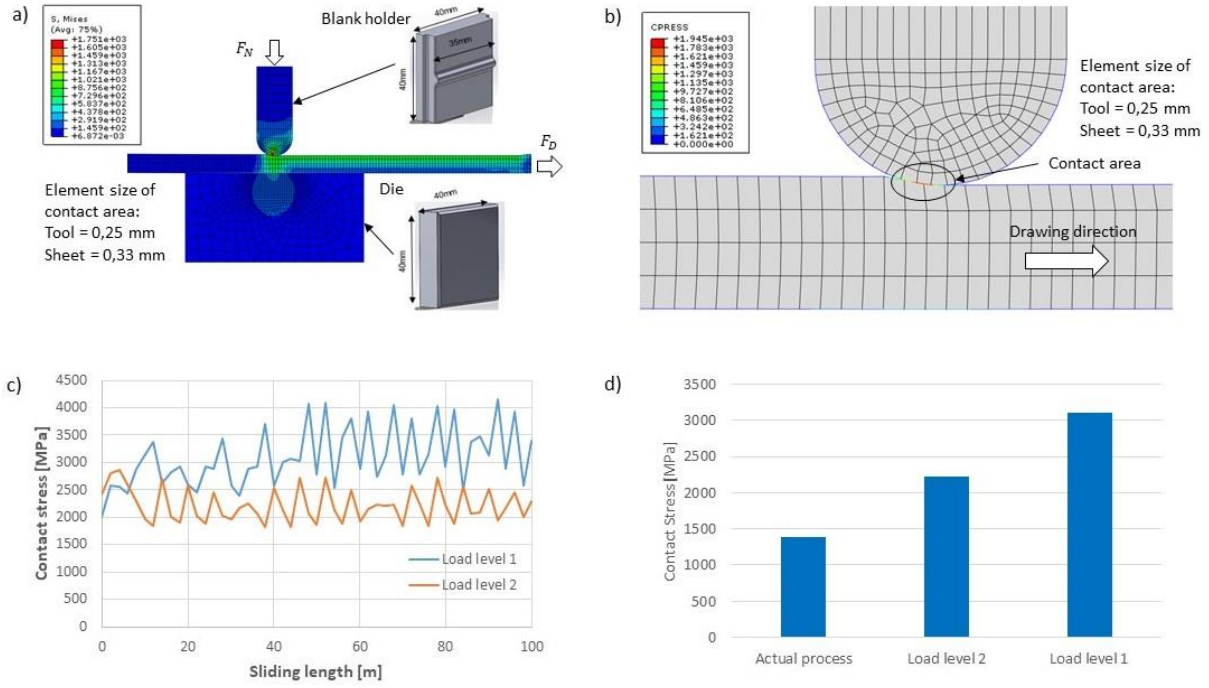

Figure 77 Strip drawing tests for emulating the ironing process: a) Numerical model of the strip drawing test; b) Distribution of contact stress; c) Contact stress evolution within a stroke; d) Three levels of average contact stress

The tool design and contact stress analysis of the SBF of a gear is shown in Figure 78a. The die is also designed as flat, and a bead which simulates the tooth edge is added to the blank holder. After applying the normal force, the

bead penetrates into the sheet as the sheet is drawn. Due to the reduction, severe contact stresses can be produced on the bead. Through changing the normal force, penetration (reduction) into the sheet metal can be controlled. In this case, compared to the ironing process, normal forces of 20 kN (load level 1) and 16 kN (load level 2) are used. The contact stress evolution and the average contact stress are shown in Figure 78c and d. Load level 2 is found to be a factor 1.7 and load level 1 a factor 3 higher than the contact stress found in the actual process.

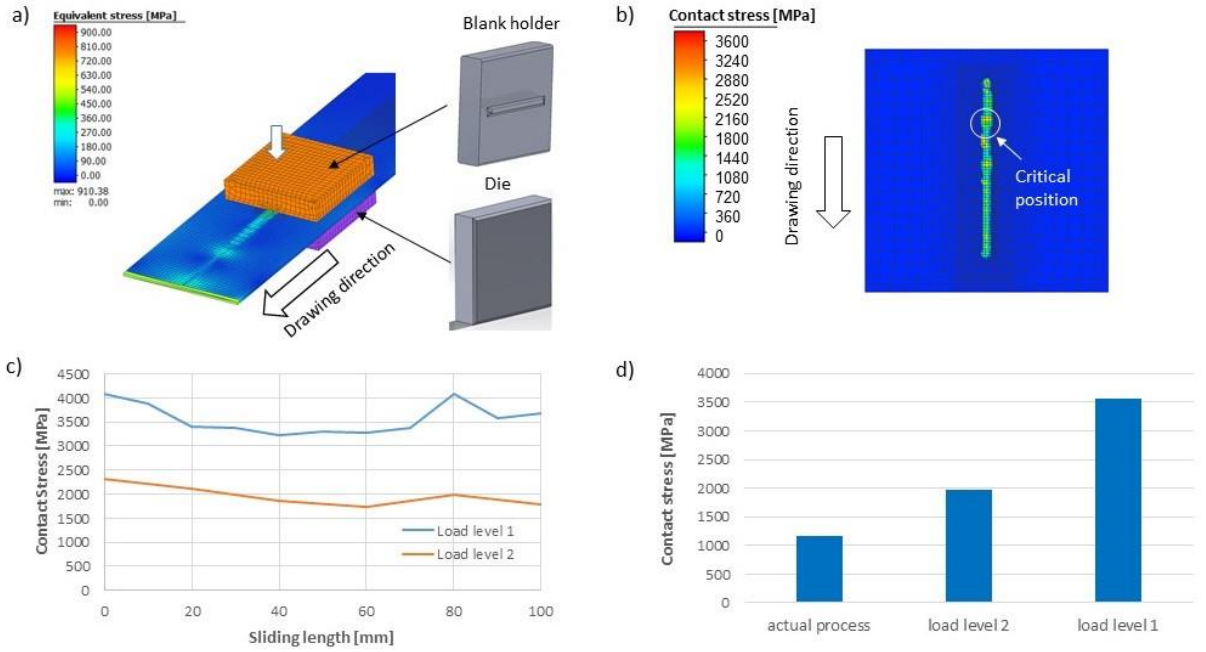

Figure 78 Strip drawing test for sheet-bulk forming of gear: a) Numerical model of the strip drawing test; b) Distribution of contact stresses; c) Contact stress evolution within a stroke; d) Three levels of average contact stress

After the design of experiment described in this section, the test matrix for the following wear tests can be defined.

7.4 Wear test

After the definition of load levels, six strip drawing tests under two load levels for each process are performed to determine the life spans at higher load levels. Thermoelectric measurement is used for wear detection (See Chapter 4) with tool life spans being determined through signal analysis of the thermoelectric current. After the experiment, the wear mechanism and the surface

topographies are characterized through optical measurement with µSurf and SEM microscope of Zeiss. The test matrix of each test series is summarized in Table 28.

Table 28 Test matrix – Wear test for life span estimation at higher load levels

	Ironing process	SBF of gear
Sheet metal material	HSM760	S420MC
Tool material	K490	CPOH plus
Coating	Duplex-Variantic 1000	Duplex Variantic
Lubricant and amount	Dionol ST V1842 (1 g/m^2)	DRAWLUB S13/20 (1 g/m^2)
Load level 1 [MPa]	3102	3568
	Tool number: T1, T2 and T3	
Load level 2 [MPa]	2142	1973
	Tool number: T4, T5 and T6	

Figure 79 shows the evolution of measured thermoelectric current from the model test of the ironing process. After the running-in (first 10 m of sliding length) and steady-state, the measured thermoelectric current of T1, T2, T4 and T5 shows a significant drop of current after 91.7 m, 22.9 m, 84.8 m and 165.7m of sliding length. For the other two tests, T3 and T6, the thermoelectric current increases significantly after a long period of steady-state.

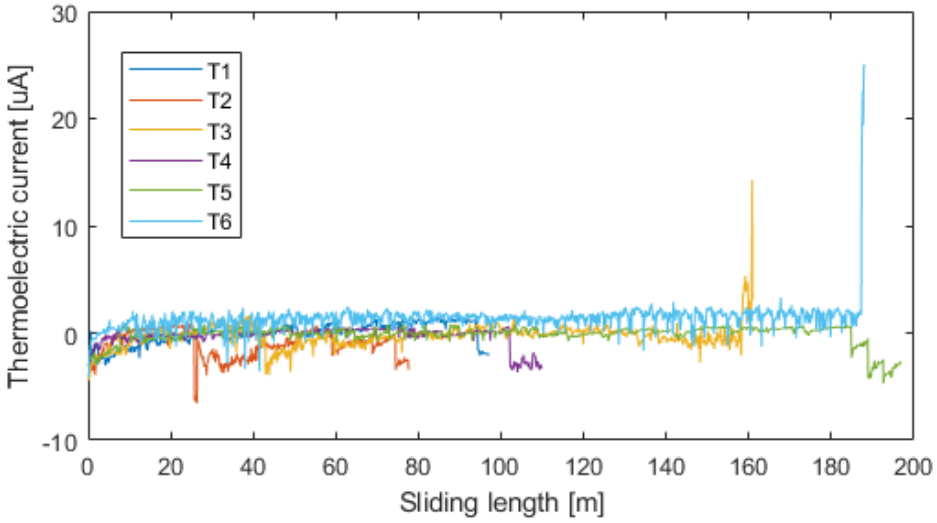

Figure 79 Thermoelectric current: model test of ironing process

The different behavior of measured thermoelectric current among different tests can be explained through the analysis of the dominating wear mechanisms in the tests. In Figure 80, two different wear mechanisms from T1 and T3 are shown as examples. On the surface of T1, a local wear mark can be found. Under a microscope using 20x magnification, the abrasive wear on the coating is obvious. Based on the grooves seen on the coating, which have a height of up to 50 µm according to surface analysis, local galling occurred. The position of galling corresponds to the position of highest contact stresses according to the simulation (see Figure 77b). It is deducted that the galling is caused by the direct contact between the sheet metal and the base material of the tool after breakage of the coating.

In the running-in and steady-state phase, the sheet has direct contact with the tool coating. The Seebeck coefficient of the blank holder (S_{BH} of equation 23) corresponds to the Seebeck coefficient of the coating. After wear occurrence, the direct contact between sheet and base material also leads to a sudden change in the Seebeck coefficient of the contact partners, which causes a sudden decrease in the measured thermoelectric current. Under these circumstances, S_{BH} corresponds to the Seebeck coefficient of the tool base material. Through thermoelectric measurement, a local breakage of the coating can be detected in real-time, and the compatibility of wear detection through thermoelectric measurement at tools with coatings can be proven.

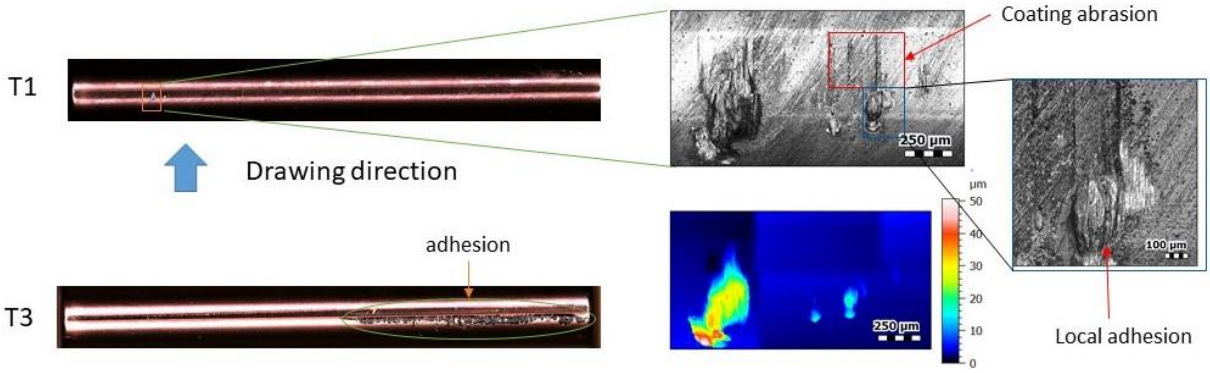

Figure 80 Two different wear mechanisms in model tests for an ironing process

On the contrary, only adhesive wear was found on the surface of T3 and T6. On the surface of these two test tools, no breakage of the coatings was detected. Therefore, the increase of thermoelectric current is merely caused by the temperature increase because of surface roughening due to galling.

Figure 81 illustrates the thermoelectric current in the model test for SBF of a gear. For the highest load level (load level 1), the thermoelectric current starts to decrease within a sliding length of 5 m, which indicates a coating breakage. The tool life span at load level 1 is so short that it occurs during the running-in phase of the wear development.

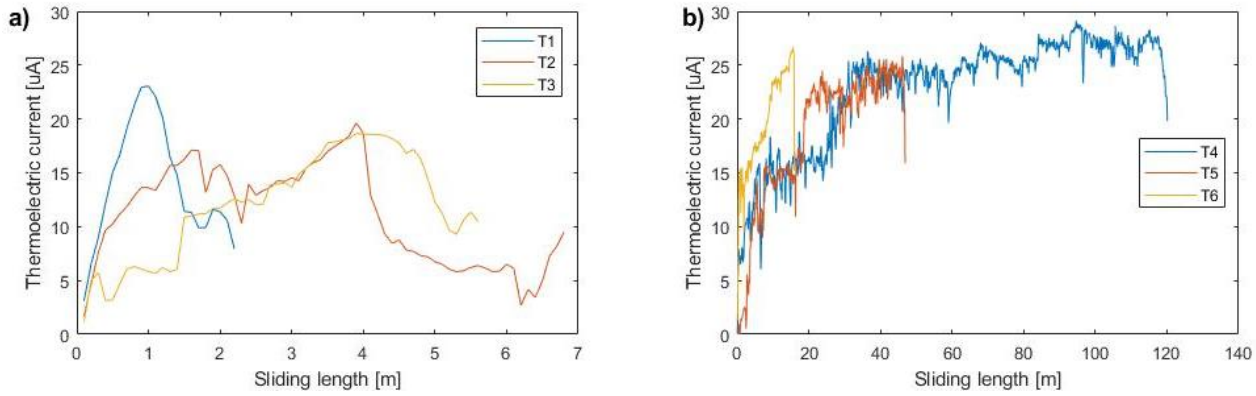

Figure 81 Thermoelectric current: model test for SBF of gear a) Load level 1; b) load level 2

At load level 2, the life spans increase significantly. From the measured thermoelectric current at the tools T4 and T5, a steady-state of wear development can be observed. Similar to load level 1, a sudden decrease of

thermoelectric current can be detected, which indicates coating breakage and the beginning of tool failure.

Figure 82 shows the surface topography of tool T1 after wear has occurred under load level 1. From Pos. 1, the coating breakage can be identified, which explains the sudden decrease of the thermoelectric current due to the abrupt change of the material characteristics of contact partners in the tribological system. Compared to the coating breakage in the ironing process (see Figure 80), the coating fracture of Pos. 1 tends to be caused by fatigue instead of abrasion because of the formation of pitting on the tool surface. Pos. 2 shows severe galling on the surface, which causes the deterioration of the finished parts. It is deduced that severe coating fracture causes the formation of severe galling on the tool surface.

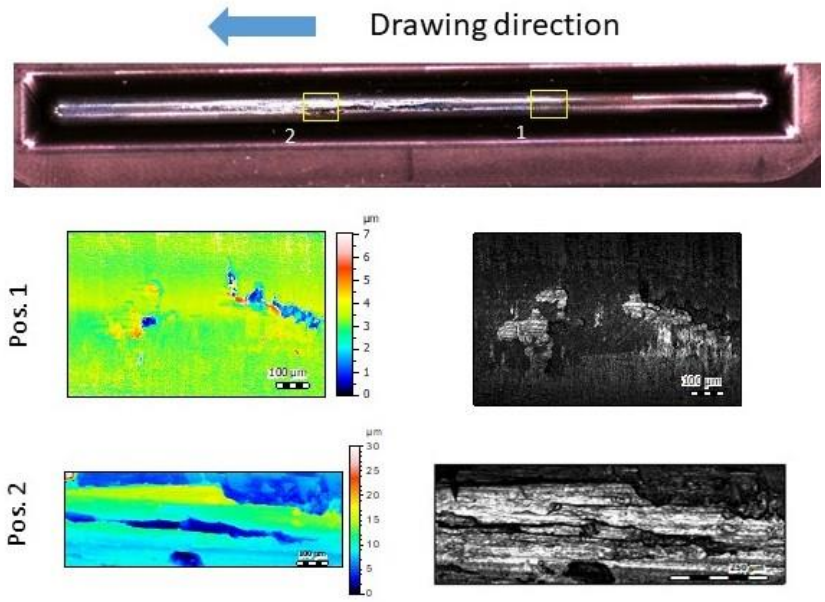

Figure 82 Surface topography after wear occurrence (load level 1: T1)

On tool surfaces used in tests where load level 2 is applied, pitting is also visible, but the size of the pitting is approximately 50% of those at load level 1 (Figure 83). Similarly, comparing the severity of galling on the tool surface (Pos. 2) of load level 1 (see Figure 82), the pickup height of load level 2 is only about one-fourth of load level 1.

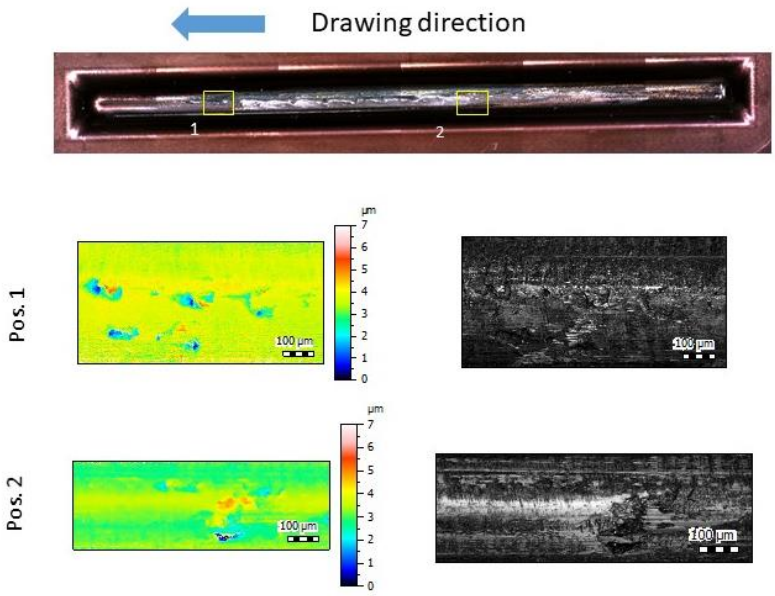

Figure 83 Surface topography after wear occurrence (load level 2: T4)

In summary, the wear mechanism of tools in the model test emulating SBF of gear is mainly the formation of galling due to fatigue of the tool coating. The severity of surface fatigue and galling is load-dependent, which leads to the obvious difference of life spans between load levels.

Combining the two tests, thermoelectric measurement proves an effective method for wear detection. It can detect not only the heat generation due to surface roughening, but also the fatigue fracture or abrasive breakage of coatings. With this method, tool life spans can be determined accurately.

7.5 Wear resistance curve (WRC) of tools with coating

The next step of the investigation is the derivation of the WRC for characterization of the load-dependent wear resistance of the investigated tribological systems.

The life span and the corresponding contact stress of the investigated processes are summarized in Table 29.

Table 29 Summary: contact stresses and life spans of the investigated tribological systems

	Ironing process		Sheet-bulk forming of gear	
Tool number	Contact stress [MPa]	Life span [m]	Contact stress [MPa]	Life span [m]
T1	3102	91.7	3568	1.1
T2	3102	22.9	3568	3.95
T3	3102	142.2	3568	11.2
T4	2142	84.8	1973	15.9
T5	2142	165.7	1973	46.1
T6	2142	168.4	1973	117.7
Actual process	1392	542.7 603 663.3	1166	1204 1565.2 842.8

The data from the industrial forming processes is provided by industrial partners. The life span corresponds to the sliding length until occurrence of wear in the actual process. After summarizing all the data, different fitting models (see Table 15) are used to extrapolate the raw data (WRD) and the quality of the fittings are evaluated by mean square error (MSE) as was done in Chapter 6.

Figure 84 shows the estimated WRC with 50% confidence (median) and the quality of fitting. It is interesting to find that the “Henry and Dayton” fitting model is best for the coated tools, which is different from those without coating (see section 6.3). For coated tools, the “Hwang and Han” model does not match well. In the fatigue life estimation, the “Hwang and Han” model serves well for composite materials, while “Henry and Dayton” serves well for isotropic metals. An interpretation of this difference will be discussed in section 7.6.

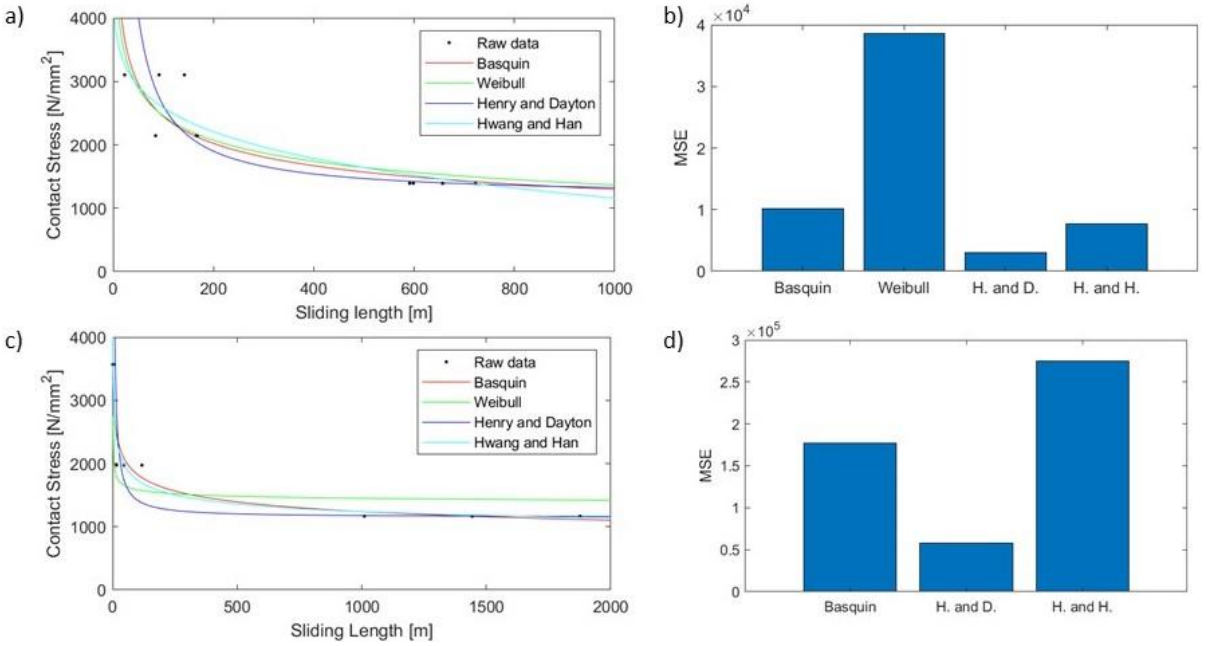

Figure 84 Estimated WRC (Median) based on WRD and the quality of fitting a) b) ironing process; c) d) sheet-bulk forming of gear (The MSE of Weibull is so high, that it is omitted in the diagram.)

Figure 85 shows the WRCs with different confidence levels. Compared to the median (50 % confidence), curves with higher confidence levels move to the left-hand side, indicating a more conservative estimate of the life span. The level of conservativeness should correspond to the actual requirement of a process. For products with higher and stricter requirements with respect to surface quality, higher confidence levels should be selected. For products with a wider tolerance of surface quality, a riskier WRC with lower confidence level can be used for a better utilization of forming tools.

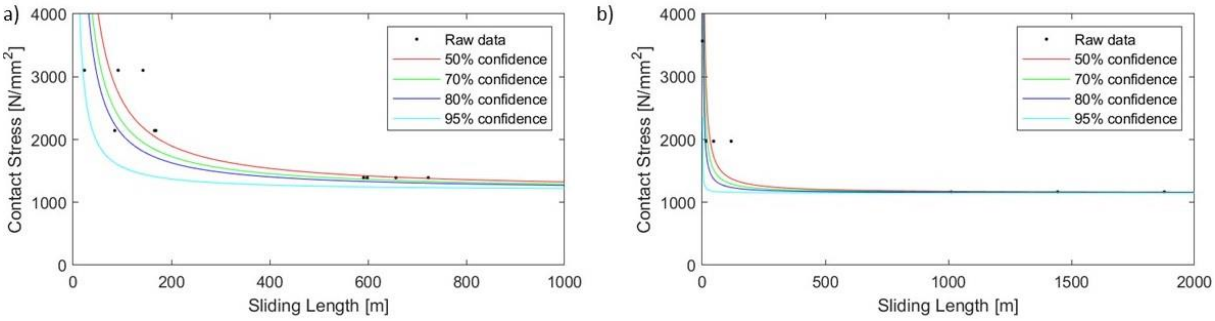

Figure 85 WRCs of a) ironing process; b) sheet-bulk forming of a gear with different confidence levels

7.6 Discussion of the results

Combining the derived WRCs of section 6.3 and 7.5, it is interesting to find that the best fitting models for tools with and without coating are different. For tools without coating, the “Hwang and Han” model, which serves for fatigue life estimation of composite materials, has the best fitting. However, the “Henry and Dayton” model has the best fitting performance for tools with coating.

The reason for the compatibility of the “Henry and Dayton” model for wear resistance estimation of coated tools can firstly be explained through the wear mechanism. The “Henry and Dayton” model is normally used for the life span estimation of typical isotropic metals. For metals, the source of fatigue failure is crack initiation and propagation from local weak spots such as metallurgical defects or cast porosities. In Figure 12, section 2.2.4, the procedure of fatigue wear is described. The pitting or detachment of wear particles from the surface of the material is formed from micro-crack initiation, which is similar to crack initiation in isotropic metals.

The pitting on the tool surface from SBF of gears (Figure 82 and Figure 83) also clearly shows the detachment of wear particles from the coating, which implies a fatigue wear mechanism and explains the similarity between fatigue material failure and failure by wear.

7.7 An example for practical application of wear resistance analysis

In this section, an example for practical application of WRC is described. For SBF of gears, the short life span of tools is a challenge for actual production. The utilization of different kinds of coating is a common way to extend tool life spans. In this investigation, two alternative coatings are tested in strip drawing tests to evaluate their wear resistance with a limited number of tests. The test matrix is shown in Table 30.

Table 30 Test matrix of alternative tribological system (sheet-bulk forming of gear)

Sheet metal material	S420MC	
Tool material	CPOH plus	
Coating	Duplex Variantic 1000	Formatic Pro
Lubricant and amount	DRAWLUB S13/20 (1 g/m^2)	
Load levels	1x. load level 1 (3568.46 MPa) 2x. load level 2 (1973.32 MPa)	

Compared to the original coating, Duplex Variantic, Duplex Variantic 1000 is identical in material composition, except that the thickness is increased from 3 to 9 µm. Formatic Pro is a PVD coating based on Titanium carbide which shows an extremely high hardness (3.900 ± 500 HV) and high resistance to abrasion for avoiding adhesion. Three tests are performed at the two highest load levels. One test is performed at load level 1 and two tests are performed at load level 2. The tool life span is also determined by thermoelectric measurements. Figure 86 shows the evolution of thermoelectric current.

For the test with Formatic Pro, the thermoelectric current under load level 1 and one of the tests under load level 2 increases after 59 m and 62 m of sliding length (Figure 86a), while the current of the other test under load level 2 decreases after 113 m of sliding length. For the test with Duplex Variantic 1000, the thermoelectric current of all tests decreases after 25.8 m, 80.4 m and 113 m of sliding length. According to results shown in Figure 79 and Figure 81, the increase of thermoelectric current indicates adhesive wear and the decrease of the current indicates a breakage of the coating.

The life spans of the tools are shown in comparison to the reference WRC of the SBF of a gear (see Figure 87). It can be found from the WRC that both alternative coating systems show better resistance to wear in higher load levels. At the highest load level, Formatic Pro has significantly better wear resistance, while Duplex Variantic 1000 shows better wear resistance at load level 2.

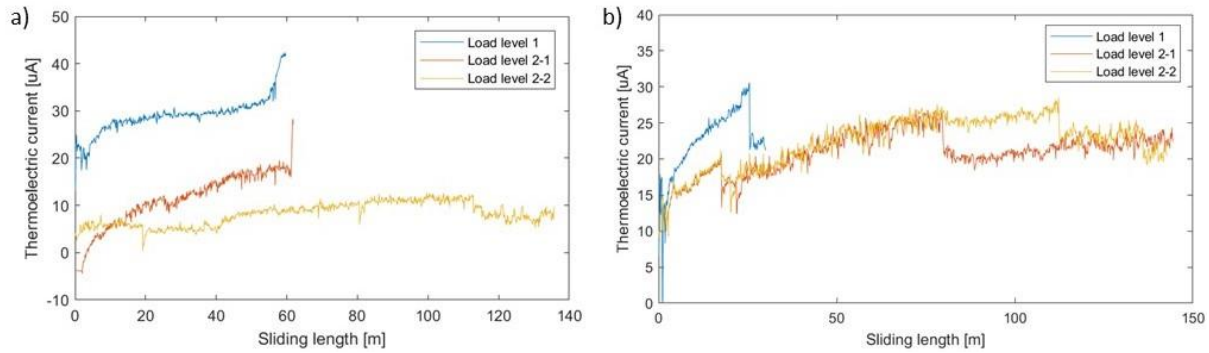

Figure 86 The evolution of thermoelectric current a) Formatic Pro; b) Duplex Variantic 1000

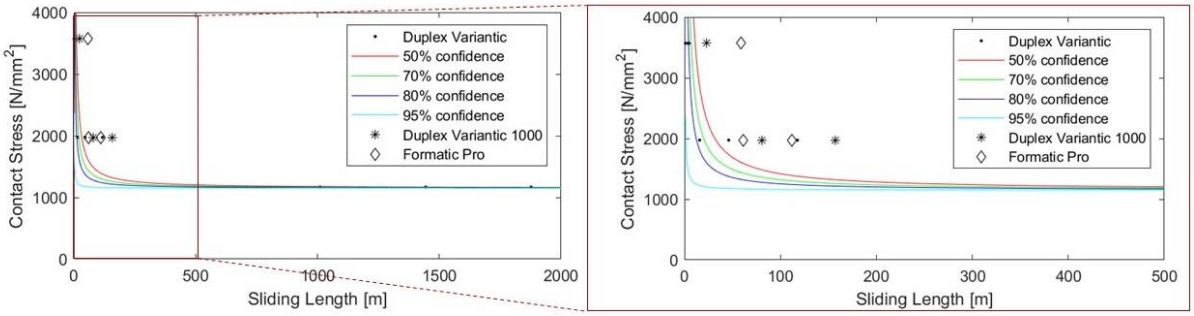

Figure 87 The wear resistance of alternative coating systems

Comparing the same coating family, the life span of Duplex Variantic 1000 is higher than the reference system. According to the measured thermoelectric current (Figure 86b) and the wear mechanism shown in Figure 88, a detachment of coating was observed, which led to a decrease of the thermoelectric current after wear had occurred. Coating breakage also leads to a high tendency for adhesive wear. Compared to Figure 82 and Figure 83, the depth of pitting for Duplex Variantic is 7 µm, while it is over 10 µm for the Duplex Variantic 1000. For lower coating thickness, pitting will cause a higher tendency for adhesion even at a low depth, since the base material is exposed and has direct contact with the sheet. For a higher coating thickness, pitting with a low depth will not cause the exposure of base material and therefore has a lower probability of adhesion. Once the depth of pitting exceeds the coating thickness, the risk for adhesive wear increases and severe galling occurs. As a result, the increase of coating thickness is helpful for extending the life span of tools, since it reduces the risk for exposure of the base material.

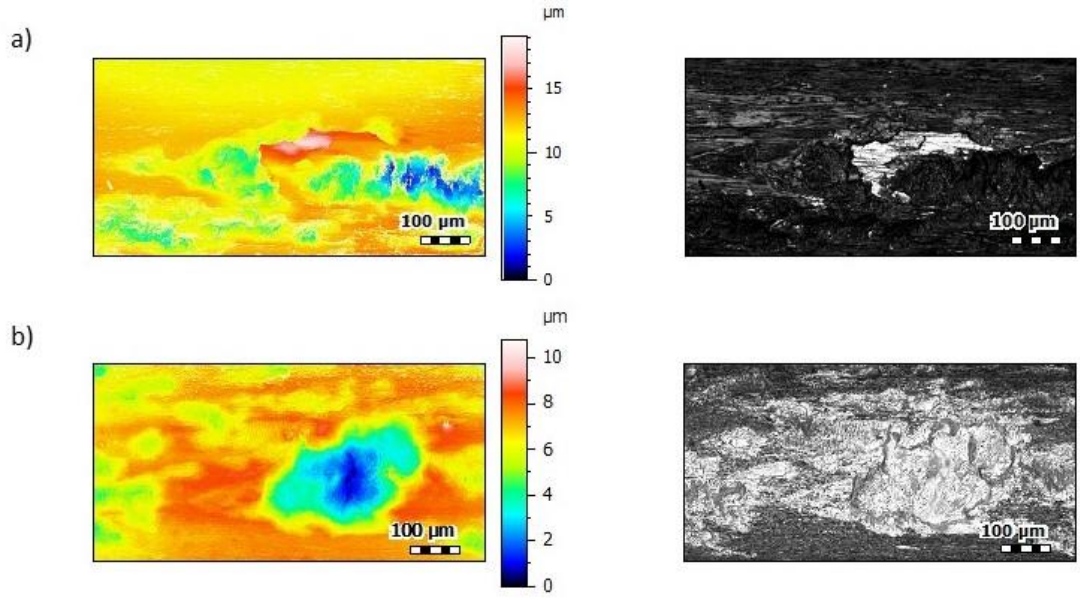

Figure 88 Pitting on the Duplex Variantic 1000 coating a) load level 1; b) load level 2 (drawing direction: from right to left)

In terms of Formatic Pro, the wear resistance is also higher than the original Duplex Variantic, although the coating thickness of the two coatings is the same. The higher hardness and decreased tendency for adhesion to the coating reduces the risk for fatigue wear. At the highest load level, the wear resistance of the Formatic coating is better than the Duplex Variantic 1000 coating.

Figure 89 shows the track of squeezing of the Duplex Variantic 1000 coating for the highest load level. This squeezing causes the coating to be strained in the drawing direction and leads to coating detachment. This kind of squeezing is, however, not visible on the surface of the Formatic Pro coating. On one hand, the contact stress distribution on the tool along the drawing direction is inhomogeneous (see Figure 78b). There are several critical positions with high contact stress. On the other hand, the adhesive force between coating and sheet is not only material-dependent but also load-dependent, which leads to an inhomogeneity of tangential force in the drawing direction. This inhomogeneity leads to surface squeezing when the adhesive tendency between tool and sheet is high. Since the Formatic Pro has a low tendency for adhesion, this causes a small tangential force and reduces the risk of squeezing.

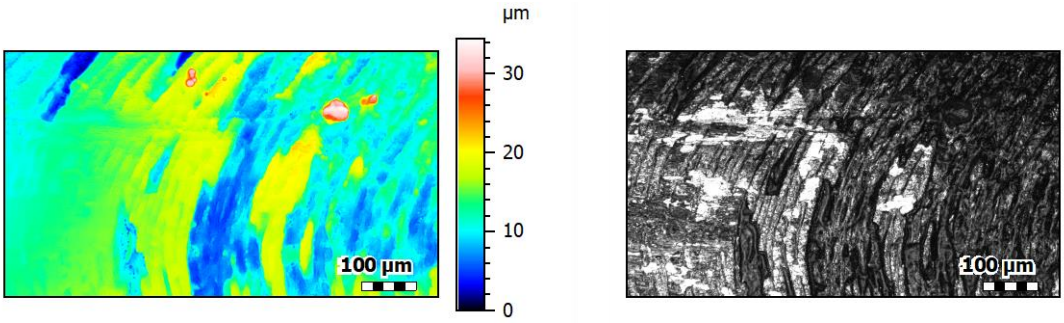

Figure 89 The track of squeezing on the surface of Duplex Variant 1000 (drawing direction: from right to left)

At load level 2, the wear resistance of the Duplex Variantic 1000 coating is higher than that of the Formatic Pro coating. For the tools of this load level, surface squeezing is not visible for Duplex Variantic 1000. The cause for failure is mainly fatigue breakage of the coating but adhesion between tool and sheet metal is no longer a problem. Since the thickness of the Duplex Variantic coating is 7 µm greater than Formatic Pro, it is more resistant to the exposure of the base tool material.

From the example explained in this section, it can be concluded that the wear resistance of alternative tribological systems can be estimated through wear resistance analysis by applying a limited number of tests when a reference WRC is available. For an even lower contact stress, corresponding to the actual forming process, the risk of fatigue wear is much higher than surface squeezing. Therefore, it is deduced that the coating with higher thickness is more important for life span extension in the actual forming process.

7.8 Summary of this chapter

In this chapter, a practical application of tool wear detection through thermoelectric measurement and wear prediction through wear resistance analysis is presented through two case studies, an ironing process and SBF of gears. The tools of both processes are coated and prone to premature wear due to severe tribological loads.

From the case studies, the following conclusions are obtained:

1) The thermoelectric current monitoring is a reliable method for inline detection of severe tool wear, also for coated tools in actual forming processes. Tool breakage leads to a sudden change of the measured thermoelectric current due to the abrupt change of Seebeck coefficient of the tools.

2) The estimation of life span through wear resistance curves (WRC) is also compatible with tribological systems that include a coating. However, different fitting models are used for tribological systems with or without coating. For actual processes with coating, the “Henry and Dayton” estimation model is most compatible. The example shown in section 7.7 reveals that the wear resistance evaluation of alternative (coating) systems is achievable through a limited number of tests, when a reference WRC of a tribological system is available.

3) In this chapter, two typical WRCs for ironing and SBF of gears are given. For a further practical application of this method of life span estimation, different WRCs for typical forming processes should be found. A database for “typical WRCs for forming processes” could be built in the future. With such a database, the influence of factors such as alternative coatings, lubricant systems, sheet metals and tool materials on the wear resistance could be characterized through a limited number of model tests.

8 Conclusion and outlook of the dissertation

Tool wear in metal forming is a process limit and is harmful to an effective production. For several reasons, such as increased demand of light-weight material, ecological specification of lubricants and reduction of over-engineering, wear becomes an issue in manufacturing processes. For a sustainable development, controlling wear effectively has many ecological and economic benefits in metal forming. Firstly, finishing parts with wear defects can be reduced when a reliable wear detection method is available. Secondly, tool maintenance and production planning can be optimized if the tool life spans are predictable. Thirdly, a better understanding of the influence of various parameters on wear supports the know-how for tool and material selection for production to avoid and reduce possible wear occurrence. Therefore, controlling wear effectively requires a combination of three factors: real-time wear detection, accurate estimation of tool life, and characterization of the influence of wear, which are the main topics investigated in this dissertation.

Thermoelectric current monitoring is a sensorless method for wear detection. For wear monitoring, only two cables are needed, one for the blank holder and one for the die. The thermoelectric current is recorded during sliding between tools and sheet metal, which makes inline wear monitoring possible. Moreover, isolation plates are needed to separate the tool set from the other parts of the machine. The effectiveness of wear detection through thermoelectric current is dependent on material characteristics, namely the Seebeck coefficient of the participating contact partners. For wear detection with high sensitivity, a higher sum of Seebeck coefficient of tool and sheet is required. According to the investigation, galling (adhesive wear) detection for both coated and uncoated tools is reliable. For tools with coating, tool breakage can also be detected. In summary, tool wear can be detected in real time and the wear development can be obtained with high time resolution through thermoelectric measurements.

The effectiveness of this measurement principle for real-time wear detection has already been proven in strip drawing tests in the lab. This method for wear detection has a high potential for practical application in actual production. However, several problems should be solved before industrial implementation.

Firstly, the design of isolation plates should be optimized for the requirements of manufacturing. This includes material selection and characterization of material behavior under long-period operation. Secondly, different lubricants and coatings have different characteristics such as Seebeck-coefficient and conductivity. The suitability of coatings and lubricants for wear monitoring with thermoelectric measurement should be evaluated.

Another focus of the dissertation is on indirect wear prediction through wear resistance analysis. Through WRD, the influence of factors such as contact stress, hardness of tools and sheets, and surface roughness on tool life spans can be characterized. This idea is inspired from the S-N curve for fatigue strength estimation. The procedure for evaluating the influence of contact stress through the use of WRC is given in this dissertation. Through WRC, the life spans of typical tribological systems at different operating load levels can be estimated. Because of the high variation of life spans at lower load levels, the WRCs with different conservativeness (confidence levels) are given in this investigation. For practical application, the user can choose the appropriate WRC according to their practical need.

Fitting models for S-N curve estimation are directly compatible with the estimation of WRC. The reason can be explained by the similarities between the development of fatigue failure and tool wear. However, the choice of a specific fitting model depends on whether the tools are coated or not.

The potential for life span estimation through wear resistance analysis is also high. WRCs for two typical metal forming processes are derived in this investigation. For future applications, more WRCs for other typical forming processes should also be found. It is expected that a database with a series of WRCs for different typical forming processes can be determined.

The investigations in this work build a basis for wear control, focused on wear detection and life span estimation of forming tools. Sustainable production is foreseen through wear control of the forming process and subsequent optimization of the method.

Table Content

Figure Content

9 Appendix 1: Device for Seebeck coefficient determination

In this chapter, a device for Seebeck coefficient measurements of sheet metal is introduced. According to Seebeck, thermoelectric voltage emerges when a temperature differences emerges within a certain material. Similar to the approach of Demmel et al. [DEM14], a device for the measurement of Seebeck coefficients is designed.

In Figure 90a, a schematic diagram illustrates the measurement principle of the Seebeck coefficient. The two ends of the sample are placed on a warm and a cold block. The warm block 1 is heated by a ceramic heater with a power of 500 W, while the cold side 2 is connected with a water tank 4. Water with a reference temperature (0°C with ice water or room temperature) is supplied by the water pump 3 through the cold side of the device (see Figure 90c). The whole mentioned system plays a role as a cooler 1. The temperatures of both, the cold and warm sides are measured by the K-Type thermocouples with a measurement frequency of 200 Hz, while the voltage between the cold and warm sides are measured through Quantum MX840A, through which it is possible to measure a voltage in the µV range. The whole function of water supply and evacuating, is realized by a control and measuring system based on Arduino.

In Figure 90b, the method for the measurement data evaluation is illustrated. The Seebeck coefficient at the temperature of T_{warm} corresponds to the gradient of the thermoelectric voltage U_{th} relative to temperature T and can be described as following:

$$S = dU_{th}(T_{warm})/dT \tag{A-1}$$

where S is the determined Seebeck coefficient, T the measured temperature and U_{th} the measured thermoelectric voltage.

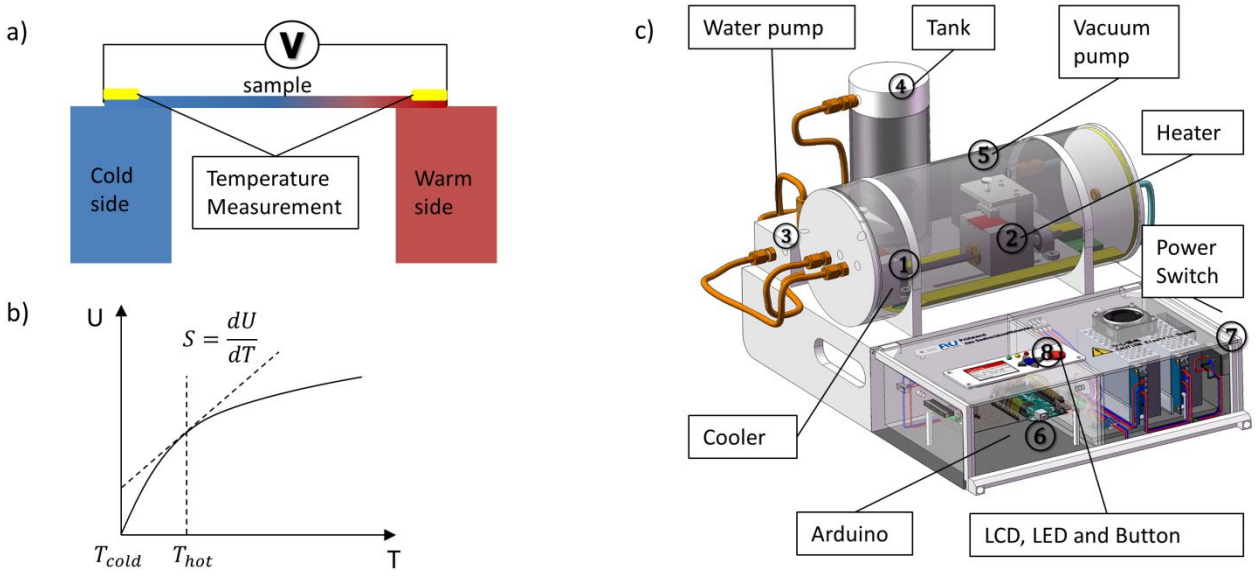

Figure 90 a) Measurement principle of the Seebeck coefficient for metal samples according to Demmel et al. [DEM14]; b) Measured data and method to determine the Seebeck coefficient; c) Illustration of a device for the determination of Seebeck coefficients

Under the background of the wear issue and in the demand for light-weight design, the sheet metals aluminum EN AW-1050A, aluminum alloy EN AW 5083, stainless steel X5CrNi18-10 and high-strength low-alloy steel H630LA (Manufacturer: C.D. Waelzholz) are selected in this approach for evaluation.

After mounting of the sample, the warm block starts heating continuously to 250°C and the thermoelectric voltage between the two ends as well as the temperature of the warm and cold sides are acquired through Quantum MX840A. The integrated Bessel low-pass filter is used for noise filtering.

Figure 91 shows the data of the Seebeck coefficient measurement of three repetitions for each sample. The temperature differences between the warm and cold side are the x-axis, while the measured thermoelectric voltage is the y-axis. The diagram clearly shows a non-linear evolution between the temperature differences and the measured thermoelectric voltage.

The Seebeck coefficient is calculated through the linear regression by applying the “Curve Fitting” Toolbox of MATLAB. The gradient of the linear regression corresponds to the Seebeck coefficient according to equation A-1. Because of its non-linearity, a 2-degree polynomial function is used. This approach of linear

regression for Seebeck coefficient calculation is similar to the approach of Tozaki et al. [YAS17].

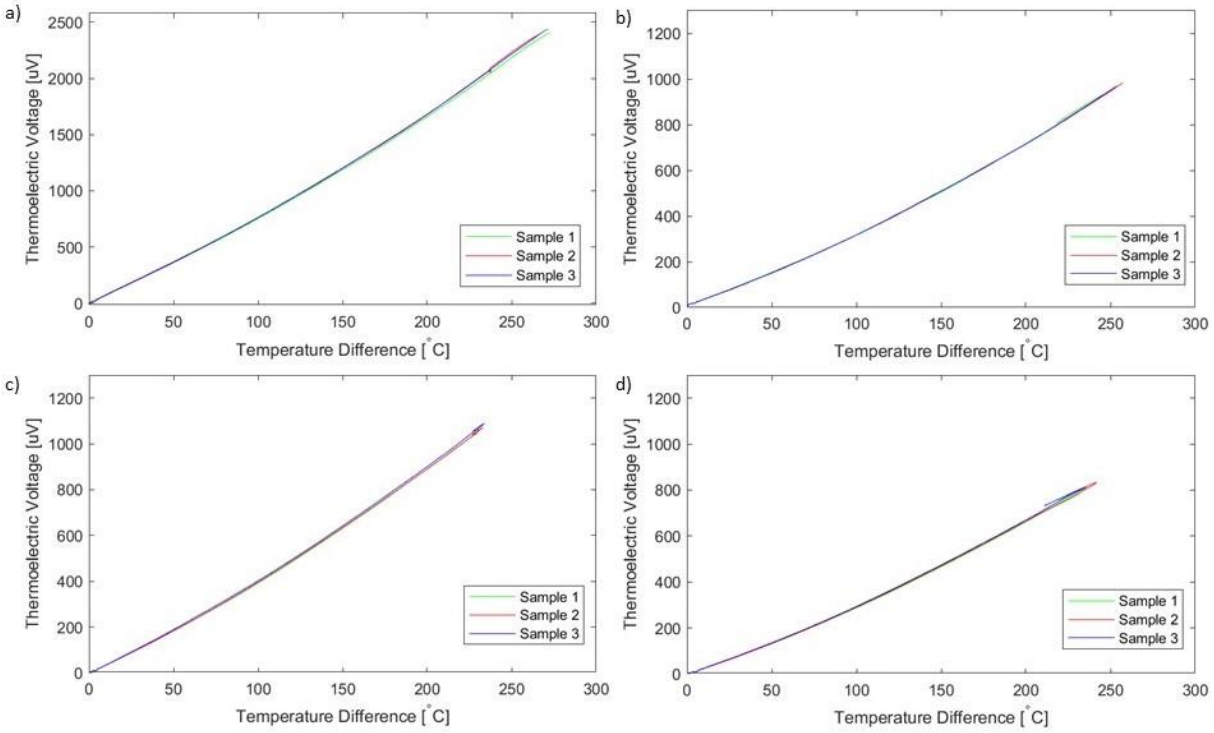

Figure 91 Data of the generated thermoelectric voltage at different temperature differences; x-axis: temperature difference between warm and cold side; y-axis: measured thermoelectric voltage a) H630LA, b) X5CrNi18-10, c) AW 5083, d) AW-1050A

Figure 92 shows the calculated Seebeck coefficients of the test materials after three repetitions. All materials imply a linear temperature-dependent Seebeck coefficient. Since the curves of three repetitions have low variations, it shows a high reproducibility. In terms of the value, it can be identified that the low-alloyed steel sheet H630LA shows the highest Seebeck coefficient with approximately twice higher than stainless steel X5CrNi18-10 and aluminum alloy AW 5083 at room temperature (23 ℃). The aluminum alloy AW 5083 and the stainless steel X5CrNi18-10 show a similar Seebeck coefficient, which is similar to the result of Tröber et al. [TRÖ17a], where the Seebeck coefficient difference between aluminum alloy and stainless steel is close to zero.

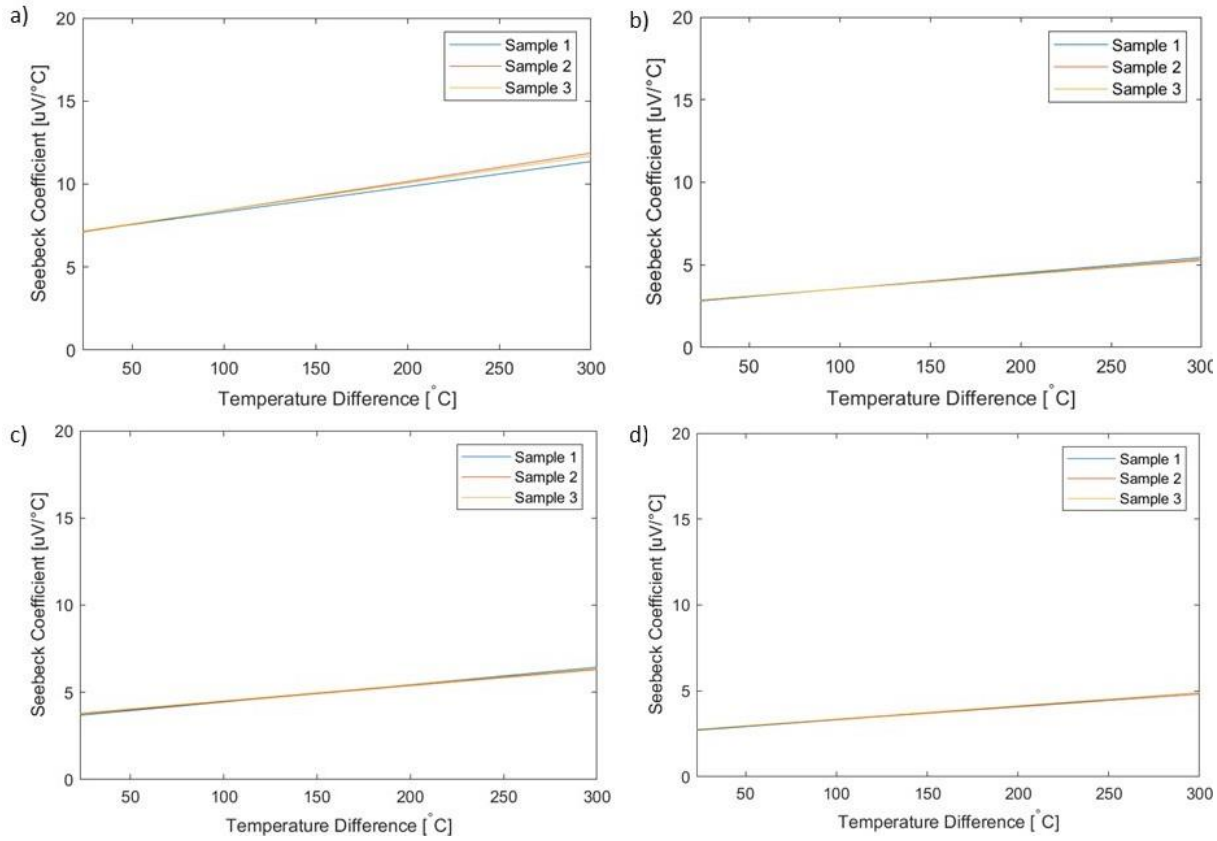

Figure 92 Calculated Seebeck coefficient a) H630LA, b) X5CrNi18-10, c) AW 5083, d) AW-1050A

10 Appendix 2: Mathematical background for WRC derivation

In this appendix, the procedure for pre-selecting the mathematic models for WRC estimation based on S-N curves for fatigue life estimation is described in 10.1 and 10.2. The curve fitting for the derivation of wear resistance curve (WRC) is described in 10.3.

10.1 Models for S-N curve estimation

The concept of fatigue stress of metals was initiated by Wöhler and intended for illustrating the endurance of metals through a series of material tests [WÖH71]. The curve which illustrated the stress and its resulting fatigue load cycles is called “S-N curve” (German: Wöhlerlinie). This is an indirect method for the fatigue strength illustration of materials by means of its life spans. For describing the fatigue strength under all stress levels, several mathematical models are derived which allow S-N curve estimation in different applications [BUR18]. For example, the models of Basquin [BAS10], Weibull [WEI52], Henry [HEN53] and Stromeyer [STR14] are used to estimate the fatigue strength of single metals, while some other models, such as the models of Hwang and Han [HWA86], Sendeckyi [SEN81] and Poursatip and Beaumont [POU86], are used to estimate the fatigue strength of composite materials like glass fiber reinforced materials.

The models for S-N curve estimation are summarized in Table 31. In this paper, 10 models are taken into account.

Table 31 Pre-selected models for S-N Curve estimation

	S-N Curve models	No. of fitting parameters	Material parameters	No. of citing
Basquin [BAS10]	$\sigma_{max} = \alpha(N_f)^{\beta}$	2	-	1963
Stromeyer [STR14]	$\sigma_{max} = \alpha(N_f)^{\beta} + \sigma_{\infty}$	2	σ_{∞}	162

Weibul [WEI52]l	$\sigma_{max} = (\sigma_{uT}) \cdot \exp[-\alpha(\log N_f)^{\beta}]$	2	σ_{uT}	4251
Henry [HEN53]	$\sigma_{max} = \frac{\alpha}{N_f} + \beta$	2	-	187
Sendeckyj [SEN81]	$\sigma_{max} = \frac{\sigma_{uT}}{(1 - \alpha + \alpha N_f)^{\beta}}$	2	σ_{uT}	158
Hwang and Han [HWA86]	$\sigma_{max} = \sigma_{uT}(1 - \frac{N_f^{\beta}}{\alpha})$	2	σ_{uT}	403
Kohout [KOH01]	$\sigma_{max} = \sigma_{\infty}[\frac{(N_f + \alpha)}{N_f + \gamma}]^{\beta} = \sigma_{uT}[\frac{(1 + {N_f}/{\alpha})}{1 + {N_f}/{\gamma}}]^{\beta}$	3	σ_{uT} , σ_{∞}	133
Kim and Zhang [KIM01]	$\sigma_{max} = \sigma_{uT}(\frac{\alpha(\beta - 1)(N_f + N_0)}{\sigma_{uT}^{-\beta}} + 1)^{\frac{1}{1-\beta}}$	2	σ_{uT}	25
Poursartip [POU86]	$N_f = \alpha(\frac{\sigma_{max}}{\sigma_{uT}})^{-6.393} \cdot (\frac{\sigma_{uT} - \sigma_{max}}{\sigma_{uT}})$	1	σ_{uT}	130
D'Amore [D'A96]	$N_f = [\frac{\sigma_{uT} - \sigma_{max}}{\alpha' \cdot \sigma_{max}} + 1]^{1/\beta}$	2	σ_{uT}	78

In these models, the parameter σ_{max} stands for the stress amplitude and N_f the fatigue load cycles. For the application of the models for a specific material, the values for model parameters such as α, β and γ have to be determined through curve-fitting. Additionally, data for material parameters such as σ_{∞} and σ_{uT} are necessary for some models. The fatigue limit σ_{∞} is defined as the stress limit, under which an infinite number of fatigue load cycles can be achieved by the material [BEE92]. The ultimate tensile strength σ_{uT} corresponds to the tensile strength of the material and in definition of the fatigue strength it can be defined as "the failure of material occurs within one cycle under the ultimate tensile strength". In the following section, the procedure for WRC-estimation by applying the models known from the S-N curve is presented.

10.2 Pre-selection of the models

Before estimating the WRC by using the models for S-N curves, the similarities between the WRC and the S-N curve are discussed.

The S-N curve shows the reachable number of load cycles under different stress amplitudes for a specific material such as isotropic steel or composite material, while the WRC defines the reachable life span of a tool in a tribological system under different levels of contact stress. The concept of “stress amplitude” in the S-N curve models corresponds to the “contact stress” of the WRC. Both concepts serve as the input of the model. The output parameters of the models are the life span of the material (S-N curve) and tool before severe wear occurs (WRC). Because of these similarities, the parameter $\sigma_{\max}$ in the S-N curve can be substituted by the parameter p (contact stress) in WRC and the parameter N_f (fatigue load cycles) can be replaced by L (sliding length or stroke number). The substitution of parameters between S-N curve and WRC is illustrated in the following table:

S-N Curve	WRC
$N_f = f(\sigma_{max})$	$L = f(p)$

The model selection procedure for the WRC estimation consists of two steps. Firstly, if the models for a S-N curve include parameters, which do not exist or are difficult to define in the concept of wear resistance analysis, the models are no longer considered as transferable. For example, the fatigue limit $\sigma_{\max}$ does not always exist even in fatigue strength analysis [BAT99]. When analyzing wear resistance, this parameter is also difficult to define, since according to Archard's wear model, wear always occurs no matter how low the contact stress is [ARC53]. Therefore, the models in Table 31 with the material parameter $\sigma_{\max}$ are not suitable for wear resistance estimation (eg. The fitting models “Stromeyer” and “Kohout”) On the other hand, ultimate tensile strength σ_{uT} does exist and is definable in wear resistance analysis. σ_{uT} can be defined as “the failure occurs after one load cycle” in the field of fatigue life study, while in the field of wear resistance analysis, it can be defined as “the ultimate contact stress, under which the severe wear occurs after a very short sliding distance”. Christiany defines the “very short sliding distance” as 1 m in the strip drawing

test [CHR16]. Thus, a material parameter, the "ultimate contact stress p_{uT}" is derived with the definition "the contact stress, under which the severe wear occurs over a sliding distance of 1 m".

In this dissertation, the models for fatigue life estimation with highest citing frequency in international journals are pre-selected for applicability in the life span estimation. Four models with the widest spread (determined by the number of citations in Table 31) are considered in this work: "Basquin", "Weibull", "Henry and Dayton" and "Hwang and Han". The equations after parameter substitution and linearization are summarized in Table 32.

Table 32 Selected equations after parameter substitution and linearization for WRC estimation

S-N curve model	Original equation	Linearized equation
Basquin	$p = \alpha(L)^{\beta}$	$\log p = \log \alpha + \beta \log L$
Weibull	$p = p_{uT} \cdot \exp(-\alpha(\log L)^{\beta})$	$\log[-\log(\frac{p}{p_{uT}})] = \log \alpha + \beta \log(\log L)$
Henry and Dayton	$p = \frac{\alpha}{L} + \beta$	$pL = \alpha + \beta L$
Hwang and Han	$p = p_{uT}(1 - \frac{L^{\beta}}{\alpha})$	$\log(1 - \frac{p}{p_{uT}}) = -\log \alpha + \beta \log L$

10.3 Determination of fitting parameters

After the model selection, the fitting parameters α and β of the selected models are determined. Since these parameters are estimated parameters, the fitting parameters are named as $\hat{\alpha}$ and $\hat{\beta}$ in this work.

Since the variation of tool life spans at lower load levels is relatively high due to the complexity of the tribological system [GRO19a], not only the median of life

span but also its uncertainties are considered through quantile calculation for a reliable life span estimation in this study.

Compared to the curve fitting method “least square error”, the method “Maximum likelihood estimation (MLE)” is more suitable for curve fitting in this research, since the determination of the fitting parameters can be related to the probability density function (PDF) from a sample set [MYU03]. By using the PDF, it is possible to derive curves not only with 50 % confidence (median) but also with other confidence levels through quantile calculation. Therefore, a set of curves with different certainties is to be defined. In this section, the mathematical derivation of curve fitting of median and quantiles are discussed. It is assumed that the distribution of the life span data for each load level follows the normal random distribution. For curve fitting with MLE, the equations should be linearized. The linearized equations are shown in Table 32.

When it comes to estimating the fitting parameters in a linear function (slope and intercept) using MSE, a linear regression is adopted. In linear regression, there is a basic hypothesis that the linear function is as follows:

$$\mathrm{y} = \hat{\mathrm{a}} + \hat{\mathrm{b}}\mathrm{x} + \varepsilon, \qquad \varepsilon \in \mathrm{N}(0, \sigma^2) \tag{A-2}$$

in which ε is the random error, and $\hat{\mathrm{a}}$ and $\hat{\mathrm{b}}$ the to be determined fitting parameters. Taking the Basquin model in Table 32 as an example, the linearized equation can be written in $\mathrm{x} = \log(\mathrm{L})\,; \mathrm{y} = \log(\mathrm{p})\,; \hat{\mathrm{a}} = \log(\hat{\alpha});\ \hat{\mathrm{b}} = \log(\hat{\beta})$. After the determination of $\hat{\mathrm{a}}$ and $\hat{\mathrm{b}}$, the fitting paramters $\hat{\alpha}$ and $\hat{\beta}$ can be calculated accordingly.

This equation is called unary linear regression model:

$$\varepsilon = \mathrm{y} - \hat{\mathrm{a}} + \hat{\mathrm{b}}\mathrm{x} \tag{A-3}$$

Supposing the variation of the tool life span follows the normal distribution, the likelihood function of collected samples $(x_1, y_1),\ (x_2, y_2),\ (x_n, y_n)$ for ε is:

$$Li = \prod_{i=1}^{n} \frac{1}{\sigma\sqrt{2\pi}} \cdot \exp\left[-\frac{1}{2\sigma^2}(y_i - \hat{a} - \hat{b}x_i)^2\right] \tag{A-4}$$

For the determination of the maximum value of the likelihood function (equation A-4), it is to be assumed the equation:

$$Q(\hat{a},\hat{b}) = \sum_{i=1}^{n}(y_i - \hat{a} - \hat{b}x_i)^2 \tag{A-5}$$

being the minimum.

Taking partial derivative of $\hat{a}$ and $\hat{b}$ of equation (A-5) and solving the equations $\frac{\partial Q}{\partial \hat{a}} = 0$; $\frac{\partial Q}{\partial \hat{b}} = 0$, equation A-5 can be obtained:

$$\begin{cases} n\hat{a} + (\sum_{i=1}^{n} x_i)\hat{b} = \sum_{i=1}^{n} y_i \\ (\sum_{i=1}^{n} x_i)\hat{a} + (\sum_{i=1}^{n} x_i^2)\hat{b} = \sum_{i=1}^{n} x_i y_i \end{cases} \tag{A-6}$$

$\hat{a}$ and $\hat{b}$ can be determined by solving equation (A-6). The result is given by equation (A-7):

$$\begin{cases} \hat{b} = \frac{n\sum_{i=1}^{n} x_i y_i - (\sum_{i=1}^{n} x_i)(\sum_{i=1}^{n} y_i)}{n\sum_{i=1}^{n} x_i^2 - (\sum_{i=1}^{n} x_i)^2} \\ \hat{a} = \frac{1}{n}\sum_{i=1}^{n} y_i - \frac{\hat{b}}{n}\sum_{i=1}^{n} y_i \end{cases} \tag{A-7}$$

After the determination of $\hat{a}$ and $\hat{b}$, the fitting parameters $\hat{\alpha}$ and $\hat{\beta}$ can be calculated according to Table 32.

For quantile estimation, the quantile line can be fitted by adjusting the fitting parameters $\hat{a}$ into $\widehat{a_q}$, supposing that the distribution obeys the Gauss distribution. For a q % quantile, the adjusted parameter $\widehat{a_q}$ is as following:

$$\widehat{a_q} = \hat{a} + \Phi^{-1}(q) \cdot \hat{\sigma} \tag{A-8}$$

The $\hat{\sigma}$ stands for the standard deviation of the random error ε (see equation A-1).

The calculation of σ follows [WEI14]:

$$\hat{\sigma}^2 = \frac{Q(\hat{a},\hat{b})}{n-2} \tag{A-9}$$

Therefore, $\widehat{a_q}$ can be calculated by combining the equations (A-8) and (A-9):

$$\widehat{a_q} = \hat{a} + \Phi^{-1}(q)\sqrt{\frac{\sum_{i=1}^{n}(y_i - \hat{a} - \hat{b}x_i)^2}{n-2}} \tag{A-10}$$

After the determination of $\widehat{a_q}$, the fitting parameter for quantile $\hat{\alpha}$ can also be determined through transformation according to the equations in Table 32.

The parameter $\Phi^{-1}(q)$ can be obtained from the „Standard normal table“ according to the targeted confidence grade of the estimation. For example, a 95 % confidence level corresponds to the 5 % quantile of the normal distribution. This means that 95 % of the obtained life span data is located on the right side of the estimated curve with a 95 % confidence and the probability of error is 5 %.

11 Appendix 3: Methods for wear detection in state of the art

Table 33 Overview: methods for wear detection in the field of metal forming in academic journals

Literature	VA	2D	3D	Mass	COF	Force	T	AE	Related Process
[SWA88]	x								Pin-on-disc
[SCH93]	x								SMF
[SCH93]	x								SMF
[AND98]	x		x						SMF
[VAN01]			x		x				SMF
[ATT02]	x								Deep drawing
[SKÅ03]	x			x		x			SMF
[FIL04]	x					x			SMF
[POD04]	x	x			x				General metal forming
[SHA07]	x				X				General dry forming
[CHR08]	x		x						SMF
[OLS09]	x	x	x			x		x	Deep drawing
[GÅÅ09a]	x	x	x						Roll forming
[COR09]	x		x						Pin-on-disc
[FIG11]	x								SMF
[GAL11]	x	x			X		x		Roll forming
[GRO11]	x			x					SMF
[KAR12]	x	x	x						Roll forming

[HAS12]	x							x	Pin-on-disc
[HAS14]	x							x	
[WAN13]	x			x					SMF
[PUJ13]	x				x				Pin-on-disc
[GRO13a]	x	x	x				x		SMF
[UBH17]	x	x						x	Stamping
[MOG17b]	x					x		x	SMF
[MOG17a]	x					x		x	SMF
[MOG20]	x					x			Stamping
[GRO19a]	x	x							SMF
[VET13]	x								General dry forming
Sum	28	8	8	3	10		2	5	

Abbreviations:

VA: Visual assessment; 2D: 2-dimensional roughness measurement; 3D: three-dimensional roughness measurement; Mass: mass measurement; COF: Measurement of coefficient of friction; Force: Measurement of force (e.g.: Punch force); T: Temperature; AE: Acoustic emission

SMF: sheet metal forming

12 Literature

ABR18 Abraham, T. et al.: Observation of the aC: H run-in behaviour for dry forming applications of aluminium. In: MATEC Web of Conferences : EDP Sciences, 2018 (190), S. 14001

AME19 American Society of Mechanical Engineers: Surface texture - (surface roughness, waviness, and lay) : an international standard. New York, NY: The American Society of Mechanical Engineers, 2019.

AND98 Andreasen, J. L.; Bay, N.; Chiffre, L. de: Quantification of galling in sheet metal forming by surface topography characterisation. In: International Journal of Machine Tools and Manufacture 38, Nr. 5, 1998, S. 503–510. URL: https://www.sciencedirect.com/science/article/pii/S089069559700095 3

ARC53 Archard, J. F.: Contact and Rubbing of Flat Surfaces. In: Journal of Applied Physics 24, Nr. 8, 1953, S. 981–988

ASH76 ASHCROFT, N. W. ; MERMIN, N. D.: Solid state physics: Solid state physics. holt, rinehart and winston, new york London, 1976

ATT02 Attaf, D. (Hrsg.); Penazzi, L. (Hrsg.); Boher, C. (Hrsg.); Levaillant, C. (Hrsg.): Mechanical study of a sheet metal forming dies wear, 2002.

AVL15 Avlonitis, M.; Kalaitzidou, K.: Estimating the real contact area between sliding surfaces by means of a modified OFC model. In: Archives of Civil and Mechanical Engineering 15, Nr. 2, 2015, S. 355–360. URL: https://www.sciencedirect.com/science/article/pii/S1644966514001411

BAS10 Basquin, O. H.: The exponential law of endurance tests. In: Proc Am Soc Test Mater, 1910 (10), S. 625–630

BAT99 Bathias, C.: There is no infinite fatigue life in metallic materials. In: Fatigue & fracture of engineering materials & structures 22, Nr. 7, 1999, S. 559–565

BAY94 Bay, N.: The state of the art in cold forging lubrication. In: Journal of Materials Processing Technology 46, 1-2, 1994, S. 19–40

BAY10 Bay, N. et al.: Environmentally benign tribo-systems for metal forming. In: CIRP Annals 59, Nr. 2, 2010, S. 760–780

BAY08 Bay, N.; Olsson, D. D.; Andreasen, J. L.: Lubricant test methods for sheet metal forming. In: Tribology international 41, Nr. 9, 2008, S. 844–853. URL: https://www.sciencedirect.com/science/article/pii/S0301679X070020 6X

BAY04 Bayer, R. G.: Mechanical Wear Fundamentals and Testing, revised and expanded: CRC Press, 2004.

BAY75 Bayer, R. G.; Sirico, J. L.: The influence of surface roughness on wear. In: Wear 35, Nr. 2, 1975, S. 251–260

BEE92 Beer, Ferdinand P.; Johnston, E. R.: Mechanics of materials. New York: McGraw-Hill, 1992.

BEH08 Behrens, B.-A.: Finite element analysis of die wear in hot forging processes. In: CIRP Annals 57, Nr. 1, 2008, S. 305–308

BEH17a Behrens, B.-A. et al.: Development and validation of a new method for accelerated and economic wear testing of tool materials for deep drawing applications. In: Wear 376-377, 2017, S. 1814–1821

BEH17b Behrens, B.-A. et al.: Wear behavior of MoS2 lubricant layers during sheet metal forming. In: Procedia Engineering 183, 2017, S. 357–362

BER01 Berdin, C.; Dong, M. J.; Prioul, C.: Local approach of damage and fracture toughness for nodular cast iron. In: Engineering Fracture Mechanics 68, Nr. 9, 2001, S. 1107–1117

BHU03 Bhushan, B.; Ko, P.: Introduction to tribology. In: Appl. Mech. Rev. 56, Nr. 1, 2003, B6-B7

BLA05 Blau, P. J.: On the nature of running-in. In: Tribology international 38, 11-12, 2005, S. 1007–1012

BUC81 Buckley, D. H.: Surface effects in adhesion, friction, wear, and lubrication: Elsevier, 1981.

BUR18 Burhan, I.; Kim, H.: SN curve models for composite materials characterisation: An evaluative review. In: Journal of Composites Science 2, Nr. 3, 2018, S. 38

CAL79 Calais, J-L: Introduction to solid state theory (Springer series in solid state sciences. Vol. 2) by O. Madelung. In: Acta Crystallographica Section A: Crystal Physics, Diffraction, Theoretical and General Crystallography 35, Nr. 6, 1979, S. 1087–1088

CHE16 Chen, L. et al.: A Reliability Accelerated Test of High-speed Punch Based on Failure Analysis. In: MATEC Web of Conferences 61, 2016, S. 4003

CHO12 Choi, C.; Groseclose, A.; Altan, T.: Estimation of plastic deformation and abrasive wear in warm forging dies. In: Journal of Materials Processing Technology 212, Nr. 8, 2012, S. 1742–1752

CHR08 Christiansen, S.; Chiffre, L. de: Topographic Characterization of Progressive Wear on Deep Drawing Dies. In: Tribology Transactions 40, Nr. 2, 2008, S. 346–352

CHR16 Christiany, M.: Methode zur Analyse des Verschleißverhaltens in der Blechumformung: Shaker Verlag, 2016.

CHR14 Christiany, M.; Groche, P.: Reproducibility of Wear Tests and the Effect of Load on Tool Life in Sheet Metal Forming. In: Advanced Materials Research 1018, 2014, S. 293–300. URL: https://www.scientific.net/AMR.1018.293

CLA10 CLAUDE, B. ; PINEAU, A.: Fatigue of Materials and Structures-Fundamentals: Fatigue of Materials and Structures-Fundamentals. John Wiley & Sons, 2010

CLA87 Clayton, P. et al.: Wear behavior of bainitic steels. In: Wear 120, Nr. 2, 1987, S. 199–220

COR09 Cora, O. N.; Koç, M.: Experimental investigations on wear resistance characteristics of alternative die materials for stamping of advanced

high-strength steels (AHSS). In: International Journal of Machine Tools and Manufacture 49, 12-13, 2009, S. 897–905

CZI10 Czichos, H.; Habig, K.-H.: Tribologie-Handbuch: Tribometrie, Tribomaterialien, Tribotechnik: Springer-Verlag, 2010.

D'A96 D'amore, A. et al.: Effect of stress ratio on the flexural fatigue behaviour of continuous strand mat reinforced plastics. In: Science and Engineering of Composite Materials 5, Nr. 1, 1996, S. 1–8

DEM13 Demmel, P. et al.: Characterization of the Thermoelectric Behavior of Plastically Deformed Steels by Means of Relative Seebeck Coefficient. In: Materials Science Forum 755, 2013, S. 1–7. URL: https://www.scientific.net/MSF.755.1

DEM14 Demmel, P.: In-situ Temperaturmessung beim Scherschneiden. Technische Universität München. 2014

DET02 Deters, L. et al.: Gesellschaft für Tribologie Arbeitsblatt 7: Tribologie: Gesellschaft für Triblogie, 2002.

DOH15 Dohda, K. et al.: Tribology in metal forming at elevated temperatures. In: Friction 3, Nr. 1, 2015, S. 1–27

DOM21 Domitner, J. et al.: Characterization of wear and friction between tool steel and aluminum alloys in sheet forming at room temperature. In: Journal of Manufacturing Processes 64, 2021, S. 774–784

DOR92 Dornfeld, D.: Application of acoustic emission techniques in manufacturing. In: NDT & E International 25, Nr. 6, 1992, S. 259–269. URL: https://www.sciencedirect.com/science/article/pii/096386959290636U

EHR13 Ehrlenspiel, K.; Meerkamm, H.: Integrierte produktentwicklung: Denkabläufe, methodeneinsatz, zusammenarbeit: Carl Hanser Verlag GmbH Co KG, 2013.

EMM97 Emmens, W. C.: Tribology of flat contacts and its application in deep drawing, 1997.

ERS08 Ersoy-Nürnberg, K. et al.: Simulation of wear on sheet metal forming tools—An energy approach. In: Wear 265, 11-12, 2008, S. 1801–1807

EYT32 Eytelwein, J. A.: Handbuch der Statik fester Körper: mit vorzüglicher Rücksicht auf ihre Anwendung in der Architektur: de Gruyter, 1832.

FIG11 Figueiredo, L. et al.: Experimental study of friction in sheet metal forming. In: Wear 271, 9-10, 2011, S. 1651–1657

FIL22 Filali, O. et al.: Numerical prediction of the galling of aluminium alloys in cold strip drawing. In: Journal of Manufacturing Processes 73, 2022, S. 340–353. URL: https://www.sciencedirect.com/science/article/pii/S1526612521008094

FIL04 Filzek, J.: Kombinierte Prüfmethode für das Reib-, Verschleiß-und Abriebverhalten beim Tief-und Streckziehen: Shaker Darmstadt, Germany, 2004.

GÅÅ08 Gåård, A.; Krakhmalev, P.; Bergström, J.: Wear mechanisms in deep drawing of carbon steel – correlation to laboratory testing. In: Tribotest 14, Nr. 1, 2008, S. 1–9

GÅÅ09a Gåård, A.; Krakhmalev, P.; Bergström, J.: Influence of tool steel microstructure on origin of galling initiation and wear mechanisms under dry sliding against a carbon steel sheet. In: Wear 267, Nr. 1, 2009, S. 387–393. URL: https://www.sciencedirect.com/science/article/pii/S0043164809000726

GÅÅ09b Gåård, A.; Krakhmalev, P.; Bergström, J.: Wear mechanisms in galling: cold work tool materials sliding against high-strength carbon steel sheets. In: Tribology Letters 33, Nr. 1, 2009, S. 45–53

GAH87 Gahr, K.-H. Z.: Microstructure and wear of materials: Elsevier, 1987.

GAH88 Gahr, K.-H. Z.: Modelling of two-body abrasive wear. In: Wear 124, Nr. 1, 1988, S. 87–103

GAL11 Galakhar, A. S. et al.: Adhesive tool wear in the cold roll forming process. In: Wear 271, Nr. 11, 2011, S. 2728–2745. URL:

https://www.sciencedirect.com/science/article/pii/S004316481100439X

GEN19 Geng, Z.; Puhan, D.; Reddyhoff, T.: Using acoustic emission to characterize friction and wear in dry sliding steel contacts. In: Tribology international 134, 2019, S. 394–407. URL: https://www.sciencedirect.com/science/article/pii/S0301679X19300775

DIN16, 25178: *Geometrical product specifications (GPS) - Surface texture: Areal - Part 1: Indication of surface texture (ISO 25178-1:2016); German version EN ISO 25178-1:2016*

DIN98 DIN, 4288: *Geometrical Product Specifications (GPS) - Surface texture: Profile method - Rules and procedures for the assessment of surface texture*

GOH18 Gohar, R.; Rahnejat, H.: Fundamentals Of Tribology (Third Edition): World Scientific, 2018.

GON11 Gong, F. et al.: Micro deep drawing of micro cups by using DLC film coated blank holders and dies. In: Diamond and Related Materials 20, Nr. 2, 2011, S. 196–200

GRO11 Groche, P. et al.: Influence of gliding speed and contact pressure on the wear of forming tools. In: Wear 271, 9-10, 2011, S. 2570–2578

GRO13a Groche, P.; Christiany, M.: Evaluation of the potential of tool materials for the cold forming of advanced high strength steels. In: Wear 302, 1-2, 2013, S. 1279–1285

GRO13b Groche, P.; Christiany, M.: Qualifizierung neuer Tribosysteme zur Umformung höchstfester Stahlbleche - Ergebnisse eines Vorhabens der industriellen Gemeinschaftsforschung (IGF). Hannover, 2013 (EFB-Forschungsbericht EFB-363)

GRO19a Groche, P.; Christiany, M.; Wu, Y.: Load-dependent wear in sheet metal forming. In: Wear 422-423, 2019, S. 252–260

GRO08 Groche, P.; Nitzsche, G.; Elsen, A.: Adhesive wear in deep drawing of aluminum sheets. In: CIRP Annals 57, Nr. 1, 2008, S. 295–298. URL:

https://www.sciencedirect.com/science/article/pii/S0007850608001030

GRO19b Groche, P.; Wu, Y.: Inline observation of tool wear in deep drawing with thermoelectric and optical measurements. In: CIRP Annals 68, Nr. 1, 2019, S. 567–570

GUO09 Guo, B. et al.: Flow stress and tribology size effects in scaled down cylinder compression. In: Transactions of Nonferrous Metals Society of China 19, 2009, s516-s520. URL: https://www.sciencedirect.com/science/article/pii/S1003632610601008

HAB80 Habig, K.-H.: Wear and Hardness in Metals(Verschleiss und Harte von Werkstoffen). In: Carl Hanser Verlag, 1980, S. 303

HAN13 Han, X.; Hua, L.: 3D FE modelling of contact pressure response in cold rotary forging. In: Tribology international 57, 2013, S. 115–123

HAN08 Hanson, M.: On adhesion and galling in metal forming. Acta Universitatis Upsaliensis. 2008

HAS12 Hase, A.; Mishina, H.; Wada, M.: Correlation between features of acoustic emission signals and mechanical wear mechanisms. In: Wear 292-293, 2012, S. 144–150. URL: https://www.sciencedirect.com/science/article/pii/S0043164812001949

HAS14 Hase, A.; Wada, M.; Mishina, H.: Scanning electron microscope observation study for identification of wear mechanism using acoustic emission technique. In: Tribology international 72, 2014, S. 51–57. URL: https://www.sciencedirect.com/science/article/pii/S0301679X13004009X

HAS03 Hassui, A.; Diniz, A. E.: Correlating surface roughness and vibration on plunge cylindrical grinding of steel. In: International Journal of Machine Tools and Manufacture 43, Nr. 8, 2003, S. 855–862. URL:

https://www.sciencedirect.com/science/article/pii/S089069550300049X

HEN53 Henry, D.: A theory of fatigue damage accumulation in steel. Ohio State University. 1953

HOF05 Hoffmann, H.; Hwang, C.; Ersoy-Nürnberg, K.: Advanced Wear Simulation in Sheet Metal Forming. In: CIRP Annals 54, Nr. 1, 2005, S. 217–220

HOF12 Hoffmann, H. (Hrsg.); Neugebauer, R. (Hrsg.); Spur, G. (Hrsg.): Handbuch Umformen. 2., vollständig neu bearbeitete Auflage. München: Hanser, 2012.

HOL12 Hol, J. et al.: Advanced friction modeling for sheet metal forming. In: Wear 286-287, 2012, S. 66–78

HOR01 Hortig, D.; Schmoeckel, D.: Analysis of local loads on the draw die profile with regard to wear using the FEM and experimental investigations. In: Journal of Materials Processing Technology 115, Nr. 1, 2001, S. 153–158

HUA12 Huang, M. L.; Zhou, S.; Chen, L.: Electromigration-Induced Interfacial Reactions in Cu/Sn/Electroless Ni-P Solder Interconnects. In: Journal of Electronic Materials 41, Nr. 4, 2012, S. 730–740

HWA86 Hwang, W.; Han, K.: Fatigue of composites—fatigue modulus concept and life prediction. In: Journal of Composite Materials 20, Nr. 2, 1986, S. 154–165

KAR12 Karlsson, P. et al.: Galling resistance and wear mechanisms for cold-work tool steels in lubricated sliding against high strength stainless steel sheets. In: Wear 286-287, 2012, S. 92–97. URL: https://www.sciencedirect.com/science/article/pii/S0043164811002481

KIM08 Kim, H. et al.: Evaluation of tool materials, coatings and lubricants in forming galvanized advanced high strength steels (AHSS). In: CIRP Annals 57, Nr. 1, 2008, S. 299–304

KIM01 Kim, H.; Zhang, J.: Fatigue damage and life prediction of glass/vinyl ester composites. In: Journal of reinforced plastics and composites 20, Nr. 10, 2001, S. 834–848

KIM97 Kim, T. H.; Kim, B. M.; Choi, J. C.: Prediction of die wear in the wire-drawing process. In: Journal of Materials Processing Technology 65, 1-3, 1997, S. 11–17

KOH01 Kohout, J.; Vechet, S.: A new function for fatigue curves characterization and its multiple merits. In: International Journal of Fatigue 23, Nr. 2, 2001, S. 175–183

KÖN06 König, W.: Fertigungsverfahren 4 - Umformen. 5., neu bearbeitete Auflage. Berlin, Heidelberg: Springer Berlin Heidelberg, 2006.

KOP14 Kopeliovich, D.: Mechanisms of wear. In: Mechanisms of Wear, 2014.

KOV09 Kovaříková, I. et al.: Study and characteristic of abrasive wear mechanisms. In: Materials Science and Technology 1, 2009, S. 1–8

KRA69 Kragelsky, I. V.; Kombalov, V. S.: Calculation of value of stable roughness after running-in (elastic contact). In: Wear 14, Nr. 2, 1969, S. 137–140. URL: https://www.sciencedirect.com/science/article/pii/0043164869903445

KUB21 Kubik, C.; Hohmann, J.; Groche, P.: Exploitation of force displacement curves in blanking—feature engineering beyond defect detection. In: The International Journal of Advanced Manufacturing Technology 113, Nr. 1, 2021, S. 261–278

KUM02 Kumar, R.; Prakash, B.; Sethuramiah, A.: A systematic methodology to characterise the running-in and steady-state wear processes. In: Wear 252, Nr. 5, 2002, S. 445–453. URL: https://www.sciencedirect.com/science/article/pii/S004316480100895X

KUW07 Kuwer, C.-J.: Verschleißreduktion beim Tiefziehen von X 5 CrNi 18-10. Dissertation, Aachen, Techn. Hochsch., 2007. 2007

LIM87 Lim, S. C.; Ashby, M. F.; Brunton, J. H.: Wear-rate transitions and their relationship to wear mechanisms. In: Acta Metallurgica 35, Nr. 6,

1987, S. 1343–1348. URL: https://www.sciencedirect.com/science/article/pii/0001616087900162

LUD12 Ludwig, M.: Advanced friction model for cold forging processes, 2012, S. 1003

MER11 Merklein, M. et al.: Overview on sheet-bulk metal forming processes. In: Proceedings of the 10th International Conference on Technology of Plasticity, Aachen, Germany, 2011, S. 1109–1114

MER12a Merklein, M. et al.: Bulk forming of sheet metal. In: CIRP Annals 61, Nr. 2, 2012, S. 725–745

MER12b Merklein, M. et al.: Bulk forming of sheet metal. In: CIRP Annals 61, Nr. 2, 2012, S. 725–745

MOG17a Moghadam, M. et al.: Acoustic emission monitoring of the bending under tension test. In: Procedia Engineering 207, 2017, S. 1421–1426

MOG19a Moghadam, M.: Limits of lubrication in severe stamping operations. In: 87747557, 2019.

MOG17b Moghadam, M.; Christiansen, P.; Bay, N.: Detection of the onset of galling in strip reduction testing using acoustic emission. In: Procedia Engineering 183, 2017, S. 59–64

MOG20 Moghadam, M.; Nielsen, C. V.; Bay, N.: Analysis of the risk of galling in sheet metal stamping dies with drawbeads. In: Proceedings of the Institution of Mechanical Engineers, Part B: Journal of Engineering Manufacture 234, Nr. 9, 2020, S. 1207–1214

MOG18 Moghadam, M. (Hrsg.); Nielsen, C. V. (Hrsg.); Christiansen, P. (Hrsg.); Bay, N. (Hrsg.): Tool condition monitoring in strip reduction testing using acoustic emission, 2018.

MOG19b Moghadam, M. (Hrsg.); Üstünyagiz, E. (Hrsg.); Nielsen, C. V. (Hrsg.): Evaluation of tribosystems for sheet metal forming, 2019.

MYU03 Myung, I.: Tutorial on maximum likelihood estimation. In: Journal of mathematical Psychology 47, Nr. 1, 2003, S. 90–100

NAK01 Nakano, T.: Compound Technology of Sheet Metal Forming and Forging. In: Journal of the Japan Society for Technology of Plasticity 42, Nr. 484, 2001, S. 388–392

NAK09 Nakano, T.: Introduction of Flow Control Forming (FCF) for sheet forging and new presses. In: Proceedings of the International Seminar on Precision Forging, Kyoto, 2009, S. 35–40

NET95 Netsch, T.: Methode zur Ermittlung von Reibmodellen für die Blechumformung: Shaker, 1995.

NOO16 Noorawzi, N.; Samion, S.: Tribological Effects of Vegetable Oil as Alternative Lubricant: A Pin-on-Disk Tribometer and Wear Study. In: Tribology Transactions 59, Nr. 5, 2016, S. 831–837

OHM27 Ohm, G. S.: Die galvanische kette: mathematisch: TH Riemann, 1827.

OKO11 Okonkwo, P. C. et al.: Effects of temperature in relation to sheet metal stamping. In: MEQAPS 2011: Proceedings of the 4th International Conference on Manufacturing Engineering, Quality and Production Systems : World Scientific and Engineering Academy and Society (WSEAS), 2011, S. 114–118

OKO12 Okonkwo, P. C. et al.: The effect of temperature on sliding wear of steel-tool steel pairs. In: Wear 282, 2012, S. 22–30

OLS09 Olsson, D. D.; Bay, N.; Andreasen, J. L.: A quantitative lubricant test for deep drawing. In: International Journal of Surface Science and Engineering 4, Nr. 1, 2009, S. 2–12

OST13 Ostasevicius, V. et al.: Study of vibration milling for improving surface finish of difficult-to-cut materials. In: Strojniški vestnik-Journal of Mechanical Engineering 59, Nr. 6, 2013, S. 351–357

PAI96 Painter, B.; Shivpuri, R.; Altan, T.: Prediction of die wear during hot-extrusion of engine valves. In: Journal of Materials Processing Technology 59, 1-2, 1996, S. 132–143

PAN61 Panknin, W.: Die Grundlagen des Tiefziehens im Anschlag unter besonderer Berücksichtigungder Tiefziehprüfung: Auszugsweise vorgetragen am 19. 3. 1959 vor dem Werkstoffausschuß des Vereins

Deutscher Eisenhüttenleute, Düsseldorf und am 24. 5. 1960 von der IDDRG in Paris: Bänder, Bleche, Rohre, 1961.

PEL05 Pelster, R.; Hüttl, I.; Pieper, R.: Thermospannungen-viel genutzt und fast immer falsch erklärt. In: PhyDid A-Physik und Didaktik in Schule und Hochschule 1, Nr. 4, 2005, S. 10–22

PER09 Pereira, M.: Tool wear analysis in sheet metal stamping. Deakin University. 2009

PER08 Pereira, M.; Yan, W.; Rolfe, B.: Contact pressure evolution and its relation to wear in sheet metal forming. In: Wear 265, 11-12, 2008, S. 1687–1699

PER10 Pereira, M.; Yan, W.; Rolfe, B.: Sliding distance, contact pressure and wear in sheet metal stamping. In: Wear 268, 11-12, 2010, S. 1275–1284

PET03 Pettersson, U.; Jacobson, S.: Influence of surface texture on boundary lubricated sliding contacts. In: Tribology international 36, Nr. 11, 2003, S. 857–864

POD04 Podgornik, B.; Hogmark, S.; Pezdirnik, J.: Comparison between different test methods for evaluation of galling properties of surface engineered tool surfaces. In: Wear 257, Nr. 7, 2004, S. 843–851. URL: https://www.sciencedirect.com/science/article/pii/S0043164804001152

POU86 Poursartip, A.; Beaumont, P. W.: The fatigue damage mechanics of a carbon fibre composite laminate: II—life prediction. In: Composites Science and Technology 25, Nr. 4, 1986, S. 283–299

PUJ13 Pujante, J. et al.: Investigations into wear and galling mechanism of aluminium alloy-tool steel tribopair at different temperatures. In: Wear 308, Nr. 1, 2013, S. 193–198. URL: https://www.sciencedirect.com/science/article/pii/S0043164813004080

RAA03 Raabe, D. et al.: Grain-scale micromechanics of polycrystal surfaces during plastic straining. In: Acta Materialia 51, Nr. 6, 2003, S. 1539–1560

RAB66 Rabinowicz, E.; Tanner, R. I.: Friction and wear of materials. In: Journal of Applied Mechanics 33, Nr. 2, 1966, S. 479

RAM10 Ramezani, M.; Ripin, Z. M.; Ahmad, R.: Sheet metal forming with the aid of flexible punch, numerical approach and experimental validation. In: CIRP Journal of Manufacturing Science and Technology 3, Nr. 3, 2010, S. 196–203

RAN96 Rangarajan, V.; Jagannathan, Vijay; Raghavan, K. S.: Influence of strain state on powdering of galvannealed sheet steel. In: SAE Transactions, 1996, S. 68–75

REC20 Recklin, V.: Untersuchung des Einflusses dehnungsinduzierter Oberflächenevolution in der Blechumformung: Shaker Verlag, 2020.

REI12 Reizer, R. et al.: Modeling of worn surface topography formed in a low wear process. In: Wear 278, 2012, S. 94–100

SAI89 Saito, M.; Saiki, H.; Kawai, N.: Experimental Analysis of Ironing of Thin Metal Cups. In: Journal of Engineering for Industry 111, Nr. 1, 1989, S. 56–63

SAS84 Sasada, T.; Oike, M.; Emori, N.: The effect of abrasive grain size on the transition between abrasive and adhesive wear. In: Wear 97, Nr. 3, 1984, S. 291–302. URL: https://www.sciencedirect.com/science/article/pii/0043164884901558

SCH93 Schedin, E.; Lehtinen, B.: Galling mechanisms in lubricated systems: A study of sheet metal forming. In: Wear 170, Nr. 1, 1993, S. 119–130. URL: https://www.sciencedirect.com/science/article/pii/004316489390358S

SCH21a Schell, L.; Groche, P.: In Search of the Perfect Sheet Metal Forming Tribometer. In: Forming the Future : Springer, Cham, 2021, S. 81–96

SCH21b Schrepfer, A. et al.: Reduktion von adhäsivem Verschleiß durch thermostromunterdrückende Werkzeugbeschichtung. Hannover: Europäische Forschungsgesellschaft für Blechverarbeitung e.V. (EFB), 2021.

SCR87 Scruby, C. B.: An introduction to acoustic emission. In: Journal of Physics E: Scientific Instruments 20, Nr. 8, 1987, S. 946–953

SEN81 Sendeckyj, G. P.: Fitting models to composite materials fatigue data: ASTM International, 1981.

SHA07 Shaffer, S. J.; Rogers, M. J.: Tribological performance of various coatings in unlubricated sliding for use in small arms action components—A case study. In: Wear 263, Nr. 7, 2007, S. 1281–1290. URL: https://www.sciencedirect.com/science/article/pii/S0043164807004437

SHA19 Shahzad, A.: Investigation into fatigue strength of natural/synthetic fiber-based composite materials. In: Mechanical and Physical Testing of Biocomposites, Fibre-Reinforced Composites and Hybrid Composites : Elsevier, 2019, S. 215–239

SIE32 Siebel, E.: Die Formgebung im bildsamen Zustande: theoretische Grundlagen der technischen Formgebungsverfahren: Verlag Stahleisen, 1932.

SIM94 Simão, J. et al.: Mill roll texturing using EDT. In: Journal of Materials Processing Technology 45, Nr. 1, 1994, S. 207–214. URL: https://www.sciencedirect.com/science/article/pii/0924013694903425

SIM89 Simon, H.: Rechnergestützte Ziehteilauslegung mit elementaren Berechnungsmethoden. Dissertation, Universität Hannover. 1989

SKÅ03 Skåre, T.; Krantz, F.: Wear and frictional behaviour of high strength steel in stamping monitored by acoustic emission technique. In: Wear 255, Nr. 7, 2003, S. 1471–1479. URL: https://www.sciencedirect.com/science/article/pii/S0043164803001972

SOB92 Sobis, T.; Engel, U.; Geiger, M.: A theoretical study on wear simulation in metal forming processes. In: Journal of Materials Processing Technology 34, 1-4, 1992, S. 233–240

STA06 Stachowiak, G.; BATCHELOR, A. W. (Mitarb.); BATCHELOR, A. W. (Mitarb.) : Engineering Tribology. 3rd ed. Oxford: Elsevier Science & Technology, 2006.

STE96 Steinhoff, K.; Rasp, W.; Pawelski, O.: Development of deterministic-stochastic surface structures to improve the tribological conditions of sheet forming processes. In: Journal of Materials Processing Technology 60, Nr. 1, 1996, S. 355–361. URL: https://www.sciencedirect.com/science/article/pii/0924013696023540

STE15 Steitz, M.; Stein, P.; Groche, P.: Influence of hammer-peened surface textures on friction behavior. In: Tribology Letters 58, Nr. 2, 2015, S. 1–8

STR14 Stromeyer, C. E.: The determination of fatigue limits under alternating stress conditions. In: Proceedings of the Royal Society of London. Series A, Containing Papers of a Mathematical and Physical Character 90, Nr. 620, 1914, S. 411–425

SWA88 Swanson, P. A. et al.: A study of the galling of two steels using two test methods. In: Wear 122, Nr. 2, 1988, S. 207–223. URL: https://www.sciencedirect.com/science/article/pii/0043164888900786

TAK13 Takadoum, J.: Materials and surface engineering in tribology: John Wiley & Sons, 2013.

THO80 Thomson, P. F.; Nayak, P. U.: The effect of plastic deformation on the roughening of free surfaces of sheet metal. In: International Journal of Machine Tool Design and Research 20, Nr. 1, 1980, S. 73–86

TIL17 Tillmann, W. et al.: Adjustment of friction by duplex-treated, bionic structures for Sheet-Bulk Metal Forming. In: Tribology international 111, 2017, S. 9–17. URL: https://www.sciencedirect.com/science/article/pii/S0301679X17300981

TIM70 Timoshenko, S.: Theory of elastic stability 2e: Tata McGraw-Hill Education, 1970.

TIS18 Tisza, M.; Czinege, I.: Comparative study of the application of steels and aluminium in lightweight production of automotive parts. In: International Journal of Lightweight Materials and Manufacture 1, Nr. 4, 2018, S. 229–238

TRÖ15 Tröber, P.: Influence of lubrication on the measured thermoelectric volt-age and temperature in the forming zone when embossing S355MC. In: Dry Metal Forming Open Access Journal, 2015.

TRÖ16 Tröber, P.: Experimental investigation on the thermoelectric current during embossing of Aluminum EN AW 1050. In: Dry Metal Forming Open Access Journal, 2016.

TRÖ17a Tröber, P. et al.: On the correlation between thermoelectricity and adhesive tool wear during blanking of aluminum sheets. In: International Journal of Machine Tools and Manufacture 118, 2017, S. 91–97

TRÖ17b Tröber, P. et al.: On the influence of Seebeck coefficients on adhesive tool wear during sheet metal processing. In: CIRP Annals 66, Nr. 1, 2017, S. 293–296

TRÖ18 Tröber, P. et al.: The influence of process parameters on the temperature development in the forming zone. In: MATEC web of conferences : EDP Sciences, 2018 (190), S. 14004

TRÖ19 Tröber, P. et al.: The influence of process parameters and sheet material on the temperature development in the forming zone. In: Manufacturing Review 6, 2019, S. 9

TRZ19 Trzepiecinski, T.; Lemu, H. G.: Recent developments and trends in the friction testing for conventional sheet metal forming and incremental sheet forming. In: Metals 10, Nr. 1, 2019, S. 47

TSC06 Tschaetsch, H.: Metal forming practise: processes—machines—tools: Springer, 2006.

TSU65 Tsukizoe, T.; Hisakado, T.: On the Mechanism of Contact Between Metal Surfaces—The Penetrating Depth and the Average Clearance. In: Journal of Basic Engineering 87, Nr. 3, 1965, S. 666–672

TSU18 Tsutsumi, D. et al.: Towards joint optimization of product design, process planning and production planning in multi-product assembly. In: CIRP Annals 67, Nr. 1, 2018, S. 441–446

UBH17 Ubhayaratne, I. et al.: Audio signal analysis for tool wear monitoring in sheet metal stamping. In: Mechanical Systems and Signal Processing 85, 2017, S. 809–826. URL: https://www.sciencedirect.com/science/article/pii/S0888327016303570

UEH92 Uehara, K.; Sakurai, M.; Ikeda, T.: On the Problem of Thermoelectric Current in Metal Cutting. In: CIRP Annals 41, Nr. 1, 1992, S. 75–78. URL: https://www.sciencedirect.com/science/article/pii/S0007850607611561

ÜST17 Üstünyagiz, E. et al.: Continuous strip reduction test simulating tribological conditions in ironing. In: Procedia Engineering 207, 2017, S. 2286–2291

ÜST18 Üstünyagiz, E. et al.: A study on DLC tool coating for deep drawing and ironing of stainless steel. In: Key Engineering Materials : Trans Tech Publ, 2018 (767), S. 181–188

ÜST19 Üstünyagiz, E. et al.: A combined numerical and experimental approach for determining the contact temperature in an industrial ironing operation. In: Journal of Materials Processing Technology 264, 2019, S. 249–258. URL: https://www.sciencedirect.com/science/article/pii/S0924013618304126

VAN02 van der Heide, E.: Lubricant failure in sheet metal forming processes. In: University of Twente, 2002.

VAN01 van der Heide, E.; Huis in ‘t Veld,, A. J.; Schipper, D. J.: The effect of lubricant selection on galling in a model wear test. In: Wear 251, Nr. 1, 2001, S. 973–979. URL: https://www.sciencedirect.com/science/article/pii/S004316480100761X

VEL17 Velkavrh, I. et al.: Using a standard pin-on-disc tribometer to analyse friction in a metal forming process. In: Tribology international 114, 2017, S. 418–428

VET13 Vettivel, S. C. et al.: Numerical modelling, prediction of Cu–W nano powder composite in dry sliding wear condition using response surface methodology. In: Materials & Design 50, 2013, S. 977–996

VOL05 Volk, R. (Hrsg.): Rauheitsmessung - Theorie und Praxis. 1. Aufl. Berlin, Wien, Zürich: Beuth, 2005.

VOR17 Vorholt, J. et al.: In-situ observation of lubricant flow on laser textured die surface in sheet metal forming. In: Procedia Engineering 207, 2017, S. 2209–2214

VOS17 Voss, B. M. et al.: A new methodology for measuring galling wear severity in high strength steels. In: Wear 390-391, 2017, S. 334–345. URL: https://www.sciencedirect.com/science/article/pii/S0043164817306439

WAN13 Wang, C. et al.: Die wear prediction by defining three-stage coefficient K for AHSS sheet metal forming process. In: The International Journal of Advanced Manufacturing Technology 69, Nr. 1, 2013, S. 797–803

WAN74 Wang, N.; Wenner, M. L.: An analytical and experimental study of stretch flanging. In: International Journal of Mechanical Sciences 16, Nr. 2, 1974, S. 135–143

WAN11 Wang, X.; Masood, S. H.: Investigation of die radius arc profile on wear behaviour in sheet metal processing of advanced high strength steels. In: Materials & Design 32, Nr. 3, 2011, S. 1118–1128

WEB94 Weber, H.; Seltz, R.: Zwischen „Over-engineering“ und „Lean Construction“-Zum Wandel von Organisation und Qualifikation von Ingenieuren. In: WEBER, H. (Hrsg.): Lean Management — Wege aus der Krise: Organisatorische und gesellschaftliche Strategien. Wiesbaden : Gabler Verlag, 1994, S. 157–187

WEI52 Weibull, W.: The statistical aspect of fatigue failure and its consequences. In: Fatigue and fracture of metals 4, 1952, S. 182–196

WEI14 Weisberg, Sanford: Applied linear regression. Fourth edition. Hoboken, NJ: Wiley, 2014.

WEL20 Welm, M. et al.: Thermoelectrically Based Approaches to Reduce Adhesive Wear During Blanking. In: JOM 72, Nr. 7, 2020, S. 2525–2535

WES03 Westeneng, A. J.: Modelling of contact and friction in deep drawing processes, 2003.

WIL05a Williams, J.: Engineering tribology: Cambridge University Press, 2005.

WIL05b Williams, J.: Wear and wear particles—some fundamentals. In: Tribology international 38, Nr. 10, 2005, S. 863–870

WÖH71 Wöhler, A.: Tests to determine the forces acting on railway carriage axles and the capacity of resistance of the axles. In: Engineering 11, Nr. 199, 1871, S. 1858–1870

WU21a Wu, Y. et al.: Influence of the sheet metal Seebeck coefficient on wear detection based on thermoelectric measurement, in 24th International Conference on Metal Forming, 2021.

WU20 Wu, Y.; Groche, P.: Influence of Tool Finishing on the Wear Development in Strip Drawing Tests with High Strength Steels. In: Tribology Online 15, Nr. 3, 2020, S. 170–180

WU22 Wu, Y.; Li, R.; Groche, P.: Method for the estimation of wear resistance curves in sheet metal forming with uncoated tools. In: Key Engineering Materials. Vol. 926, 2022.

WU21b Wu, Y.; Recklin, V.; Groche, P.: Strain Induced Surface Change in Sheet Metal Forming: Numerical Prediction, Influence on Friction and Tool Wear. In: Journal of Manufacturing and Materials Processing 5, Nr. 2, 2021, S. 29

XIA07 Xia, Z.; Ren, F.: Die Wear Severity Diagram and Simulation. 2007

YAO11 Yao, Z.: Die Wear Evaluation for Stamping TRIP700 and DP980 B-Pillar. In: SAE international, 2011.

YAS17 Yasuyoshi, T. et al.: THE MEASUREMENT OF SURFACE TEMPERATURES ON GEAR TEETH DURING HIGH SURFACE PRESSURE WITH DISSIMILAR HARDENED GEARS. In: The Japan Society of Mechanical Engineers, 2017, S. 7

YIL17 Yilkiran, D. et al.: Wear behaviour of thermally oxidised tool surfaces as low-friction separation layers for dry sheet metal forming. In: Wear 376-377, 2017, S. 1789–1803. URL: https://www.sciencedirect.com/science/article/pii/S0043164817302156

YOO13 Yoon, J. W.; Barlat, F.: Modeling and simulation of the forming of aluminum sheet alloys, 2013.